Organic/Inorganic Nanocomposite Materials by Electrospinning and Their Properties

A Dissertation Presented

by

Guan Wang

to

The Graduate School

in Partial Fulfillment of the Requirements for the Degree of

Doctor of Philosophy

in

Materials Science and Engineering

Stony Brook University

December 2007

Stony Brook University

The Graduate School

GUAN WANG

We, the dissertation committee for the above candidate for the Doctor of Philosophy degree, hereby recommend acceptance of this dissertation.

Professor Michael Dudley, Advisor
Department of Materials Science and Engineering

Professor Dilip Gersappe
Department of Materials Science and Engineering

Professor Yimei Zhu
Department of Materials Science and Engineering

Dr. Xiaoqing Yang
Department of Chemistry, Brookhaven National Laboratory, NY

This dissertation is accepted by the Graduate School

Lawrence Martin
Dean of the Graduate School

Abstract of the Dissertation

Organic/Inorganic Nanocomposite Materials by Electrospinning and Their Properties

A Dissertation Presented
by
Guan Wang
Doctor of Philosophy
in
Materials Science and Engineering
Stony Brook University
2007

One-dimensional (1D) nanostructures, such as nanowires, nanobelts, nanofibers and nanotubes, have been the focus of intensive research due to their peculiar structures and resultant fascinating properties. However, the applications of 1D nanostructures have been hindered by the slow progress of the synthesis and characterization methods for these nanoscaled materials. Well controlled dimensionality, tailorable morphology and assembly, high phase purity and controllable crystallinity are major concerns when generating these nanostructures.

In this work, a relatively simple technique -- electrospinning has been introduced for the preparation of 1D organic/inorganic nanocomposite materials. Materials under investigation include polymer/metal oxide (WO_3, MoO_3) composite nanofibers and polymer/MWNT composite nanofibers. Notably, peculiar nanostructures, such as polycrystalline nanowires, nanoplatelets and nanobelts, can also be obtained after post-calcination processing on the nanocomposite materials. Spectroscopy techniques, such as XRD, SEM, TEM, AFM and Raman have been carried out to obtain structural and morphological information from the electrospun composite nanofibers. Meanwhile, some advanced characterization methods and measurements have been developed and designed to investigate the nanofibers from a basic science view point as to their properties. Specific designs of experiment include: synchrotron-based *in situ* XRD for phase transition monitoring; gas flow control bench for sensitivity measurement; three-point-bending by AFM for mechanical property measurement.

In summary, the electrospinning technique provides a versatile method for synthesizing and assembling 1D nanocomposite structures. The electrospun composite nanofibers showed promising electrical and mechanical properties, which may find applications for gas sensors, reinforced fibrous materials and nano-electrical devices.

Dedicated to

My Beloved Father and Mother

Table of Contents

Chapter 4 **Electrospinning Polymer/MWNT Composite Nanofibers**

Chapter 5 **Polymer/MWNT Composite Nanofibers for Gas Sensing Applications**

Chapter 6 **Highlights of This Research and Future Work**

List of Figures

List of Tables

Acknowledgement

I would like to extend my sincere gratitude to my advisor, Prof. Michael Dudley, for his trust, encouragement, support and valuable instructions throughout the course of this research.

Sincere thanks are due to Prof. Dilip Gersappe, Dr. Yimei Zhu and Dr. Xiaoqing Yang for serving on my defense committee and for their valuable comments and suggestions on the my dissertation.

I would like to thank Dr. Jim Quinn for his generous help in times of need and emergencies related to laboratory equipments. Without his help and suggestions, this work cannot be finished.

Thanks are owed to all my friends and colleagues for their valuable discussions. I greatly appreciate the help from Dr. Yuan Ji for his help during the initial stages of the research and his willingness to share his fine knowledge and experiences. I am deeply grateful to Dr. Vladimir Samuilov for his help with various aspects of sensor technologies including assistance with the gas sensing setup and measurements. I feel grateful for the help from Dr. John Hanson with the XRD equipment at NSLS at the Brookhaven National Laboratory (BNL), and the help from Dr. Lihua Zhang with high resolution TEM at the Center of Functional Nanomaterials (CFN).

I also would like to thank all my friends in the department for their support: Dr. Xianrong Huang, Dr. Balaji Raghothamachar, Dr. Jie Bai, Hui Chen, Yi Chen, Ning Zhang, Lisheng Wang, Shanshan Liang, Samrat Chawda, Jose Mawyin, Minhua Shao, Ja-Seung Koo. Special thanks to Debby and Lynn for providing me all the academic and research-related help throughout my study.

This project has been supported by a National Science Foundation (NSF) NIRT Grant, under the direction of Pelagia Gouma, Fu-Pen Chiang, Michael Dudley, and Sanford R. Simon at SUNY Stony Brook (award ID: DMR-0304169, 2003-2007). All the X-ray diffraction experiments have been carried out at the National Synchrotron Light Source (NSLS), Brookhaven National Laboratory, which is supported by the U.S. Department of Energy (D.O.E.).

CHAPTER 1

Introduction

1.1 Background

The study of materials with low dimensionality has a long history in chemistry and physics because of the fascinating properties and applications resulting from lowered dimensionalities. More recently, one-dimensional (1D) nanostructures such as nanowires, nanobelts and nanofibers have become the focus of intensive research[1-3]. 1D nanostructures provide a unique system to study the transport phenomena or mechanical properties due to the different ways that electrons interact in one-dimensional (1D) structures. They are also expected to work as interconnects and functional units in fabricating nanoscaled electronic, optoelectronic and electromechanical devices. However, the applications of 1D nanostructure have been hindered by the lack of understanding of the synthesis and fabrication of these nanostructures with well-controlled dimensionality, morphology, purity and crystallinity. Under this circumstance, unconventional methods based on chemistry synthesis and nanoscaled growth techniques are being developed to provide intriguing strategies for generating 1D nanostructures in terms of materials diversity, cost and potential for high-volume production [4].

In this chapter, the concepts related to the growth of nanowires, as well as synthetic strategies for achieving 1D morphologies, will be reviewed. Electrospinning, as a kind of simple and versatile method for generating ultra-thin fibers from a rich variety of materials, will be introduced in the following sections. Concepts on the solid state chemical sensor materials and devices, their sensing mechanism and applications will be introduced. At the end of this chapter, the objectives and organization of the study are stated.

1.2 Available Strategies for 1D Synthesis

1.2.1 Template directed growth

Template-directed synthesis is a straightforward route to 1D nanostructures. In this approach, the template serves as a scaffold within or around which a different material is generated *in situ* and shaped into a nanostructure with its morphology complementary to that of the template[5]. The template is usually involved only physically, working as a confinement for the formation of the secondary nanostructures. Therefore, at the end of the synthesis it is often necessary to remove the template selectively using chemical etching or calcination. It is generally accepted that template-directed synthesis provides a simple and effective procedure that allows the complex topology on the template surface to be duplicated in a single step. However, a most obvious drawback of this method is that crystallinity of the nanostructures synthesized using template-directed methods is often uncontrollable, and the quantity that can be produced in one experiment is relatively limited.

A representative template-directed synthesis is to use channels in porous membranes, which provide a class of template for use in the synthesis of 1D nanostructures. This method was initiated by Martin and some other groups [6-8]. Two types of porous materials are commonly used in such syntheses: polymer films containing track-etched channels and alumina films containing anodically etched pores. A variety of materials have been examined for use with this type of templates, with typical examples like semiconductors [9, 10], ceramics [11, 12], and organic polymers [13, 14]. The only requirement is that the material can be loaded into the pores using methods based on vapor-phase sputtering, liquid-phase injection, or solution-phase chemical or electrochemical deposition. Subsequent sintering at elevated temperatures led to the formation of uniform, ceramic nanorods with compositions such as titania and $Pb(Zr,Ti)O_3$ (PZT). If a polymer template is used, the template can be readily removed at elevated temperature during the formation of the nanostructure. But when inorganic templates are employed, strong acid or alkali becomes necessary to remove the template and harvest the resultant nanostructures.

Another common method for template-directed growth is the synthesis upon existing nanostructures. The surfaces of the existing nanowires could be directly coated with conformal sheaths made of a different material to form coaxial nanocables. Subsequent dissolution of the original nanowires would lead to the formation of nanotubes. For instance, Murphy and co-workers have directly coated gold nanorods with polystyrene or silica (5-10nm in thickness) to form cable-like nanostructures [15]. In addition, the sol-gel coating method has been examined as an effective route to coaxial nanocables that may contain electrically conductive cores and insulating sheaths in the form of amorphous silica or other dielectric materials [16]. Another representative work was carried out by Lee's group[17]. Oriented Silicon Carbide nanowires were synthesized by the reaction between SiO and highly aligned carbon nanotubes, which acted as a template, spatially confining the orientations of the formed SiC nanowires.

A number of solution-phase reactions have also been demonstrated to transform currently existing nanowires into 1D nanostructures with other chemical compositions.

Xia and co-workers have synthesized highly crystalline nanotubes of noble metals such as Au, Pd and Pt via galvanic displacement reactions between Ag nanowires and appropriate precursors of these metals in the aqueous medium [18, 19].

1.2.2 Vapor-based method

Growth of nanowires from the vapor phase is a generic method suitable for all solid materials. This synthesis has been the most extensively explored approach to the formation of various kinds of one-dimensional oxide nanostructures, such as nanowires of ZnO [20, 21], In_2O_3 [22], SiO_2 [23, 24], Ga_2O_3 [25, 26], and GeO_2 [27]; nanobelts of ZnO, SnO_2, Ga_2O_3, In_2O_3, CdO, and PbO_2 [28, 29]; and nanorods of MgO [30]. According to the different mechanisms during the formation of the one-dimensional structure, the vapor-based methods can also be categorized as thermal evaporation synthesis and Vapor-Liquid-Solid mechanism (VLS).

The thermal evaporation synthesis is based on the vaporization of source materials at a high-temperature zone, and their subsequent deposition in the downstream direction, which results in the formation of nanostructures at specific temperature zones. In this process, the driving forces for 1D growth were proposed to be (a) an anisotropic structure of the material[31], (b) the existence of an axial screw dislocation[32, 33], or (c) preferred growth introduced by other defects or catalysts. In an anisotropic growth mechanism, one-dimensional growth can be realized by preferential reactivity, binding of gas phase reactants along specific crystal facets due to the thermodynamic and kinetic conditions, and also the desire for a system to minimize surface energies. In the dislocation and defect-induced growth mechanism, specific defects are known to have larger sticking coefficients for gas phase species, thus incoming atoms could absorb onto the surface of the nanostructure and migrate toward the growing tip due to the enhanced reactivity of gas phase reactants at these defects. The concentrations of gaseous reactants have to be adjusted carefully, so that the nanowire growth mechanism is dominant and can suppress the nucleation process in the vapor. It is now accepted that a low super-saturation of gaseous reactants is required for 1D nanostructure growth; a medium super-saturation results in bulk crystal growth; and a high super-saturation supports the formation of powders due to homogenous nucleation. Representative synthesis of molybdenum oxide and tin oxide nanostructures by thermal evaporation has been carried out by Wang's group [34, 35].

Vapor-Liquid-Solid mechanism is the most successful method for generating large quantities of single crystalline 1D nanostructures[36-40]. In the VLS process, the one-dimensional growth is induced by liquid droplets of a catalyst metal, which form due to the dissolution of gaseous reactants. These liquid droplets are the starting sites for the nucleation and growth of the 1D nanostructures. They serve as a virtual template, directing the nanowire growth direction and limiting the lateral growth of an individual wire under chemical-vapor-deposition conditions [3]. This mechanism has been confirmed by Yang's group[38] by observing the *in situ* growth of Ge nanorods directly under a TEM equipped with a temperature-controlled chamber. The most challenging requirement for the VLS process is to find an appropriate catalyst, because of the important role of the liquid droplets in the initial stage of the process. The catalyst should be able to form liquid alloy with the target material. Presently, this is done by analyzing the equilibrium phase diagrams. It has been shown to be very effective to consider the pseudo-binary phase diagram between the metal catalyst and the solid material of interest [39]. Based on the VLS mechanism, some other methods have been developed, such as laser ablation synthesis[41], oxide-assisted growth[42] and chemical vapor deposition [43].

1.2.3 Nanowire growth by solution-phase methods

The major disadvantages of the growth by vapor-based methods are the high cost of fabrication and inability to produce metallic nanowires. Synthesis from solution can be a complementary method to solve these problems.

Solvothermal synthesis is one of the most commonly used solution phase methods. In a typical process, the reaction occurs in a pressure vessel that allows normal solvents such as water to be heated to temperatures far beyond their normal boiling points to increase the solubility of a solid and speed up the reactions between solids. This method has been used by Heath's group for generating Ge nanowires[44]. Qian, Xie and Li's groups extended this method for synthesizing nanowires[45], nanotubes[46] and nanowhiskers[47-49] of a variety of other materials. However, the low yield, low purity and un-controllable size and morphology of the resultant materials greatly limit the applications of this method.

Another effective solution-phase method is based on capping reagents, which has resulted in the creation of one-dimensional nano-materials in high yields. By preferentially adsorbing to specific crystal faces, the molecular capping agents can change the free energies of the various crystallographic surfaces, thus control the final shape of the crystals by controlling the growth kinetics of the nanocrystals[50, 51]. Representative work includes the formation of silver nanowires using poly(vinyl pyrrolidone) (PVP) as a capping agent[52-54] and the shape-control growth of CdSe quantum nanorods through the use of mixed surfactants[55].

1.2.4 Other useful approaches

A number of radically different approaches have also been demonstrated as alternative routes to the fabrication of 1D nanostructures. For specific materials, highly isotropic crystallographic structures can be utilized. Typical examples are using molybdenum chalcogenides[56, 57] and chalcogens[58-60], which tend to form polymeric chain structures with diameters of a few nanometers.

Another generic bottom-up approach for generating complex structures is realized by surface patterning. Representative methods include the self-assembly of nanoparticles[61-65] and manipulation of 0D nanostructures with a field or a mechanical probe[66]. However, these methods all seem lack of control over the dimensions and morphology of the final products. Moreover, the slow production rates also limit their applications.

1.3 Electrospinning Technique

Nanomaterials produced by synthetic bottom-up methods are usually discontinuous objects, and this leads to difficulties with their alignment, assembly, and processing into applications. The formation of a thin fiber via electrospinning is based on the uni-axial stretching of a jet derived from a viscoelastic solution. Different from conventional fiber spinning methods like dry-spinning and melt-spinning, electrospinning makes use of electrostatic forces to stretch the solution as it solidifies. [67]. The first patent on the electrospinning process was awarded in 1934; and since the mid-1990s, the process attracted rapidly growing interest triggered by the potential applications of nanofibers in nanotechnology [68].

A schematic drawing of the electrospinning process is shown in Figure 1.1. It consists four main parts: i). a high voltage power supply, capable of producing up to 30kV high voltage; ii) a programmable pump meter, used to precisely control the feeding rate of the solution from the syringe tip; iii) a syringe with capillary tip; and iv) a piece of conducting metal for collecting the fibers.

In electrospinning, when a high voltage (usually in the range of 1 to 30 kV) is applied, the pendant drop of polymer will become highly electrified and the induced charges are evenly distributed over the surface. As a result, the drop will experience two electrostatic forces: the repulsion between the surface charges; and the Coulombic force exerted by the external electric field. Under the action of these two forces, the liquid drop will be distorted into a conical object, which is known as Taylor cone. A liquid jet forms once the electrical forces at the surface of a polymer solution or melt overcome the surface tension. This field jet then undergoes a stretching and whipping process, leading to the formation of an ultra-thin thread. As the liquid jet is continuously elongated and the solvent is evaporated, its diameter can be greatly reduced from hundreds of micrometers to as small as tens of nanometers.

Based on experimental observations and electrohydrodynamic theories, mathematical models have been developed by several groups to investigate the electrospinning process [69-73]. It is also showed that the models could be extended to predict the saturation of whipping amplitude, as well as the diameter of resultant fibers. All these studies provide a better understanding of the mechanism responsible for electrostatic spinning process.

The morphology and diameter control of the electrospun fibers has been a major problem since the invention of the electrospinning technique. In fact, it is a co-effect of a number of processing parameters, including a) the intrinsic properties of the solution such as the type of the polymer, the conformation of the polymer chain, viscosity, elasticity, electrical conductivity and the polarity and surface tension of the solvent; and b) the operational conditions, such as the strength of the applied electric field, the distance between spinneret and collector, and the feeding rate for the polymer solution. In addition to these variables, the humidity and temperature of the environment can also play an important role during the electrospinning process.

Among all the factors, the solution concentration plays a major role in stabilizing the fibrous structure. It has been shown previously in dilute solutions, $[\eta]C<1$, where $[\eta]$ is the intrinsic viscosity and C is the concentration [74]. When $[\eta]C>4$ (semi-dilute entangled regime), the polymer chains in the solution begin to entangle with each other and the solution viscosity increases significantly. For example, Koski and co-workers [75] have shown that for PVA in water solution, a fibrous structure cannot be stablized for $[\eta]C<4$, indicating that a minimum degree of chain entanglement is need for producing fibrous structures. Another important factor is surface tension of the solution. A low surface tension is desirable in electrospinning as it reduces the critical voltage V_c needed for the ejection of the jet from the Taylor's cone as shown below [76]:

$$V_c^2 = 4\frac{H^2}{L^2}\left(\ln\frac{2L}{R} - \frac{3}{2}\right)\left(0.117\pi\gamma R\right)$$

Where V_c = critical voltage

H = separation distance between the needle and the collector

L = the length of the needle (or capillary)

R = the radius of the needle and

γ = the surface tension of the solution.

A similar relationship correlating the applied electric field and surface tension of the droplet for the electrostatic spraying from a hemispherical drop pendant from a capillary tube was also contributed by Hendrick et al. [77]

$$V_c = 300\sqrt{20\pi\gamma r}$$

where r = the radius of the pendant drop.

On the other hand, spraying may become more difficult at high molecular weights since V_c is proportional to M_w. At any specified value of $[\eta]C$ in the fibrous regime, it may be desirable to lower M_w and increase C.

Early experimental work on electrospinning mainly dealt with conventional polymers that could be synthesized with sufficiently high molecular weights and could be dissolved in appropriate solvents. In an effort to greatly expand the applications associated with fibrous structures, a variety of methods have recently been developed to increase the diversity of materials that can be adapted for use with electrospinning. An representative example is that, in combination with sol-gel chemistry, the original process used with high molecular weight polymers has been modified and applied to produce continuous ceramic nanofibers [78-80]. Some metal oxide nanofibers have been fabricated, such as alumina borate [79], titania silica [81], cobalt oxide [82], copper oxide [83], niobium oxide [84], vanadium pentoxide [85] and zinc oxide [86]. These nanofibers can be beneficial in the areas of catalysis, tough and high-temperature ceramics, active and sensing materials, and many others.

In order to fully realize the potential of electrospun fibers, it is also important to customize nanofiber assemblies, as the fiber arrangement will have a significant affect on the performance of a device. For example, ordered nano-grooves and assemblies have been shown to influence cell proliferation and morphology; it is necessary that the single nanofiber can be grown or positioned across specific electrodes; a nonwoven mesh is desirable when applied as a filtration membrane. Driven by the specific applications, new designs of electrospinning have been created to construct nanofiber assemblies, such that their performance can be enhanced. Ramakrishna and Teo have summarized all kinds of designs for achieving various nanofiber assemblies in their review paper [87].

1.4 Solid-State Chemical Sensors

A sensor is a device that responds to a physical or chemical stimulus and transmits a resulting impulse. Sensors have been used in a variety of industries for factory automation, electronic equipment, agriculture, aerospace industries and homeland security. Their specific applications include[88]:

(i) Pollution monitoring and control – To check for pollution problems in the atmosphere including acid rain, metal contaminants, etc.

(ii) Hazard monitoring – In order to monitor explosive gas hazards, suitable sensors are required. Moreover, sensors are needed to monitor the effects of toxic chemicals and their effect on human health in industry.

(iii) Combustion control – Gas sensors are used in monitor and control of gas and oil fired boilers in industrial premises. The fuel to air mixture ratio is controlled by monitoring the exhaust gas of automobiles. This is required to conserve fuel and to minimize pollution emission from motor vehicles.

(iv) Medicine – Monitoring the chemical species in the blood and other bodily fluids and real time monitoring of patients' condition requires the use of sensors.

According to the type of signals detected, sensors can be categorized as different types, among which chemical sensors represent the mostly studied sensors with the widest applications. According to Göpel and Schierbaum [89], 'Chemical sensors are devices which convert a chemical state into an electrical signal'. Therefore, every chemical sensor is divided into two domains: the physical transducer and the chemical interface layer (Figure 1.2). At the chemical interface, the analyte interacts chemically with a surface, producing a change in physical/chemical properties such as resistance, capacitance, or temperature of the active element. These changes are measured by the transducer domain, which monitors this change and generates a related electrical signal.

The major advantages of solid state sensors are their simplicity in function, small size and projected low cost. The simplicity in function is in sharp contrast to some of the more classical analysis techniques, which require complex equipment and skilled operators to run an analysis. The projected cost is low because the size of the sample used is small (typically measured in centimeters to micrometers).

The major disadvantages of most solid-state chemical sensors are lack of stability, lack of reproducibility, and lack of selectivity as well as insufficient sensitivity for certain purposes. However, in many applications, the disadvantages are not prohibitive, and the use of arrays of sensors feeding a microcircuit can in principle overcome many of the disadvantages while still retaining a reasonable cost. [90]

One way to classify chemical sensors is by the transduction mechanism (as shown in reference[91]). Different transduction principles and the magnitudes that can be measured include:

- Electrochemical: voltages, currents, impedance
- Mechanical: weight, size, shape
- Thermal: heat flow, heat content
- Magnetic: field strength, field detection
- Radiant: frequency, intensity, wavelength
- Acoustic: bulk and surface acoustic wave devices

In addition to above categorization method, chemical sensors can also be arranged by the chemical reactions that occur at the interface. This approach is very interesting since chemical parameters, such as the type of chemical reaction, equilibrium constant, kinetic parameters, will determine the sensor performance, including sensor sensitivity and selectivity.

On another hand, in terms of the types of the materials used, solid state sensors can be classified as silicon-based chemical sensors, semiconducting metal oxide sensors, catalysis sensors, solid electrolyte sensors, membrane sensors and carbon nanotube sensors. The major two sensors discussed in this thesis are semiconducting metal oxide (tungsten oxide and molybdenum oxide) sensors and carbon nanotube (multiwalled carbon nanotubes) sensors.

The work in this thesis will be limited to the processing and characterization of one-dimensional materials (such as nanowires, nanofibers and nanotubes) for gas sensing applications. They are expected to possess novel characteristics for the following reasons[92]:

(a) A large surface-to-volume ratio can be provided, so that a significant fraction of the atoms in the system are surface atoms that can participate in surface reactions.

(b) The Debye length λ_D for most semiconducting oxide nanowires is close to their radius over a wide temperature and doping range, which causes their electronic properties to be strongly influenced by processes at their surface. This could result in better sensitivity and selectivity.

(c) Nanowires are easily configurable as field-effect transistors (FETs) and potentially integratable with conventional devices and device fabrication techniques.

(d) Significant quantum effect is expected due to the reduction of nanowire diameter.

1.5 Objectives and Organization

The work in this thesis can be divided into three major parts:

Part I (Chapter 2): Polycrystalline tungsten oxide nanowires for ammonia sensing applications. This part focuses on the fabrication of tungsten oxide polycrystalline nanofibers by combining the electrospinning technique with sol-gel chemistry. Dynamic structural evolution of tungsten oxide will be studied at elevated temperatures for optimizing the heat treatment temperatures and achieving specific polymorphs of tungsten oxide. The sensitivity of the materials will be measured, with ammonia as the analyte.

Part II (Chapter 3): Molybdenum oxide nanostructures synthesized from hybrid nanocomposites. In this chapter, a simple method will be proposed for the shape-controlled growth of crystalline molybdenum oxide. The function of polymer as the surfactant and intercalation material during the crystallization of the layered structure of MoO_3 will be discussed, interpreting the preferential growth of the nanoplatelets from the nanocomposites. Combined with electrospinning process, morphology controlled growth of the α-MoO_3 nanobelts can be also realized. This method may be applied to the anisotropic growth of low dimensional nanostructures of other materials with layered structure.

Part III: (Chapter 4, 5) Electrospinning Polymer/MWNT nanocomposite fibers and their properties. In this chapter, electrospun polymer nanofibers will be utilized as carrier media to assemble carbon nanotubes (CNTs) into continuous filaments, allowing well-controlled alignment and tailored distribution of the CNTs within an external structure. Successful incorporation of CNTs into appropriate polymer matrix systems in filament or fine fiber forms can work as an effective bridge to translate the superior properties of carbon nanotubes to meso- and macro-scale structures. An AFM-based three-point-bending method is employed to study the mechanical properties of individual composite nanofibers. Electrical properties of a single composite fiber have been investigated at room temperature as well as cryogenic states. By integrating these composite nanofibers with interdigitated electrode structure, both quantitative and qualitative measurements of sensitivity of the materials have been carried out.

In summary, the main objectives of these investigations are:

- To explore the capability of electrospinning technique in the processing of 1D nanocomposite materials;

- To study the relationship between the processing-structure-properties of the nanostructured polymer/metal oxide ceramics composite materials and polymer/MWNT nanocomposites;
- To develop new techniques for advanced characterization of polymer/nanostructured ceramic metal oxides and polymer/MWNT nanocomposites;
- To explore possible applications of the distinctive properties of the 1D nanocomposite materials prepared by electrospinning.

References

1. Wang, Z. L., Characterizing the structure and properties of individual wire-like nanoentities. *Advanced Materials* **2000,** 12, (17), 1295-1298.

2. Hu, J. T.; Odom, T. W.; Lieber, C. M., Chemistry and physics in one dimension: Synthesis and properties of nanowires and nanotubes. *Accounts of Chemical Research* **1999,** 32, (5), 435-445.

3. Wang, Z. L., Nanobelts, nanowires, and nanodiskettes of semiconducting oxides - From materials to nanodevices. *Advanced Materials* **2003,** 15, (5), 432-436.

4. Xia, Y. N.; Rogers, J. A.; Paul, K. E.; Whitesides, G. M., Unconventional methods for fabricating and patterning nanostructures. *Chemical Reviews* **1999,** 99, (7), 1823-1848.

5. Xia, Y. N.; Yang, P. D.; Sun, Y. G.; Wu, Y. Y.; Mayers, B.; Gates, B.; Yin, Y. D.; Kim, F.; Yan, Y. Q., One-dimensional nanostructures: Synthesis, characterization, and applications. *Advanced Materials* **2003,** 15, (5), 353-389.

6. Hulteen, J. C.; Martin, C. R., A general template-based method for the preparation of nanomaterials. *Journal of Materials Chemistry* **1997,** 7, (7), 1075-1087.

7. Martin, C. R., Template Synthesis of Electronically Conductive Polymer Nanostructures. *Accounts of Chemical Research* **1995,** 28, (2), 61-68.

8. Martin, C. R., Nanomaterials - a Membrane-Based Synthetic Approach. *Science* **1994,** 266, (5193), 1961-1966.

9. Cao, H. Q.; Xu, Y.; Hong, J. M.; Liu, H. B.; Yin, G.; Li, B. L.; Tie, C. Y.; Xu, Z., Sol-gel template synthesis of an array of single crystal CdS nanowires on a porous alumina template. *Advanced Materials* **2001,** 13, (18), 1393-1394.

10. Zhang, X. Y.; Zhang, L. D.; Meng, G. W.; Li, G. H.; Jin-Phillipp, N. Y.; Phillipp, F., Synthesis of ordered single crystal silicon nanowire arrays. *Advanced Materials* **2001,** 13, (16), 1238-1241.

11. Zheng, M. J.; Zhang, L. D.; Zhang, X. Y.; Zhang, J.; Li, G. H., Fabrication and optical absorption of ordered indium oxide nanowire arrays embedded in anodic alumina membranes. *Chemical Physics Letters* **2001,** 334, (4-6), 298-302.

12. Lei, Y.; Zhang, L. D.; Meng, G. W.; Li, G. H.; Zhang, X. Y.; Liang, C. H.; Chen, W.;

Wang, S. X., Preparation and photoluminescence of highly ordered TiO2 nanowire arrays. *Applied Physics Letters* **2001,** 78, (8), 1125-1127.

13. Sapp, S. A.; Mitchell, D. T.; Martin, C. R., Using template-synthesized micro- and nanowires as building blocks for self-assembly of supramolecular architectures. *Chemistry of Materials* **1999,** 11, (5), 1183-1185.

14. Burford, R. P.; Tongtam, T., Conducting Polymers with Controlled Fibrillar Morphology. *Journal of Materials Science* **1991,** 26, (12), 3264-3270.

15. Obare, S. O.; Jana, N. R.; Murphy, C. J., Preparation of polystyrene- and silica-coated gold nanorods and their use as templates for the synthesis of hollow nanotubes. *Nano Letters* **2001,** 1, (11), 601-603.

16. Yin, Y. D.; Lu, Y.; Sun, Y. G.; Xia, Y. N., Silver nanowires can be directly coated with amorphous silica to generate well-controlled coaxial nanocables of silver/silica. *Nano Letters* **2002,** 2, (4), 427-430.

17. Pan, Z. W.; Lai, H. L.; Au, F. C. K.; Duan, X. F.; Zhou, W. Y.; Shi, W. S.; Wang, N.; Lee, C. S.; Wong, N. B.; Lee, S. T.; Xie, S. S., Oriented silicon carbide nanowires: Synthesis and field emission properties. *Advanced Materials* **2000,** 12, (16), 1186-1190.

18. Sun, Y. G.; Mayers, B. T.; Xia, Y. N., Template-engaged replacement reaction: A one-step approach to the large-scale synthesis of metal nanostructures with hollow interiors. *Nano Letters* **2002,** 2, (5), 481-485.

19. Wen, X. G.; Yang, S. H., Cu2S/Au core/sheath nanowires prepared by a simple redox deposition method. *Nano Letters* **2002,** 2, (5), 451-454.

20. Huang, M. H.; Mao, S.; Feick, H.; Yan, H. Q.; Wu, Y. Y.; Kind, H.; Weber, E.; Russo, R.; Yang, P. D., Room-temperature ultraviolet nanowire nanolasers. *Science* **2001,** 292, (5523), 1897-1899.

21. Huang, M. H.; Wu, Y. Y.; Feick, H.; Tran, N.; Weber, E.; Yang, P. D., Catalytic growth of zinc oxide nanowires by vapor transport. *Advanced Materials* **2001,** 13, (2), 113-116.

22. Liang, C. H.; Meng, G. W.; Lei, Y.; Phillipp, F.; Zhang, L. D., Catalytic growth of semiconducting In2O3 nanofibers. *Advanced Materials* **2001,** 13, (17), 1330-1333.

23. Zhu, Y. Q.; Hsu, W. K.; Terrones, M.; Grobert, N.; Terrones, H.; Hare, J. P.; Kroto, H. W.; Walton, D. R. M., 3D silicon oxide nanostructures: from nanoflowers to radiolaria.

Journal of Materials Chemistry **1998,** 8, (8), 1859-1864.

24. Wu, X. C.; Song, W. H.; Wang, K. Y.; Hu, T.; Zhao, B.; Sun, Y. P.; Du, J. J., Preparation and photoluminescence properties of amorphous silica nanowires. *Chemical Physics Letters* **2001,** 336, (1-2), 53-56.

25. Wu, X. C.; Song, W. H.; Huang, W. D.; Pu, M. H.; Zhao, B.; Sun, Y. P.; Du, J. J., Crystalline gallium oxide nanowires: intensive blue light emitters. *Chemical Physics Letters* **2000,** 328, (1-2), 5-9.

26. Zhang, H. Z.; Kong, Y. C.; Wang, Y. Z.; Du, X.; Bai, Z. G.; Wang, J. J.; Yu, D. P.; Ding, Y.; Hang, Q. L.; Feng, S. Q., Ga2O3 nanowires prepared by physical evaporation. *Solid State Communications* **1999,** 109, (11), 677-682.

27. Bai, Z. G.; Yu, D. P.; Zhang, H. Z.; Ding, Y.; Wang, Y. P.; Gal, X. Z.; Hang, Q. L.; Xiong, G. C.; Feng, S. Q., Nano-scale GeO2 wires synthesized by physical evaporation. *Chemical Physics Letters* **1999,** 303, (3-4), 311-314.

28. Pan, Z. W.; Dai, Z. R.; Wang, Z. L., Nanobelts of semiconducting oxides. *Science* **2001,** 291, (5510), 1947-1949.

29. Dai, Z. R.; Pan, Z. W.; Wang, Z. L., Ultra-long single crystalline nanoribbons of tin oxide. *Solid State Communications* **2001,** 118, (7), 351-354.

30. Yang, P. D.; Lieber, C. M., Nanorod-superconductor composites: A pathway to materials with high critical current densities. *Science* **1996,** 273, (5283), 1836-1840.

31. Yan, H. Q.; He, R. R.; Pham, J.; Yang, P. D., Morphogenesis of one-dimensional ZnO nano- and microcrystals. *Advanced Materials* **2003,** 15, (5), 402-405.

32. Sears, G. W., A Growth Mechanism for Mercury Whiskers. *Acta Metallurgica* **1955,** 3, (4), 361-366.

33. Sears, G. W., A Mechanism of Whisker Growth. *Acta Metallurgica* **1955,** 3, (4), 367-369.

34. Zhou, J.; Xu, N. S.; Deng, S. Z.; Chen, J.; She, J. C.; Wang, Z. L., Large-area nanowire arrays of molybdenum and molybdenum oxides: synthesis and field emission properties. *Advanced Materials* **2003,** 15, (21), 1835-1840.

35. Dai, Z. R.; Gole, J. L.; Stout, J. D.; Wang, Z. L., Tin oxide nanowires, nanoribbons, and nanotubes. *Journal of Physical Chemistry B* **2002,** 106, (6), 1274-1279.

36. Wu, Y. Y.; Yang, P. D., Germanium nanowire growth via simple vapor transport.

Chemistry of Materials **2000,** 12, (3), 605-607.

37. Gudiksen, M. S.; Lieber, C. M., Diameter-selective synthesis of semiconductor nanowires. *Journal of the American Chemical Society* **2000,** 122, (36), 8801-8802.

38. Wu, Y. Y.; Yang, P. D., Direct observation of vapor-liquid-solid nanowire growth. *Journal of the American Chemical Society* **2001,** 123, (13), 3165-3166.

39. Duan, X. F.; Lieber, C. M., General synthesis of compound semiconductor nanowires. *Advanced Materials* **2000,** 12, (4), 298-302.

40. Shi, W. S.; Zheng, Y. F.; Wang, N.; Lee, C. S.; Lee, S. T., Synthesis and microstructure of gallium phosphide nanowires. *Journal of Vacuum Science & Technology B* **2001,** 19, (4), 1115-1118.

41. Morales, A. M.; Lieber, C. M., A laser ablation method for the synthesis of crystalline semiconductor nanowires. *Science* **1998,** 279, (5348), 208-211.

42. Zhang, R. Q.; Lifshitz, Y.; Lee, S. T., Oxide-assisted growth of semiconducting nanowires. *Advanced Materials* **2003,** 15, (7-8), 635-640.

43. Chen, X. H.; Xu, J.; Wang, R. M.; Yu, D. P., High-quality ultra-fine GaN nanowires synthesized via chemical vapor deposition. *Advanced Materials* **2003,** 15, (5), 419-421.

44. Heath, J. R.; Legoues, F. K., A Liquid Solution Synthesis of Single-Crystal Germanium Quantum Wires. *Chemical Physics Letters* **1993,** 208, (3-4), 263-268.

45. Wang, X.; Li, Y. D., Selected-control hydrothermal synthesis of alpha- and beta-MnO2 single crystal nanowires. *Journal of the American Chemical Society* **2002,** 124, (12), 2880-2881.

46. Lu, Q. Y.; Gao, F.; Zhao, D. Y., One-step synthesis and assembly of copper sulfide nanoparticles to nanowires, nanotubes, and nanovesicles by a simple organic amine-assisted hydrothermal process. *Nano Letters* **2002,** 2, (7), 725-728.

47. Xie, Y.; Yan, P.; Lu, J.; Wang, W. Z.; Qian, Y. T., A safe low temperature route to InAs nanofibers. *Chemistry of Materials* **1999,** 11, (9), 2619-2622.

48. Li, Y. D.; Sui, M.; Ding, Y.; Zhang, G. H.; Zhuang, J.; Wang, C., Preparation of Mg(OH)(2) nanorods. *Advanced Materials* **2000,** 12, (11), 818-821.

49. Wang, W. Z.; Geng, Y.; Yan, P.; Liu, F. Y.; Xie, Y.; Qian, Y. T., A novel mild route to nanocrystalline selenides at room temperature. *Journal of the American Chemical Society* **1999,** 121, (16), 4062-4063.

50. Sun, Y. G.; Xia, Y. N., Shape-controlled synthesis of gold and silver nanoparticles. *Science* **2002,** 298, (5601), 2176-2179.

51. Bradley, J. S.; Tesche, B.; Busser, W.; Masse, M.; Reetz, R. T., Surface spectroscopic study of the stabilization mechanism for shape-selectively synthesized nanostructured transition metal colloids. *Journal of the American Chemical Society* **2000,** 122, (19), 4631-4636.

52. Sun, Y. G.; Gates, B.; Mayers, B.; Xia, Y. N., Crystalline silver nanowires by soft solution processing. *Nano Letters* **2002,** 2, (2), 165-168.

53. Sun, Y. G.; Xia, Y. N., Large-scale synthesis of uniform silver nanowires through a soft, self-seeding, polyol process. *Advanced Materials* **2002,** 14, (11), 833-837.

54. Sun, Y. G.; Yin, Y. D.; Mayers, B. T.; Herricks, T.; Xia, Y. N., Uniform silver nanowires synthesis by reducing AgNO3 with ethylene glycol in the presence of seeds and poly(vinyl pyrrolidone). *Chemistry of Materials* **2002,** 14, (11), 4736-4745.

55. Peng, X. G.; Manna, L.; Yang, W. D.; Wickham, J.; Scher, E.; Kadavanich, A.; Alivisatos, A. P., Shape control of CdSe nanocrystals. *Nature* **2000,** 404, (6773), 59-61.

56. Golden, J. H.; Deng, H. B.; Disalvo, F. J.; Frechet, J. M. J.; Thompson, P. M., Monodisperse Metal-Clusters 10-Angstroms in Diameter in a Polymeric Host - the Monomer-as-Solvent Approach. *Science* **1995,** 268, (5216), 1463-1466.

57. Golden, J. H.; DiSalvo, F. J.; Frechet, J. M. J.; Silcox, J.; Thomas, M.; Elman, J., Subnanometer-diameter wires isolated in a polymer matrix by fast polymerization. *Science* **1996,** 273, (5276), 782-784.

58. Gates, B.; Yin, Y. D.; Xia, Y. N., A solution-phase approach to the synthesis of uniform nanowires of crystalline selenium with lateral dimensions in the range of 10-30 nm. *Journal of the American Chemical Society* **2000,** 122, (50), 12582-12583.

59. Gates, B.; Mayers, B.; Cattle, B.; Xia, Y. N., Synthesis and characterization of uniform nanowires of trigonal selenium. *Advanced Functional Materials* **2002,** 12, (3), 219-227.

60. Mayers, B.; Gates, B.; Yin, Y. D.; Xia, Y. N., Large-scale synthesis of monodisperse nanorods of Se/Te alloys through a homogeneous nucleation and solution growth process. *Advanced Materials* **2001,** 13, (18), 1380-1384.

61. Tang, Z. Y.; Kotov, N. A., One-dimensional assemblies of nanoparticles: Preparation,

properties, and promise. *Advanced Materials* **2005,** 17, (8), 951-962.

62. Hornyak, G.; Kroll, M.; Pugin, R.; Sawitowski, T.; Schmid, G.; Bovin, J. O.; Karsson, G.; Hofmeister, H.; Hopfe, S., Gold clusters and colloids in alumina nanotubes. *Chemistry-a European Journal* **1997,** 3, (12), 1951-1956.

63. Yin, Y. D.; Lu, Y.; Gates, B.; Xia, Y. N., Template-assisted self-assembly: A practical route to complex aggregates of monodispersed colloids with well-defined sizes, shapes, and structures. *Journal of the American Chemical Society* **2001,** 123, (36), 8718-8729.

64. Yin, Y. D.; Xia, Y. N., Self-assembly of spherical colloids into helical chains with well-controlled handedness. *Journal of the American Chemical Society* **2003,** 125, (8), 2048-2049.

65. Kimizuka, N., Towards self-assembling inorganic molecular wires. *Advanced Materials* **2000,** 12, (19), 1461-1463.

66. Lu, Y.; Yin, Y. D.; Mayers, B. T.; Xia, Y. N., Modifying the surface properties of superparamagnetic iron oxide nanoparticles through a sol-gel approach. *Nano Letters* **2002,** 2, (3), 183-186.

67. Reneker, D. H.; Yarin, A. L.; Fong, H.; Koombhongse, S., Bending instability of electrically charged liquid jets of polymer solutions in electrospinning. *Journal of Applied Physics* **2000,** 87, (9), 4531-4547.

68. Dzenis, Y., Spinning continuous fibers for nanotechnology. *Science* **2004,** 304, (5679), 1917-1919.

69. Spivak, A. F.; Dzenis, Y. A., A condition of the existence of a conductive liquid meniscus in an external electric field. *Journal of Applied Mechanics-Transactions of the Asme* **1999,** 66, (4), 1026-1028.

70. Yarin, A. L.; Koombhongse, S.; Reneker, D. H., Taylor cone and jetting from liquid droplets in electrospinning of nanofibers. *Journal of Applied Physics* **2001,** 90, (9), 4836-4846.

71. Yarin, A. L.; Koombhongse, S.; Reneker, D. H., Bending instability in electrospinning of nanofibers. *Journal of Applied Physics* **2001,** 89, (5), 3018-3026.

72. Spivak, A. F.; Dzenis, Y. A.; Reneker, D. H., A model of steady state jet in the electrospinning process. *Mechanics Research Communications* **2000,** 27, (1), 37-42.

73. Shin, Y. M.; Hohman, M. M.; Brenner, M. P.; Rutledge, G. C., Electrospinning: A whipping fluid jet generates submicron polymer fibers. *Applied Physics Letters* **2001,** 78, (8), 1149-1151.

74. Hong, P. D.; Chou, C. M.; He, C. H., Solvent effects on aggregation behavior of polyvinyl alcohol solutions. *Polymer* **2001,** 42, (14), 6105-6112.

75. Koski, A.; Yim, K.; Shivkumar, S., Effect of molecular weight on fibrous PVA produced by electrospinning. *Materials Letters* **2004,** 58, (3-4), 493-497.

76. Buchko, C. J.; Chen, L. C.; Shen, Y.; Martin, D. C., Processing and microstructural characterization of porous biocompatible protein polymer thin films. *Polymer* **1999,** 40, (26), 7397-7407.

77. Hendricks, C. D.; Carson, R. S.; Hogan, J. J.; Schneider, J. M., Photomicrography of Eletrically Sprayed Heavy Particles. *Aiaa Journal* **1964,** 2, (4), 733-737.

78. Larsen, G.; Velarde-Ortiz, R.; Minchow, K.; Barrero, A.; Loscertales, I. G., A method for making inorganic and hybrid (organic/inorganic) fibers and vesicles with diameters in the submicrometer and micrometer range via sol-gel chemistry and electrically forced liquid jets. *Journal of the American Chemical Society* **2003,** 125, (5), 1154-1155.

79. Dai, H. Q.; Gong, J.; Kim, H.; Lee, D., A novel method for preparing ultra-fine alumina-borate oxide fibres via an electrospinning technique. *Nanotechnology* **2002,** 13, (5), 674-677.

80. Choi, S. S.; Lee, S. G.; Im, S. S.; Kim, S. H.; Joo, Y. L., Silica nanofibers from electrospinning/sol-gel process. *Journal of Materials Science Letters* **2003,** 22, (12), 891-893.

81. Ding, B.; Kim, H.; Kim, C.; Khil, M.; Park, S., Morphology and crystalline phase study of electrospun TiO2-SiO2 nanofibres. *Nanotechnology* **2003,** 14, (5), 532-537.

82. Guan, H. Y.; Shao, C. L.; Wen, S. B.; Chen, B.; Gong, J.; Yang, X. H., A novel method for preparing Co3O4 nanofibers by using electrospun PVA/cobalt acetate composite fibers as precursor. *Materials Chemistry and Physics* **2003,** 82, (3), 1002-1006.

83. Guan, H. Y.; Shao, C. L.; Chen, B.; Gong, J.; Yang, X. H., A novel method for making CuO superfine fibres via an electrospinning technique. *Inorganic Chemistry*

Communications **2003,** 6, (11), 1409-1411.

84. Viswanathamurthi, P.; Bhattarai, N.; Kim, H. Y.; Lee, D. R.; Kim, S. R.; Morris, M. A., Preparation and morphology of niobium oxide fibres by electrospinning. *Chemical Physics Letters* **2003,** 374, (1-2), 79-84.

85. Viswanathamurthi, P.; Bhattarai, N.; Kim, H. Y.; Lee, D. R., Vanadium pentoxide nanofibers by electrospinning. *Scripta Materialia* **2003,** 49, (6), 577-581.

86. Viswanathamurthi, P.; Bhattarai, N.; Kim, H. Y.; Lee, D. R., The photoluminescence properties of zinc oxide nanofibres prepared by electrospinning. *Nanotechnology* **2004,** 15, (3), 320-323.

87. Teo, W. E.; Ramakrishna, S., A review on electrospinning design and nanofibre assemblies. *Nanotechnology* **2006,** 17, (14), R89-R106.

88. Göpel, W.; Hesse, J.; Zemel, J. N., *Sensors: A Comprehensive Survey*. Weinheim, F.R.G: New York, 1989; Vol. 2.

89. Göpel, W.; Schierbaum, K., *Chemical and Biochemical Sensors*. Weinheim, FRG New York, 1992; Vol. 3.

90. Hirschfeld, T.; Callis, J. B.; Kowalski, B. R., Chemical Sensing in Process Analysis. *Science* **1984,** 226, (4672), 312-318.

91. Stetter, J.; Penrose, W., Understanding Chemical Sensors and Chemical Sensor Arrays (Electronic Noses): Past, Present, and Future. *Sensor Update* **2002,** 10, 189.

92. Kolmakov, A.; Moskovits, M., Chemical sensing and catalysis by one-dimensional metal-oxide nanostructures. *Annual Review of Materials Research* **2004,** 34, 151-180.

TABLES:

Table 1.1. Possible reactions at the chemical interface of chemical sensors (Adapted from [91]).

Chemical reaction at the interface	Example
Adsorption Physisorption Chemisorption	 A[gas]+S[surface site]=AS[surface] $Vads=Ae^{-dG/kT}$
Partitioning	$K=C_m/C_s$
Acid-base	$HA+KOH=H_2O+K^++A^-$
Precipitation	Ag^+[aq]+NaCl[aq]=AgCl[s]+Na^+[aq]
Ion exchange	H^+[aq]+Na^+[surface]=H^+[surface]+Na^+[aq]
Oxidation/reduction	$CO+1/2O_2=CO_2$

FIGURES:

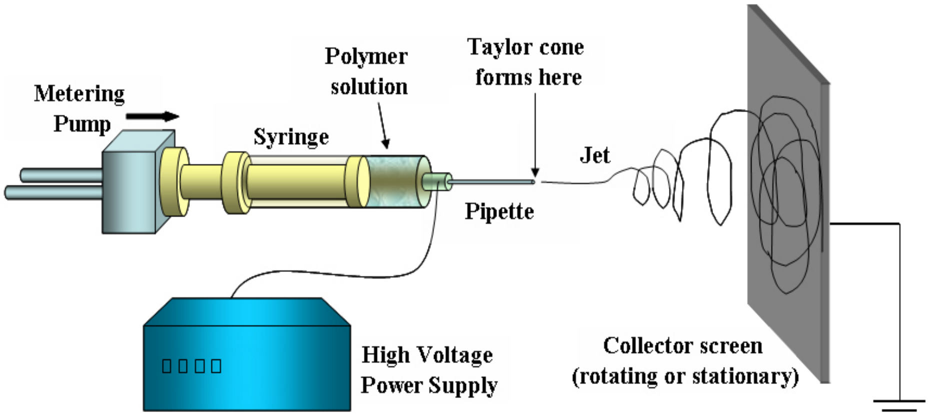

Figure 1.1. Schematic of the electrospinning setup.

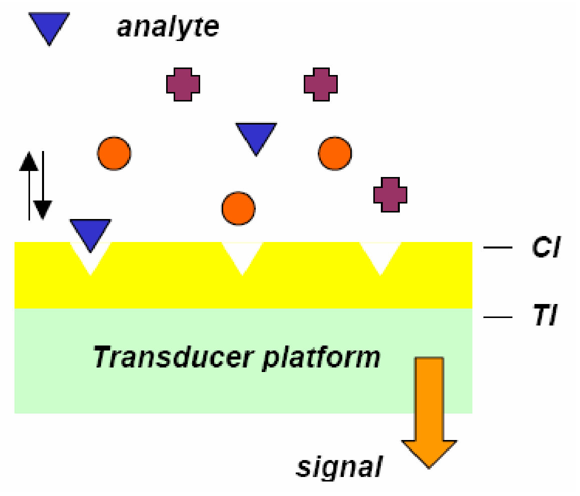

Figure 1.2. Cross-section of a chemical sensor. CI indicates the chemical interface, whereas TI indicates the transducer interface (Adapted from [91]).

CHAPTER 2

Polycrystalline Tungsten Oxide Nanofibers for Ammonia Sensing Applications

2.1 Introduction

Conductometric sensors based on semiconducting oxides have been the preferred low cost detectors for reducing gases. Metal oxides sensors (SnO_2, TiO_2, In_2O_3, WO_3) should be identified as different types within the 'class' of electrochemical-impedance sensors and are often called MOX sensors (from Metal Oxide sensors). In their simplest configuration, MOX sensors consist of a substrate with a heater, electrodes and a sensitive layer in contact with the electrodes. There are some characteristics that make MOX sensors appealing for gas sensor users:

- Low cost, small size and ease of handling (compared to other gas sensors)
- Fast sensor response and recovery
- Robust construction and good mechanical strength
- Long operating life

On the other hand, they have some disadvantages that are still a matter of research (some of them being common to most of gas sensors):

- Poor selectivity
- Influence of humidity
- High power consumption

The operating principle of these devices is associated primarily with the adsorption of gas molecules on the surface of the semiconducting oxides inducing electric charge transport between the two materials, which changes the resistance of the oxide[1]. Ideally, the interaction of the gaseous molecules will induce a change in the depletion layer of the metal oxide grain. These changes are transduced into an electrical signal depending on the microstructure of the sensitive film (the transducer). The porosity of the film, the grain size and the different grain intersections will determine the output signal, which takes into account the whole sensitive layer. The output signal is usually electric, although the measurement of the thermo-voltage or of the changes in the sensor temperature is also possible.

As discussed above, the transducer mechanism in thin films is usually surface-controlled. Transduction in porous films is highly dependent on grain size and the formation of different necks between grains. Therefore, the utility of nanostructured transition-metal oxides as gas sensing elements has been attracting more and more attention [2-4]. The reduction of the crystallite size beyond the “nano” size can result in a greater proportion of crystallite surface atoms, which are more prone to react with the surrounding ambient or to exhibit unusual structural features. From another point of view, two different microstructures of the sensitive film can be described for MOX gas sensors: compact layers (where the interaction of the gases take place mainly at the geometric surface, often obtained by the so called thin film techniques) and porous layers (where the interior volume is also accessible to the gas). With this in mind, the utility of nanofibers is preferred for conductimetric sensors because they provide a large surface-to-volume ratio which can result in excellent sensitivity, fast response and recovery time. In addition, better continuity of crystallites and alignment of wires can be achieved from such 1D nanostructures. The continuous 1D structure is expected to promote the conductivity of the oxide materials and therefore affect the temperature dependence of sensing. Compared with other nanostructures, 1D nanofibers are also easily configurable and integratable with conventional devices.

Since Seiyama and Taguchi used the dependence of the conductivity of ZnO on the gas present on the atmosphere for gas sensing applications [5], many different metal oxides have been proposed for gas detection. Generally speaking, these oxides can be divided into binary oxides and more complex oxides. The former is much more common in gas sensing applications. Among binary metal oxides, tin dioxide (SnO_2) is the one that has received by far the most attention due to its high reactivity to many gaseous species. However, this characteristic also manifests itself as a lack of selectivity, and thus investigation of other metal oxides has been considered necessary. In addition, the use of different MOX sensors is highly recommended in order to increase the amount of information.

As a wide-band-gap semiconductive metal oxide, tungsten oxide is most well-known as a catalyst. Tungsten trioxide exhibits a cubic perovskite-like structure based on the corner sharing of WO_6 regular octahedron, with the O atoms (W atoms) at the corner (centre) of each octahedron. This structure is also found in rhenium trioxide structure (ReO_3), from which it takes its common name (ReO_3-structure). Actually, the symmetry of tungsten oxide is lowered from the ideal ReO_3 structure by two distortions: tilting of WO_6 octahedron and displacement of tungsten from the centre of its octahedron [6]. Variations in the details of these distortions give rise to several phase transitions.

Another point worth noting is that the tungsten trioxide structure is likely to host several kinds of defects. One of the most elementary defects, as in most metal oxides, is the oxygen lattice vacancy, where an oxygen atom is absent from a normal lattice site. In the case of WO_3, the removal of oxygen causes the appearance of these crystallographic shear planes into the crystal along the [1m0] direction [7]. This leads to the formation of a family of WO_{3-x} compounds. From an electronic point of view, an oxygen vacancy causes the increase of the electronic density on the metallic (W) adjacent cations, leading to the formation of donor-like states slightly below the edge of the conduction band of the oxide, which acquires semiconducting properties [8].

Due to the structural specificity and the existence of large number of lattice defects, structural polymorphs of tungsten oxide exhibit manifold properties such as photochromic and electrochromic effects [9, 10]. These effects are bound up in the features that make a material sensitive to gases by modifying the surface conduction bands due to a change in the number of free electrons when a gas molecule interacts with a surface layer [11]. Shaver reported the first WO_3 gas sensor for detection of hydrogen [12]. These films were made by vacuum evaporation followed by oxidation in air at 600-750°C for several minutes. The films were then activated by Pt either by vacuum evaporation or by sprinkling platinum back on the surface of the oxide or momentarily blowing a stream of air or inert gas over a hot platinum hairpin and onto the film of the oxide. Akiyama et al prepared WO_3 films by pyrolysis of ammonium paratungstate ($(NH_4)_{10}W_{12}O_{41}.5H_2O$), ball milling and mixing to form a paste followed by sintering at 600°C for sensing NO and NO_2 [13]. The gases sensed were let in at various ppm ranging from 0-800ppm for NO and 0-250ppm for NO_2. The operating temperature was also varied to 200, 300 and 400ºC. Maekawa et al, found that WO_3 doped with Au showed excellent ammonia sensing properties [14]. The films were prepared in the same method adopted by Akiyama et al [13].

The films showed excellent sensitivity in the concentration range of 5ppb to 50ppm and were able to detect even 5ppb NH_3 in air.

Nanoscaled tungsten oxides prepared by sol-gel process have proved to have enhanced sensitivity for the detection of gases such as NO_x and NH_3. The specificity of the sensors can also be improved [11, 15]. However, the traditional sol-gel methods can only prepare discrete nano-scale tungsten oxide crystallites. Single crystalline tungsten oxide nanowires have been synthesized by a soft chemistry route [16]. The as-prepared nanowires appear in nano-bundles with diameters from 20 to 100 nm instead of well-defined individual nanofibers. However, these bundles exist in a disordered form. Although those tungsten oxide nanowires were determined to be non-stoichiometric compounds, it is still difficult to determine the real structures of them due to the high isotropic structures, which can only give diffraction in very limited directions. Other synthesis methods all involved in similar problems mentioned above. [17-19]

Electrospinning offers a relatively simple and versatile method for generating fibular microstructures [20-22]. As described in Chapter 1, this process involves in the production of continuous one-dimensional nanofibers under the electrostatic force of the charges on the surface of a liquid droplet in an electric field as strong as several kV/cm [23]. In this study, we have successfully prepared uniform inorganic-polymer composite nanofibers by electrospinning DMF solutions containing a polymer of high molecular weight and tungsten isopropoxide sol-gel solution. Pure tungsten oxide nanofibers were obtained by removing the organic phase via calcination of the composite nanofibers in air.

In this chapter, the electrospinning parameters (such as electrospinning voltage, working distance, solution flow rate, and etc.) for the polymer/ tungsten isopropoxide sol-gel solution were originally and systematically investigated and optimized. The structure evolution from composite fibers to tungsten oxide ceramic nanofibers has been investigated by synchrotron based *in situ* XRD for the first time. The gas sensing properties of the nano-porous mat composed of tungsten oxide nanofibers have been studied, showing this unique morphology of tungsten oxide nanofibers as potential candidates for the detection of low levels of NH_3.

2.2 Experimental

2.2.1 Materials

Poly(vinyl acetate) (PVAc, Mw=500,000) was obtained from Sigma-Aldrich. Tungsten isopropoxide ($W(iPr)_6$) sol-gel was purchased from the Alfa-Acer Company with a concentration of 5% w/v in propanol. Dimethylformamide (DMF) (certified A.C.S., Fisher Scientific Inc.) was utilized as a solvent to prepare the electrospinning solution. These chemicals were used without further purification.

2.2.2 Preparation of PVAc/tungsten oxide composite nanofibers

PVAc was dissolved in DMF at a concentration of 22% (w/v). Tungsten isopropoxide sol-gel was then added into the PVAc/DMF solution at various volume concentrations of 20%, 25%, 30%, and 35%, respectively. The mixtures were stirred and ultrasonically agitated for 24 hours to form homogeneous solutions for electrospinning. The experimental setup was described elsewhere [24]. Briefly, the $PVAc/W(iPr)_6$ blend solution was loaded in a 5 ml glass syringe (Popper & Sons, Inc.) attached to a syringe pump (KDS200, KD Scientific Inc.) which provided a steady solution flow rate of

20ul/min during electrospinning. A high voltage power supply (Gamma High Voltage Research, 0-30 kV) was employed to generate a high potential of 11kV to a 25 gauge blunt end syringe needle (I.D. 0.26mm, Popper & Sons Inc.). The electrospun nanofibers were collected onto silicon wafers which were horizontally placed 12 cm away from the spinneret.

2.2.3 Preparation of tungsten oxide ceramic nanofibers

Tungsten oxide ceramic nanofibers were prepared by calcining the as-spun PVAc/W(iPr)$_6$ composite fibers in a tube furnace. Figure 2.1 shows the temperature profile during the calcination process. The slow heating rate between 300 and 500^{o}C was selected to ensure the removal of organic phase without destroying the nanofibrillar structure and to avoid the disintegration of the ceramic nanofibers.

2.2.4 Characterization

a) SEM and TEM

The surface morphology of tungsten oxide nanofibers was characterized using SEM (LEO 1550) at an accelerating voltage of 15 kV. At least 200 fibers were selected randomly from the SEM micrographs to calculate the fiber diameter distribution. The elements composed of the nanofibers were analyzed using Energy Dispersive X-ray Spectroscopy (EDX). A Philips CM12 TEM with a LaB$_6$ filament at 120kV was employed to investigate the interior structure of the tungsten oxide nanofibers.

b) Structural characterization by x-ray diffraction

Grazing Incidence XRD (GIXRD) is a technology which is particularly suitable for thin film characterization [25, 26]. By increasing the path length of the incidence X-ray beam through the film, the diffraction intensity from the film can be increased so that a better signal-to-noise ratio can be obtained and conventional phase identification analysis can be run. In this project, we combined the advantages of both synchrotron radiation and the grazing incidence XRD to investigate the structure of metal oxide nanowires (see Figure 2.2). The highly collimated synchrotron beams at NSLS at Brookhaven National Lab (BNL) has been used as the incidence x-ray beam. The stationary incident beam makes a very small angle with the sample surface (typically 2^{o} to 5^{o}), which increases the path length of the x-ray. There is expected to be a dramatic increase signal to the background noise ratio from the film.

The structural evolution of the nanostructured metal oxide fibers has been studied by *in situ* x-ray diffraction [27-29]. XRD data were collected at beamline X18A at the National Synchrotron Light Source (NSLS) at the Brookhaven National Lab. A heating cell for *in situ* XRD study has been designed as shown in Figure 2.3. This cell consists of two parts: mechanical part and heating system.

For the mechanical part, brass is used for the main body, because of ease of machining and can have enough strength at temperatures even the part of heating cell is higher than $1000^{o}C$. Two blocks of brass were connected by two stainless steel rods. The blocks can slide along the rod rails. They can also be set at a certain position along the rails by set-screws. Swagelocks, which are widely used in vacuum industry, are used as connectors between the brass ends and quartz capillaries. Using a rubber ferrel inside the swagelock, we can seal the connection part, so that we can study the phase transition under a certain atmosphere in a sealed system. Thin-wall quartz capillaries and single crystal sapphire capillaries were used as the chamber to hold the sample. The heating system mainly consisted of a Ni-Cr resistance wire, conductive wires and temperature control system. Ni-Cr resistance wire, with resistance of around 8 ohms, was coiled around the quartz capillary (afterward, it was changed to a coiled around a small Al_2O_3 rod right below the capillary as a heater, in order to make a more stable heat source). A very thin k-type thermal couple was inserted inside the capillary (close to the position for the sample) so as to measure the real time temperature. At the beginning, temperature was controlled manually by adjusting the output current from a power supply. And later on, a temperature controller was used in order to control the temperature automatically with programmed temperature process. Schematic of the diffraction geometry is shown in Figure 2.4.

c) Sensitivity measurements

The tungsten oxide nanofibers were deposited onto an alumina chip (1×1cm) to test the gas sensitivity. The chip was standard microfabricated with interdigitated electrodes deposited on one side (acquired from CWRU). The gases used in the sensing test were UHP nitrogen (Praxair), UHP oxygen (Praxair), 1000ppm ammonia in nitrogen (BOC gases). The cumulative pressure inside the test chamber was kept at constant 1 atmosphere. As shown in Figure 2.5, the concentration of ammonia was changed by controlling their flow rates in conjunction with the flow rate of mixed gas of nitrogen and oxygen (4:1). The gases were controlled through 1479 MKS Mass flow controllers. A Lindberg/Blue tube furnace was used for programmed heating. The change in resistance of the sensor was measured and calculated in terms of voltage change across it by using an Agilent 34401A digital multimeter.

2.3 Results and Discussion

2.3.1 Optimization of the electrospinning process parameters

Because the morphology of the tungsten oxide nanofiber after calcination is largely determined by the polymer/W(iPr)$_6$ composite nanofibers before calcination, it is necessary to determine the relationship between the electrospinning process parameters and the morphology of the composite nanofibers, and to obtain thin fibers with uniform diameters in a controllable manner. 0.55 g PVAc (Mw=500,000, Aldrich) was dissolved in 2.5 ml dimethylformamide (DMF, Alfa Acer) and magnetically stirred for 1 hour to get a uniform and viscous solution (22 wt %). This PVAc solution was mixed with the sol-gel solution mentioned above based on a volume ratio of 5:2. The mixed solution was stirred and ultrasonically agitated for 24 hour to form a uniformly mixed solution. The process parameters were adjusted to the following values for detailed investigation: Voltage, 10kv, 12kv and 15kV; Flow rate, 5, 10 and 20 μ l/min, as tabulated below; Working distance, fixed at 12 cm. Al foils were used as collector.

The configuration of the as-prepared composite fibers is shown in Figure 2.6, from which it can be seen clearly: for the working voltage of 15kv, there is an obvious tendency that the higher the flow rate, the larger the average diameter of the fiber (see Figure 2.6 (A), (C), and (E)). As the flow rate goes low enough, such as below 5μl/min, the diameters of the fibers become non-uniform (see Figure 2.6 (A)). A lot of ultra-fine fibers form, co-existing with thicker fibers. Or in another word, the diameter distribution of the fibers is very discrete. But for the working voltage of 10kv, there is no such tendency (see Figure 2.6 (B), (D) and (F)). The relationship between flow rate and the fiber dimension is not so well defined. When considering the effect of working voltage, the flow rate was kept at 5μl/min (see Figure 2.6 (A), (B) and (G)). SEM images show that the higher the voltage is, the smaller the average diameters are. A summary of the processing parameters for the composite fibers in Figure 2.6 is listed in Table 2.1. The dependence of the average fiber diameter on the applied voltages and flow rate and has been plotted in Figure 2.7 and 2.8 respectively.

2.3.2 Morphology control on tungsten oxide ceramic nanofibers after calcination

In the electrospinning process, the accumulation of electrostatic charges on the surface of the liquid droplet at the spinneret induces the formation of a jet, which is subsequently stretched to form a continuous ultra thin fiber. During the stretching of the jet and the formation of the ultrathin fibers, the formation of larger surface area make it possible for the incorporated $W(iPr)_6$ to experience the following hydrolysis reaction:

$$W(iPr)_6 + H_2O \rightarrow W(OH)_6 + ROH \qquad (1)$$

where ROH stands for isopropanol, which is easy to evaporate in the electrospinning process. Therefore, we obtained a non-woven mats composed of the polymer/inorganic hybrid nanofibers and characterized by high surface area and small pore size.

In order to find the proper solution parameters for producing tungsten oxide nanofibers, tungsten isopropoxide was mixed with PVAc/DMF solution in various volume ratios as mentioned in the experimental section. These solutions were loaded into syringes for electrospinning. The morphologies of the samples before and after heat treatment are shown in Figure 2.9.

Comparing Figure 2.9(A)(C)(E)(G), composite fibers with uniform diameters are ready to form with a proper ratio of W(iPr)$_6$ (or precisely, concentration of PVAc). Within a proper range, the higher concentration of PVAc, the thicker composite fibers are. However, the morphologies of ceramic fibers after calcination are more directly related with the content of W(iPr)$_6$. Figure 2.9(B) is the product of sample with 20% W(iPr)$_6$. Discrete tungsten oxide ceramic grains all deposit on the substrate, with the grain size of tens of nanometers or even less. This result is like the product from the tungsten isopropoxide sol-gel. Continuous nanofibers cannot form due to the low concentration of tungsten oxide precursor. As the precursor concentration increases, continuous ceramic fibers with uniform diameters were obtained after the heat treatment (see Figure 2.9(D)(F)(H)). Their diameters are all within or around 100 nm and they appear to be polycrystalline fibers composed by obvious crystalline grains. And there are obvious differences between them: the higher the concentration of W(iPr)$_6$, the more solid the fibers seem and the better the continuity they have.

Figure 2.10(A) shows the low magnification SEM image of the as-prepared PVAc/WO$_3$ composite nanofibers (25% W(iPr)$_6$， named sample W2) before calcination. Each individual fiber is uniform in cross section, and the average diameter of this sample is around 200nm. After the polymer template was selectively removed by burning the sample in air at 500^{o}C (see Figure.2.10 (B)), metal oxide nanofibers were left, remaining the continuous structures but with a reduced diameter size, most of which were less than 100nm. The size reduction can be attributed to the loss of PVAc from the nanofibers and the crystallization of tungsten oxide. Size distributions of the nanofibers before and after heat treatment are shown in Figure 2.10 (C) and (D).

TEM images of the sample W2 before and after calcination have been shown in Figure 2.11. TEM pictures show that the darkness along the fiber was uniform, implying that the tungsten oxide sol-gel was distributed uniformly within the polymer template, so that it is possible to obtain continuous ceramic nano-fibers after removing the polymer template. The diameters of the composite fibers are around 200nm. The TEM image of the sample after calcination shows a grained fiber structure with relatively uniform diameters of around 80 nm. The grains are crystalline tungsten oxide with grain sizes less than 20 nm. Selected area electron diffraction (SAED) pattern of the sample (see inset in Figure 2.11 (B)) indicated the polycrystalline configuration of the tungsten oxide nanofiber after calcinations. EDX spectrum confirmed that the only elements in the sample after calcination were tungsten and oxygen, implying the polymer had been removed completely.

Grazing incidence X-ray diffraction was carried out at beam site X18A at NSLS with the grazing angle= 3^o. The diffraction spectra of WO_3 (see Figure 2.12) can be indexed as orthorhombic phase (JCPDS #89-4479) with structure parameters as follows: a=7.361(Å), b=7.574(Å), c=7.762(Å), $\alpha=90^o$, $\beta=90^o$, $\gamma=90^o$. The width of the peaks is broad (see diffraction peaks (120), (112) and (222)), implying that the diffraction crystallites have pretty small sizes in the order of nano-scale, which is in agreement with the SEM results. We fit the diffraction spectra and did some calculation of the particle sizes by using the software Bede Polycrystal based on the Sherrer Formula. The software gives the average particle size of 42 nm calculated by fitting the peaks based on Lorentzian peak function.

The PVAc/W(iPr)$_6$ composite nanofibers have also been deposited on Al_2O_3 plate, which is a non-conductive substrate for making gas-sensing chip. Same WO_3 ceramic nanofibers were obtained after careful calcination, as shown in Figure 2.13. By extending the deposition time, a thicker layer of WO_3 nanofibers were obtained in the form of porous mats (see Figure 2.14 and 2.15). The continuous 1D WO_3 nanofibers constitute a layer of nanoporous network with a considerably large specific area, which provides an ideal interface for a full interaction between the chemical sensor and the gas molecules.

In general, this synthetic route has little requirement for the substrate. It is also applicable for producing other ceramic nanofibers with different phases by using different sol-gel solutions and a good control of the heat treatment process [20-23]. Alignment of the 1-D nanofibers is also possible by means of various electrical or mechanical methods [30-34].

2.3.3 Synchrotron based *in situ* x-ray diffraction

As the formation of nanostructured tungsten oxide involves a continuous temperature increase process, a dynamic structure evolution might be happening in the whole process. Studies of the structural transformations may be performed using quenching experiments, but this information is only valid if the recovered material is not affected by any irreversible changes upon cooling. Therefore, sophisticated *in situ* techniques are required for their direct monitoring. In addition, the high brightness and high collimation of the synchrotron x-ray beam employed here can provide a satisfactory signal-to-noise ratio, so that it is possible to investigate very fine structures such as the nanostructured polycrystalline fibers in our research. The temperature-dependent formation of the tungsten oxide nanofibers was studied with synchrotron based *in situ* x-ray diffraction. A series of XRD spectrums were recorded as the temperature was ramped up from room temperature to 525°C, demonstrating the continuous transformation from amorphous nanocomposite phase into crystalline tungsten oxide phases. A continuous phase change process is shown in Figure 2.16(A) (2θ has been transformed based on the wavelength of 1.54056Å). Some representative diffraction spectra have been selected out and indexed (Figure 2.16 (B)) in the process of the formation of the metal oxide nanofibers from the nano-composite. Based on the information from the *in situ* XRD, the metal oxide obtained from the hydrolysis of the sol-gel precursor was amorphous in the as-prepared nano-composite. Tungsten oxide began to crystallize at around 300°C, forming a tetragonal phase at 348°C, (JCPDS# 89-1287). Two phase transitions occur at 360°C and 510°C respectively, forming a pure orthorhombic phase WO_3 in between 375°C and 500°C (JCPDS#89-4479), and tetragonal phase at 525°C (JCPDS# 89-4482). The phase transformations were gradual processes. A mixture of phases existed in the transformation process, but no intermediate phase existed. It is readily observed from the *in situ* XRD spectrum that the orthorhombic phase of tungsten oxide can exist over a relatively large temperature range (360~510°C), while the two tetragonal phases can only be stable over a small temperature range: around 348°C and 525°C respectively. Therefore, it is safe to conclude that we have obtained pure orthorhombic tungsten trioxide nanofibers after heat treatment at 500°C. A summary of the phases and their corresponding existing temperatures is listed in Table 2.2. It is noticed that the main effects observed as a function of temperature were size changes in the unit cells. The basic geometrical structures were close to each other through all temperature ranges. The transformation from tetragonal (I) to orthorhombic phase was only the result of size increase of the unit cell in the c axis (or in another word, symmetry decreased in the c axis), leading to the appearance of additional diffraction peaks at 23.47^o (020), 26.45^o (120), 33.53^o (202), 35.26^o (122). Unit cell symmetry increased gradually as temperature was increased to 525^{o}C, resulting in the disappearance of the peaks mentioned above and very small changes of diffraction peak positions. Based on our *in situ* XRD experiments, we also found that all phase transformation processes from low temperature to high temperature were irreversible. This means that the high temperature phases can exist in stable form at lower temperatures after their formation. It is notable that the phase transitions during the heating process were all second order transitions based on our thermal analysis results (see Figure 2.17).

2.3.4 Sensing test results

Tungsten trioxide has been reported to be weakly sensitive toward NH_3 compared with their superior sensing performance toward NO_x in the literature [35, 36]. However, the sensing performance of the material can be strongly affected by material microstructure, which can be modified by the preparation techniques. In this work, tungsten oxide nanofibers were prepared by sintering the PVAc/W(iPr)$_6$ composite fibers at 500^{o}C for three hours in order to remove the polymer template completely. We found that the as-prepared pure WO_3 nanofibers had a very quick response toward NH_3 at a very low concentration at an operating temperature of 350^{o}C. In terms of the *in situ* XRD results above, orthorhombic phase was the only phase that stably existed at this operating temperature for sensing test. Figure 2.18 shows the representative dynamic gas response of the tungsten oxide ceramic nanofibers to NH_3 pulse with the concentrations of 50, 100, 200 and 500ppm at 350°C. The resistance of the material decreases obviously with respect to the baseline in each NH_3 pulse. This experimental result agrees with the model developed by Moseley et al., [1] which predicted the reduction of resistance of an n-type semiconductor (such as WO_3) in presence of reductive gases (such as NH_3 here).

A detailed analysis of the sensing data (see Figure 2.19) indicated that the response time of our WO_3 nanofiber-based sensor is less than 20s. This response time toward NH_3 is much faster than those reported before for the tungsten trioxide prepared by other methods [15, 16, 19, 37]. This can be attributed to several factors. One is the porosity of the sample surface and large surface-to-volume ratio of the sample, which provide good accessibility of the gases to the sensing layers. This makes the adsorption of ammonia much easier. Another reason is the high purity of the material processed by sol-gel chemistry. Additionally, the strictly-controlled heat treatment secured the existence of pure orthorhombic phase as the only sensing material. If the sensor signal (S) is defined as the ratio $S= R_g/R_a$, where R_a is the resistance in air and R_g is the resistance in gas, the sensor signals as a function of the NH_3 concentration was plotted in Figure 2.20 (A). These data can be approximated by a equation in the form of $S = 1 + aC_{NH_3}{}^{b}$, where a and b are variables that can be fitted to a= (0.082±0.015) and b=(0.78±0.03). This result matches the sensor response law developed by Gurlo et al. [38], which gives the correlation between the sensor response (S) and the local gas concentration (C_{gas}).

The sensor response of the sample toward 100ppm NH_3 has been measured at different operating temperatures (Figure 2.20 (B)). The operating temperatures are below 500°C to avoid possible phase transformations at higher temperatures. The sensor signals for our WO_3 nanofiber network are not strongly temperature dependent for the temperature range under measurement, although the intensity of the signals has the tendency to decrease as temperature increases. However, a decreased operating temperature used to result in a longer response and recovery time in our measurement. This phenomenon has been explained as the slowing down of the kinetics of the gas-surface reaction at lower temperature [35]. The optimum operating temperature has to be determined for different application requirement.

2.4 Conclusions

Tungsten oxide ceramic nanofibers were successfully prepared using electrospinning and sol-gel chemistry with controllable diameters of around 100nm. The effects on the fiber configuration from system parameters and processing parameters have been studied in detail. The dependence of electrospun fibers' diameter sizes on the system and process parameters is pretty complicated. In general, higher applied voltage, higher feeding rate of the solution from the tip and higher concentration of polymer template can lead to larger fiber diameters. The uniformity of the fiber size distribution and the minimum diameter that fibers can be reached, are all dependent on specific cases and the intrinsic properties of the polymers themselves.

The continuous 1D nanofibrous tungsten oxides can be obtained after careful calcination of the composite fibers containing the $W(iPr)_6$ concentration above 25%. The morphology and structure of ceramic tungsten oxide nanofibers during calcination were strongly affected by temperature. A kinetic study based on *in situ* XRD showed that three typical phases, tetragonal phase (I), orthorhombic phase, and tetragonal phase (II) existed at 348, 375, and 525^{o}C respectively. Such insights are essential for optimizing the heat treatment temperatures to achieve specific tungsten oxide phases. It is also useful for selecting proper operating temperature for sensing test of the tungsten oxide polymorphs. The orthorhombic phase WO_3 nanofibers demonstrated a high sensitivity to ammonia with a wide range of concentrations, suggesting potential applications of the nanofibers as a sensor material in homeland security, environmental protection, and health care field. Optimum sensor performance can be expected for these WO_3 nanofiber networks by optimizing the fabrication process and selecting proper operating temperatures.

References

1. Moseley, P. T.; Crocker, A. J., *Sensor Materials*. Institute of Physics Pub.: Philadelphia 1996; p 69.

2. Guidi, V.; Boscarino, D.; Casarotto, L.; Comini, E.; Ferroni, M.; Martinelli, G.; Sberveglieri, G., Nanosized Ti-doped MoO3 thin films for gas-sensing application. *Sensors and Actuators B-Chemical* **2001,** 77, (1-2), 555-560.

3. Pan, Z. W.; Dai, Z. R.; Wang, Z. L., Nanobelts of semiconducting oxides. *Science* **2001,** 291, (5510), 1947-1949.

4. Walter, E. C.; Ng, K.; Zach, M. P.; Penner, R. M.; Favier, F., Electronic devices from electrodeposited metal nanowires. *Microelectronic Engineering* **2002,** 61-2, 555-561.

5. Seiyama, T.; Kato, A.; Fujiishi, K.; Nagatani, M., A New Detector for Gaseous Components Using Semiconductive Thin Films. *Analytical Chemistry* **1962,** 34, (11), 1502-1503.

6. Woodward, P. M.; Sleight, A. W.; Vogt, T., Ferroelectric tungsten trioxide. *Journal of Solid State Chemistry* **1997,** 131, (1), 9-17.

7. Kosuge, K., *Chemistry of non-stoichiometric compounds*. Oxford University Press: Oxford, 1994.

8. Nowotny, J.; Dufour, L., *Surface and near surfaces chemistry of oxides materials*. Elsevier: Amsterdam, 1988.

9. Salje, E., New Type of Electrooptic Effect in Semiconducting Wo3. *Journal of Applied Crystallography* **1974,** 7, (DEC1), 615-617.

10. Salje, E.; Viswanathan, K., Physical-Properties and Phase-Transitions in Wo3. *Acta Crystallographica Section A* **1975,** A 31, (MAY1), 356-359.

11. Gouma, P. I., Nanostructured Polymorphic Oxides for Advanced Chemsensors. *Reviews on advanced materials science* **2003,** 5, (2), 147.

12. Shaver, P. J., Activated Tungsten Oxide Gas Detectors. *Applied Physics Letters* **1967,** 11, (8), 255-257.

13. Akiyama, M.; Tamaki, J.; Miura, N.; Yamazoe, N., Tungsten Oxide-Based Semiconductor Sensor Highly Sensitive to No and No2. *Chemistry Letters* **1991**, (9), 1611-1614.

14. Maekawa, T.; Tamaki, J.; Miura, N.; Yamazoe, N., Gold-Loaded Tungsten-Oxide Sensor for Detection of Ammonia in Air. *Chemistry Letters* **1992**, (4), 639-642.

15. Prasad, A. K.; Gouma, P. I., MoO3 and WO3 based thin film conductimetric sensors for automotive applications. *Journal of Materials Science* **2003,** 38, (21), 4347-4352.

16. Polleux, J.; Gurlo, A.; Barsan, N.; Weimar, U.; Antonietti, M.; Niederberger, M., Template-free synthesis and assembly of single-crystalline tungsten oxide nanowires and their gas-sensing properties. *Angewandte Chemie-International Edition* **2006,** 45, (2), 261-265.

17. Gu, G.; Zheng, B.; Han, W. Q.; Roth, S.; Liu, J., Tungsten oxide nanowires on tungsten substrates. *Nano Letters* **2002,** 2, (8), 849-851.

18. Liu, Z. W.; Bando, Y.; Tang, C. C., Synthesis of tungsten oxide nanowires. *Chemical Physics Letters* **2003,** 372, (1-2), 179-182.

19. Li, X. L.; Lou, T. J.; Sun, X. M.; Li, Y. D., Highly sensitive WO3 hollow-sphere gas sensors. *Inorganic Chemistry* **2004,** 43, (17), 5442-5449.

20. Li, D.; Xia, Y. N., Electrospinning of nanofibers: Reinventing the wheel? *Advanced Materials* **2004,** 16, (14), 1151-1170.

21. Ding, B.; Kim, H.; Kim, C.; Khil, M.; Park, S., Morphology and crystalline phase study of electrospun TiO2-SiO2 nanofibres. *Nanotechnology* **2003,** 14, (5), 532-537.

22. Li, D.; Xia, Y. N., Fabrication of titania nanofibers by electrospinning. *Nano Letters* **2003,** 3, (4), 555-560.

23. Dzenis, Y., Spinning continuous fibers for nanotechnology. *Science* **2004,** 304, (5679), 1917-1919.

24. Ji, Y.; Li, B. Q.; Ge, S. R.; Sokolov, J. C.; Rafailovich, M. H., Structure and nanomechanical characterization of electrospun PS/clay nanocomposite fibers. *Langmuir* **2006,** 22, (3), 1321-1328.

25. Golovin, A. L.; Imamov, R. M.; Stepanov, S. A., Experimental-Study of X-Ray-Diffraction under Specular Reflection Conditions. *Acta Crystallographica Section A* **1984,** 40, (MAY), 225-228.

26. Dosch, H.; Batterman, B. W.; Wack, D. C., Depth-Controlled Grazing-Incidence Diffraction of Synchrotron X-Radiation. *Physical Review Letters* **1986,** 56, (11), 1144-1147.

27. Cahill, C. L.; Ko, Y. H.; Hanson, J. C.; Tan, K. M.; Parise, J. B., Structure of microporous QUI-MnGS-1 and *in situ* studies of its formation using time-resolved synchrotron x-ray powder diffraction. *Chemistry of Materials* **1998,** 10, (5), 1453-1458.

28. Christensen, A. N.; Jensen, T. R.; Norby, P.; Hanson, J. C., *In situ* synchrotron x-ray powder diffraction studies of crystallization of microporous aluminophosphates and Me2+-substituted aluminophosphates. *Chemistry of Materials* **1998,** 10, (6), 1688-1693.

29. Fernandez-Garcia, M.; Martinez-Arias, A.; Hanson, J. C.; Rodriguez, J. A., Nanostructured oxides in chemistry: Characterization and properties. *Chemical Reviews* **2004,** 104, (9), 4063-4104.

30. Inai, R.; Kotaki, M.; Ramakrishna, S., Structure and properties of electrospun PLLA single nanofibres. *Nanotechnology* **2005,** 16, (2), 208-213.

31. Xu, C.; Inai, R.; Kotaki, M.; Ramakrishn, S., Aligned biodegradable nanofibrous structure: a potential scaffold for blood vessel engineering *Biomaterials* **2004,** 25, (5), 877-866.

32. Sundaray, B.; Subramanian, V.; Natarajan, T. S.; Xiang, R. Z.; Chang, C. C.; Fann, W. S., Electrospinning of continuous aligned polymer fibers. *Applied Physics Letters* **2004,** 84, (7), 1222-1224.

33. Katta, P.; Alessandro, M.; Ramsier, R. D.; Chase, G. G., Continuous electrospinning of aligned polymer nanofibers onto a wire drum collector. *Nano Letters* **2004,** 4, (11), 2215-2218.

34. Li, D.; Herricks, T.; Xia, Y. N., Magnetic nanofibers of nickel ferrite prepared by electrospinning. *Applied Physics Letters* **2003,** 83, (22), 4586-4588.

35. Ponzoni, A.; Comini, E.; Sberveglieri, G.; Zhou, J.; Deng, S. Z.; Xu, N. S.; Ding, Y.; Wang, Z. L., Ultrasensitive and highly selective gas sensors using three-dimensional tungsten oxide nanowire networks. *Applied Physics Letters* **2006,** 88, (20).

36. Ponzoni, A.; Comini, E.; Ferroni, M.; Sberveglieri, G., Nanostructured WO3 deposited by modified thermal evaporation for gas-sensing applications. *Thin Solid Films* **2005,** 490, (1), 81-85.

37. Prasad, A. K. Study of Gas Specificity in MoO3/WO3 Thin Film Sensors and their Arrays. Stony Brook, Stony Brook, 2005.

38. Gurlo, A.; Barsan, N.; Ivanovskaya, M.; Weimar, U.; Gopel, W., In2O3 and MoO3-In2O3 thin film semiconductor sensors: interaction with NO2 and O-3. *Sensors and Actuators B-Chemical* **1998,** 47, (1-3), 92-99.

TABLES:

Table 2.1. Processing parameters for the PVAc/WO_3 composite fibers in Figure 2.6.

	15 kv	***10 kv***	***12 kv***
5µl/min	**(A)**	**(B)**	**(G)**
10µl/min	**(C)**	**(D)**	
20µl/min	**(E)**	**(F)**	

Table 2.2. Summary of the phases and their corresponding existing temperatures (RT: room temperature).

Phase	Temperature	JCPDS	a (Å)	b (Å)	c (Å)	$\alpha(^o)$	$\beta(^o)$	$\gamma(^o)$
Amorphous	RT	-	-	-	-	-	-	-
Tetragonal(I)	348°C	#89-1287	7.3900	7.3900	3.8800	90	90	90
Orthorhombic	375°C	#89-4479	7.3612	7.5739	7.7620	90	90	90
Tetragonal(II)	525°C	#89-4482	5.2806	5.2806	7.8496	90	90	90

FIGURES:

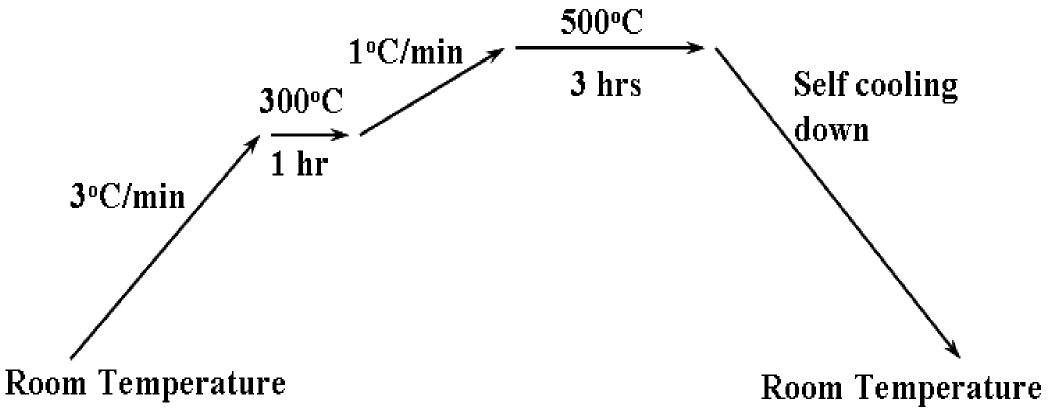

Figure 2.1. Temperature profile for the calcination process.

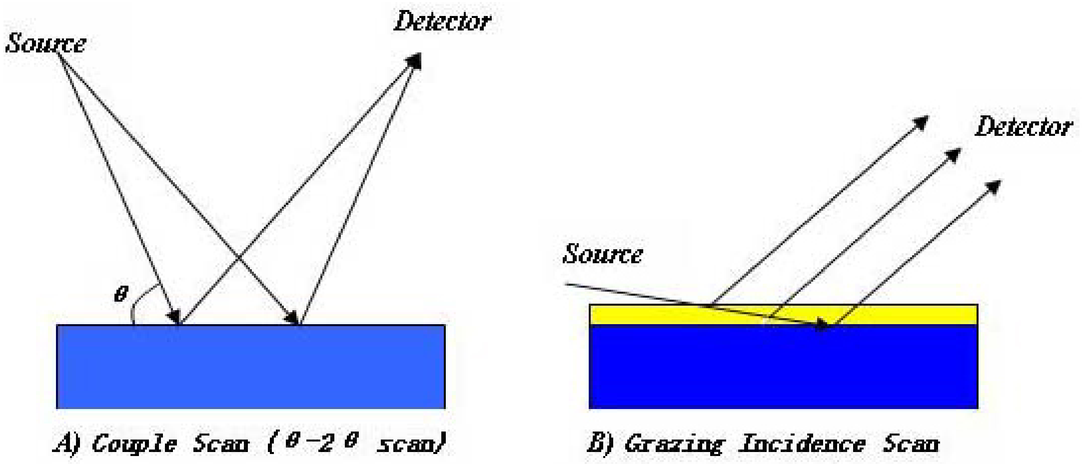

Figure 2.2. Geometries of couple scan for bulk analysis (A) and grazing incidence scan for thin film analysis (B).

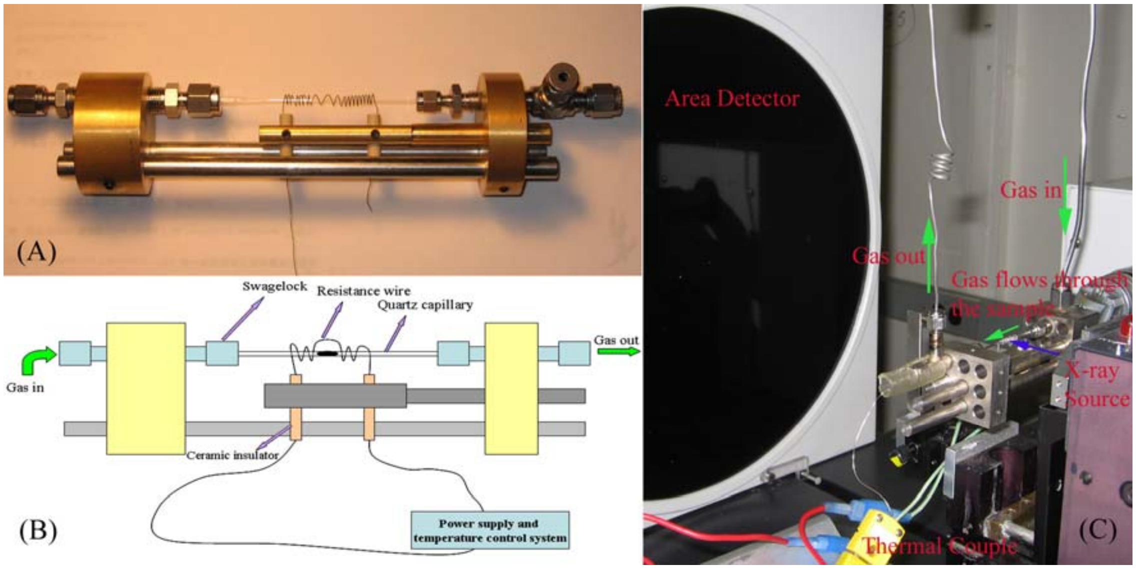

Figure 2.3. A) Heating cell design for *in situ* XRD; B) Schematic of the cell; C) *In situ* XRD set-up.

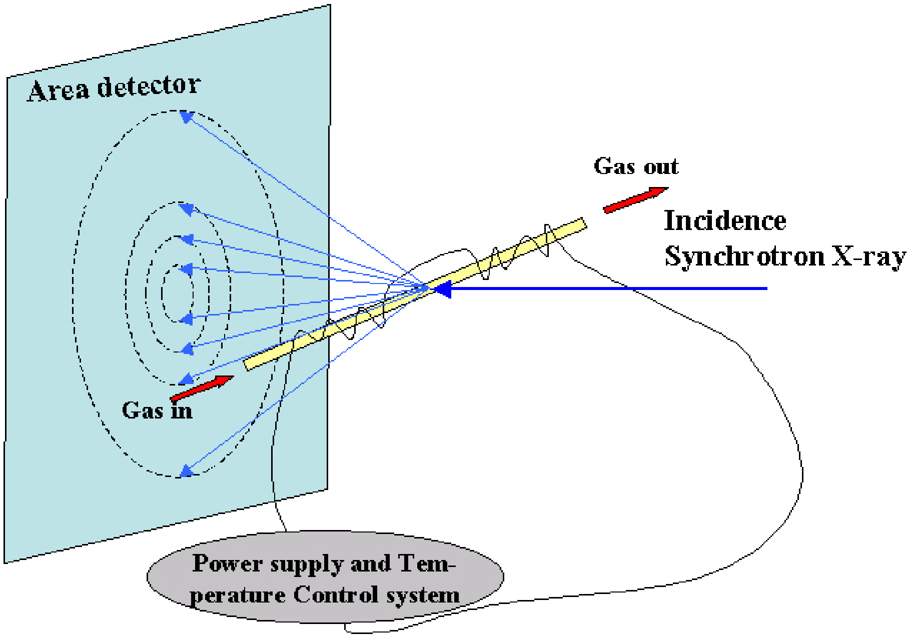

Figure 2.4. Schematic of the *in situ* XRD setup.

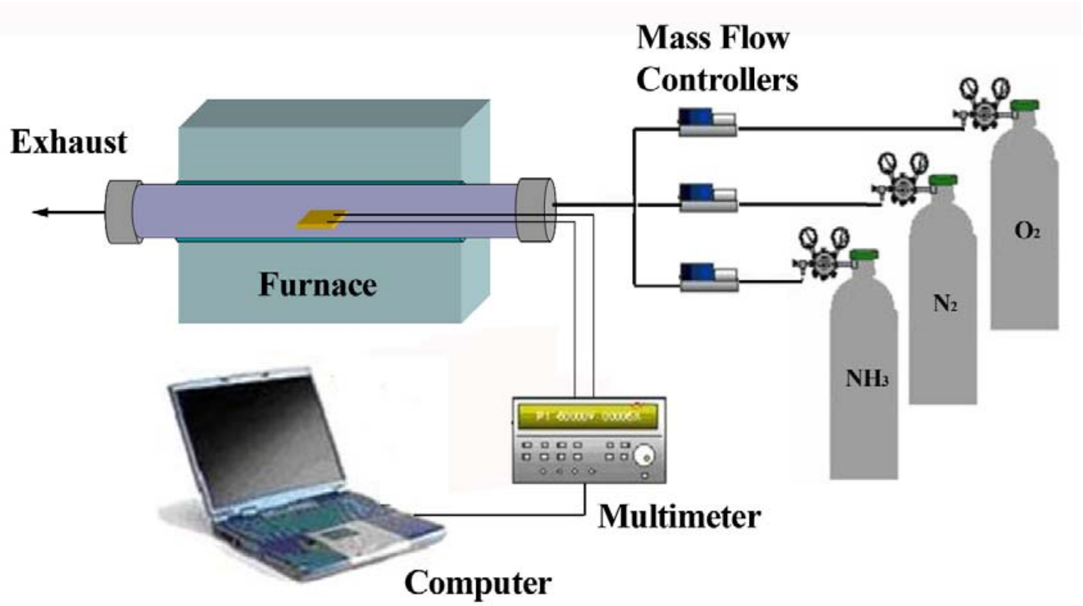

Figure 2.5. Schematic diagram of the experimental setup of the sensing system.

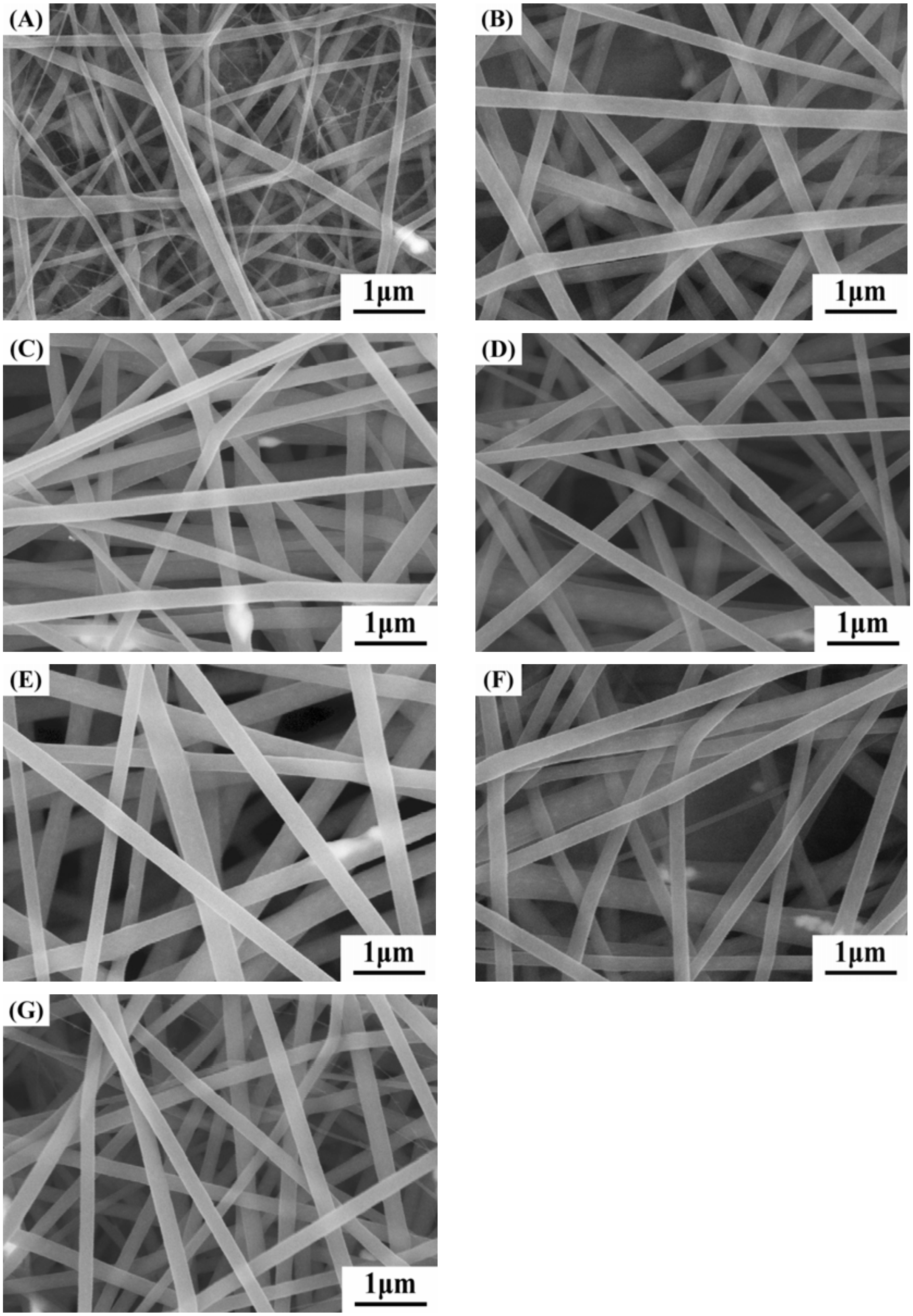

Figure 2.6. SEM images of the as-prepared PVAc/W(iPr)$_6$ composite fibers.

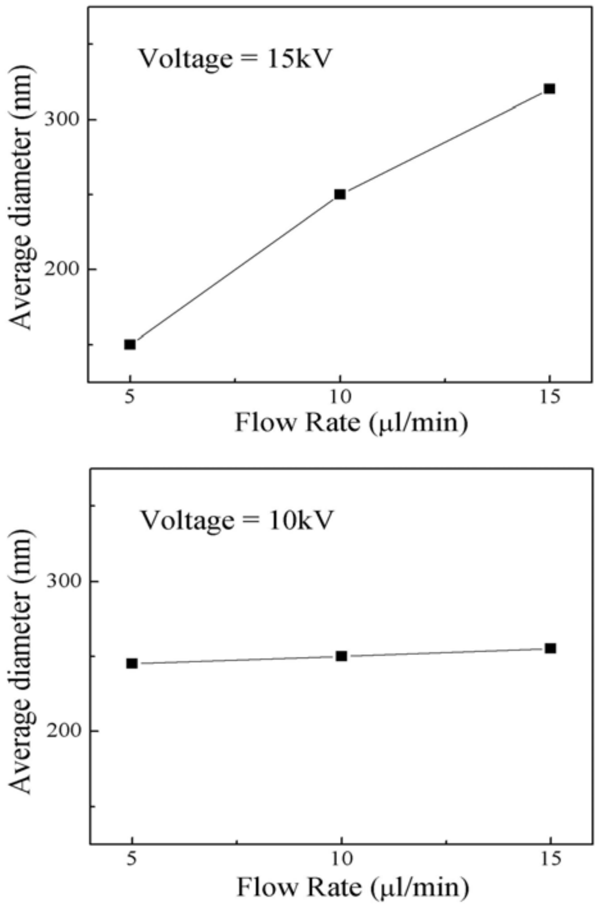

Figure 2.7. Dependence of average fiber diameter on the feeding rates.

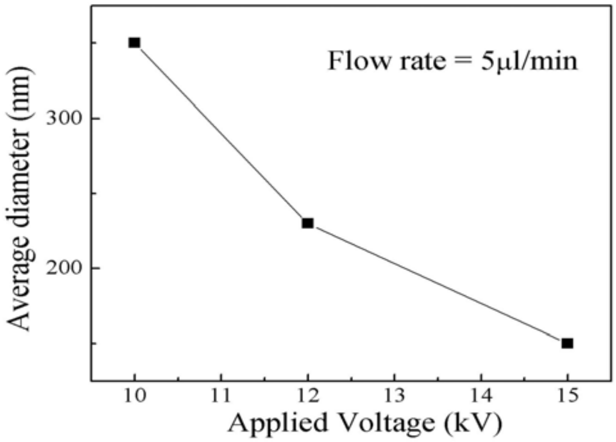

Figure 2.8. Dependence of average fiber diameters on the applied voltages of the solution.

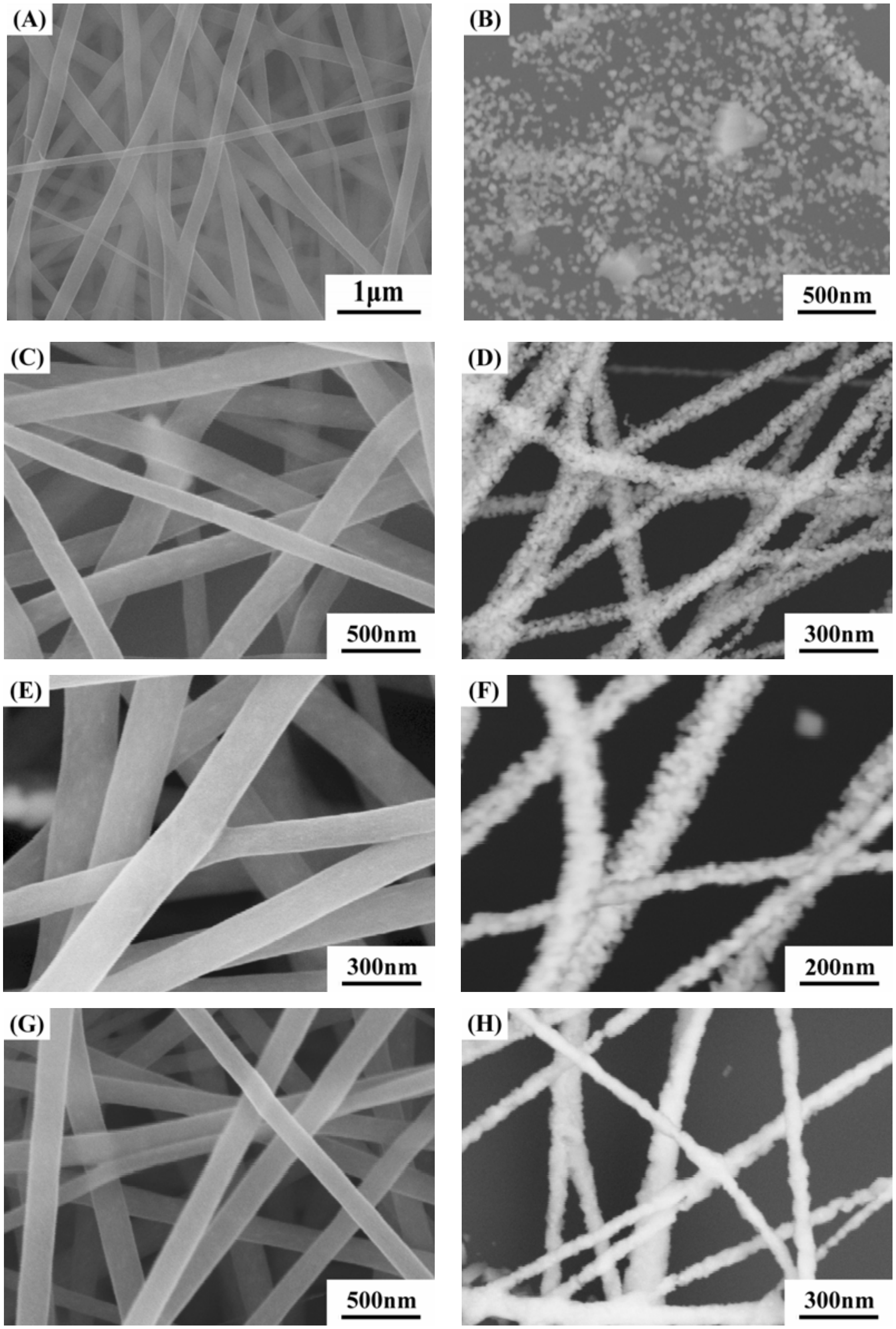

Figure 2.9. (A)(C)(E)(G): SEM images of the PVAc/WO_3 composite nanofibers with various $W(iPr)_6$ volume percentages of 20%, 25%, 30%, and 35%; and (B)(D)(F)(H): their corresponding products after calcination.

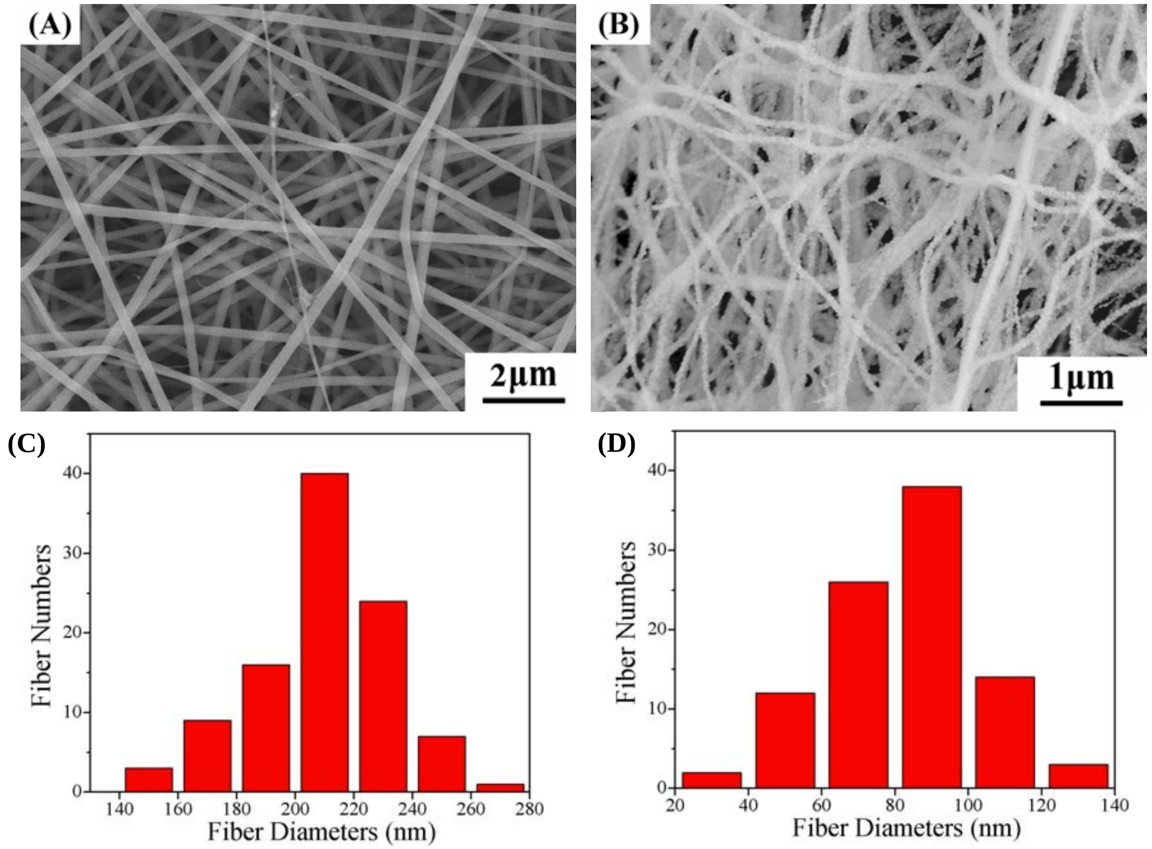

Figure 2.10. (A) SEM image of PVAc/WO_3 composite fibers of sample with 25% $W(iPr)_6$; (B) SEM image of the same sample after it had been calcined in air at 500°C for 3 hours; (C)(D) Size distributions of the nanofibers before and after calcination.

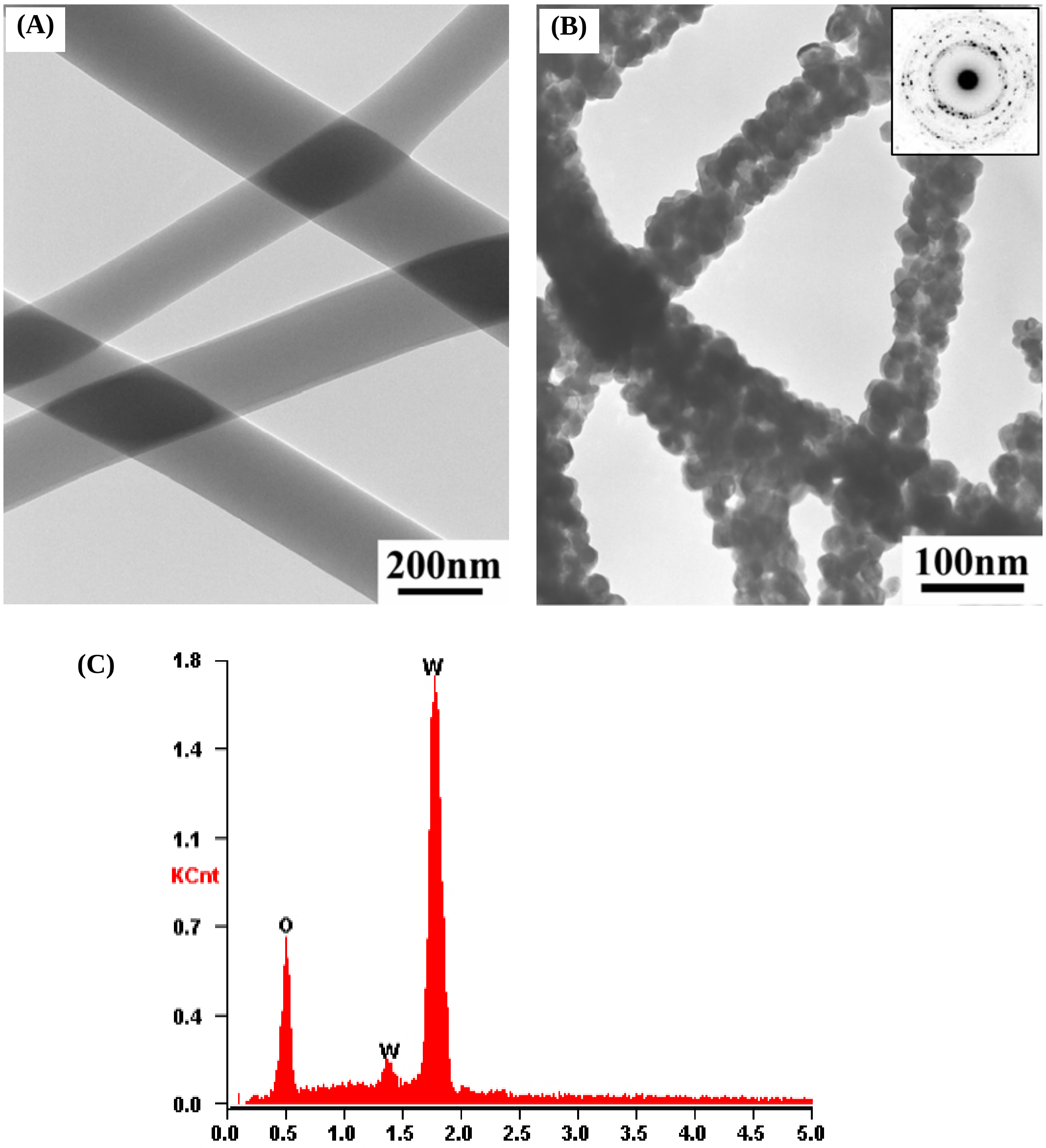

Figure 2.11. TEM images of the sample with 25% $W(iPr)_6$ before (A) and after (B) calcinations, inset in (B) is the SAED of the polycrystalline tungsten oxide nanofiber; (C) EDAX of the sample after calcination, showing it is pure tungsten oxide.

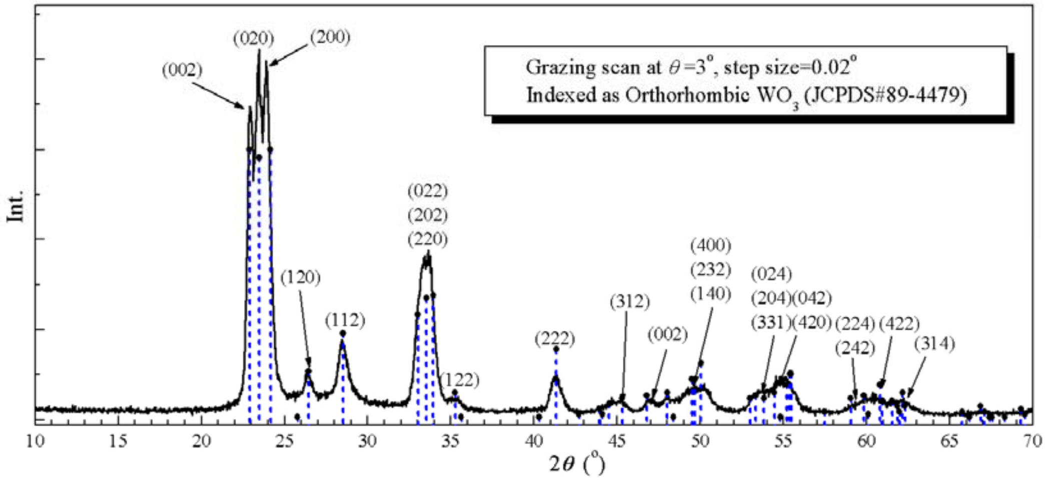

Figure 2.12. Grazing incidence XRD of the WO_3 nanofibers.

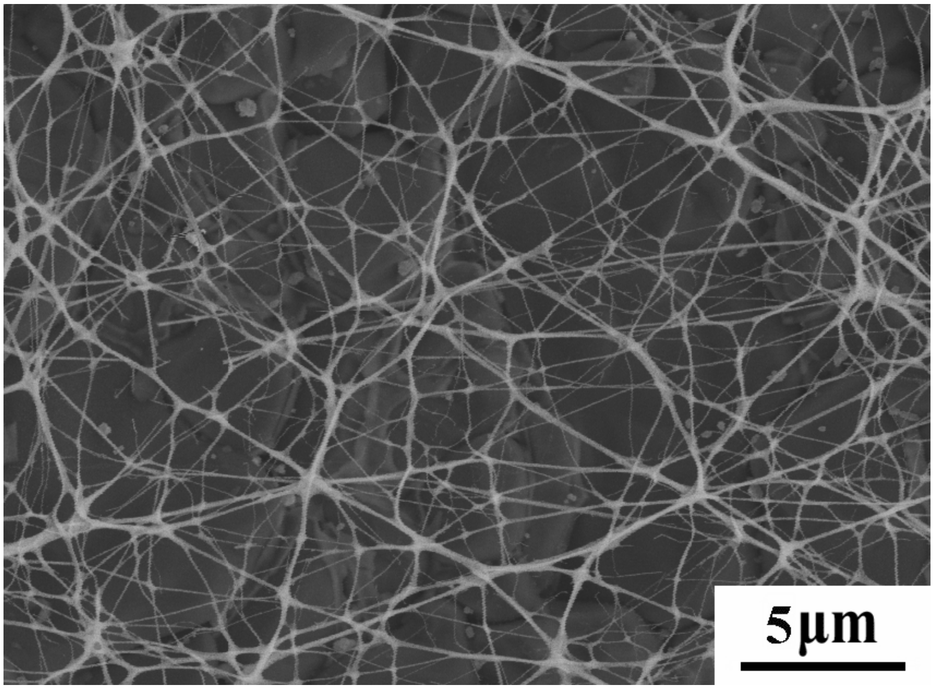

Figure 2.13. WO_3 ceramic nanofibers deposited on Al_2O_3 substrate.

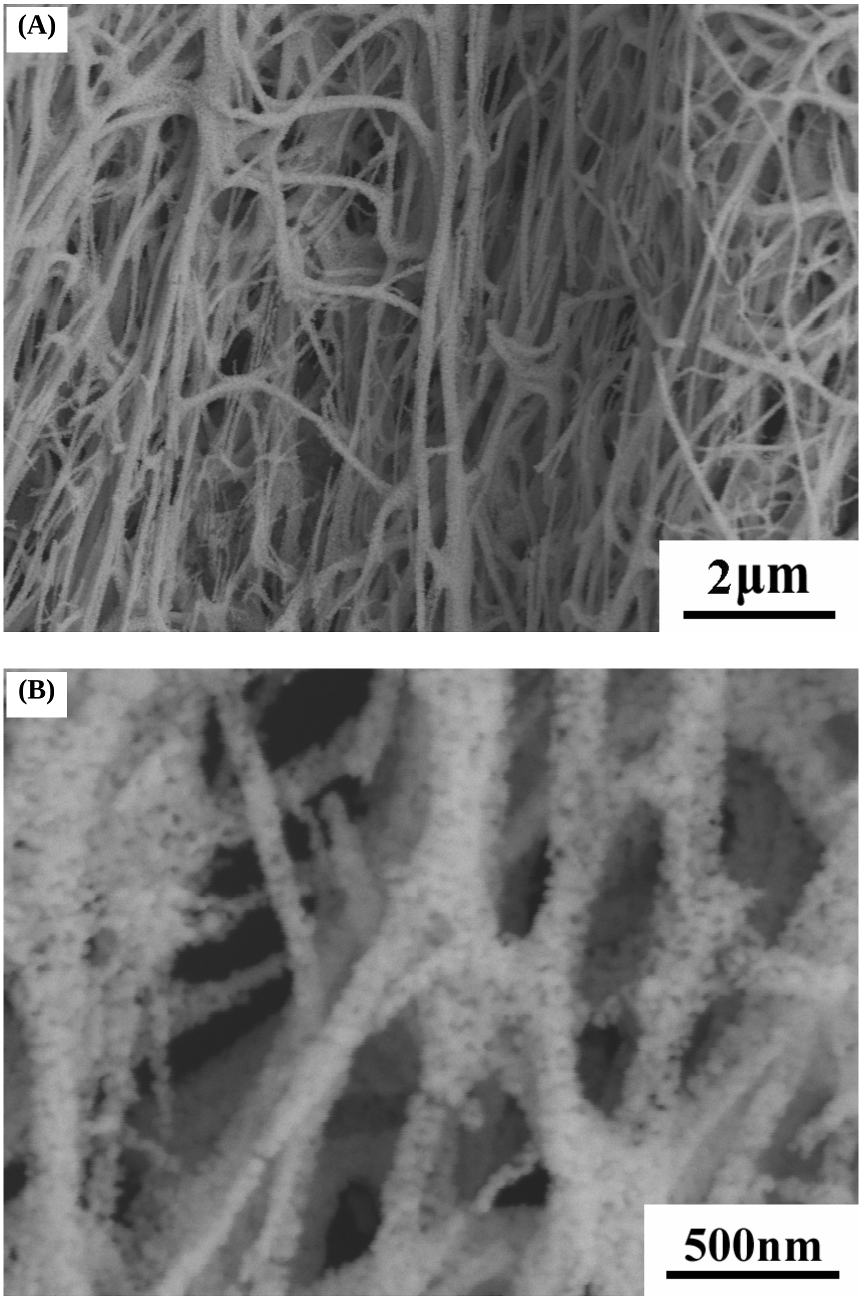

Figure 2.14. WO_3 ceramic fibers obtained after extended deposition time: (A) ×20K (B) ×100K.

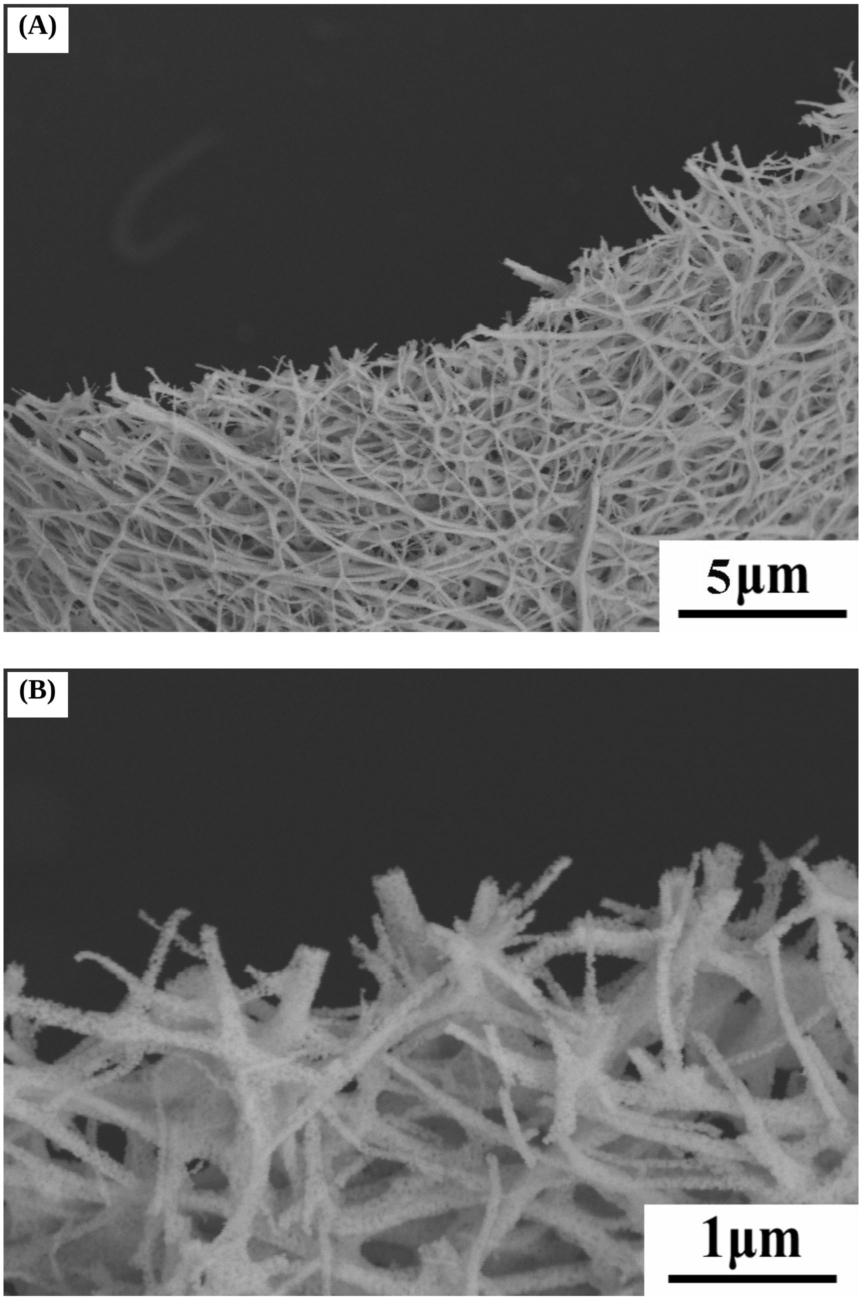

Figure 2.15. Edge area of the mats composed of WO_3 ceramic fibers: (A) ×15K (B) ×50K.

(A)

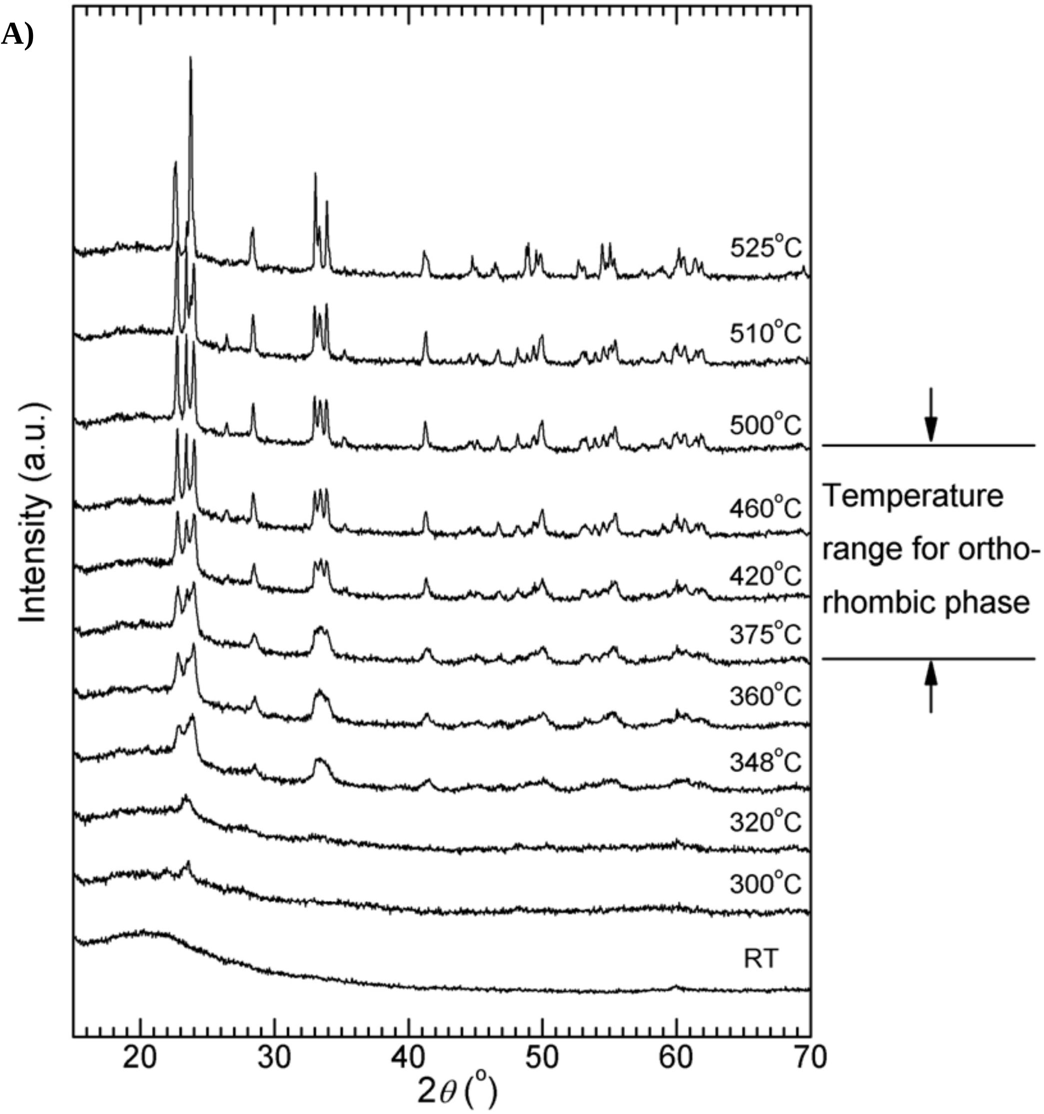

Figure 2.16. *In situ* x-ray diffraction of PVAc/WO_3 nano-composite at different temperatures: (A) an overview of the continuous phase changes; (B) index of representative diffraction peaks from (A).

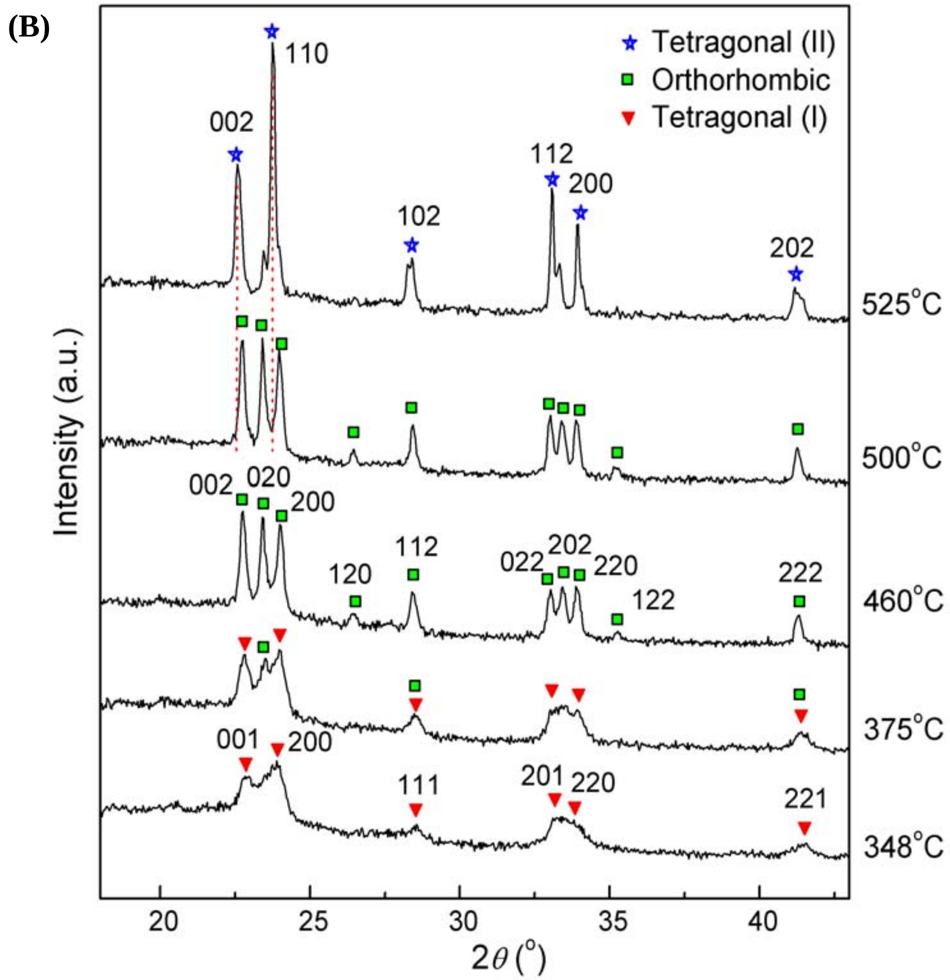

Figure 2.16. (Continued) *In situ* x-ray diffraction of PVAc/WO_3 nano-composite at different temperatures: (A) an overview of the continuous phase changes; (B) index of representative diffraction peaks from (A).

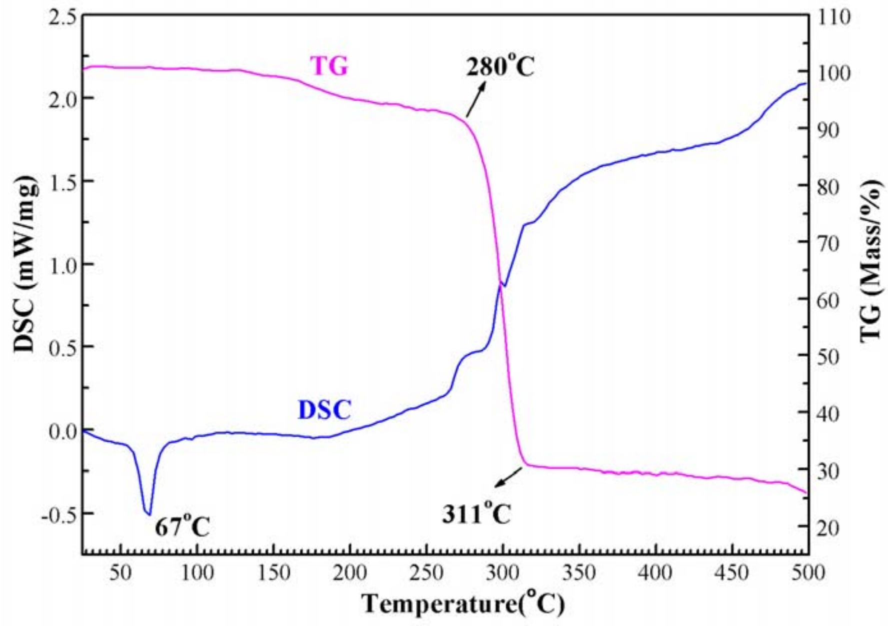

Figure 2.17. Thermal analysis of the PVAc/WO_3Fibers.

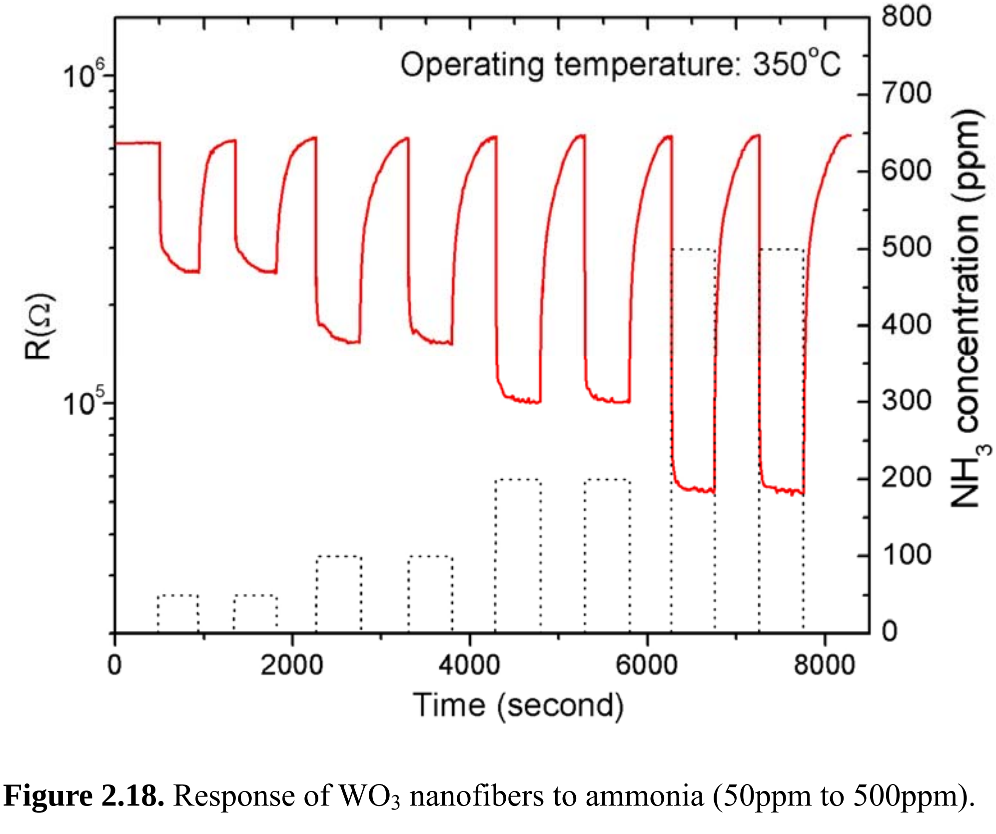

Figure 2.18. Response of WO_3 nanofibers to ammonia (50ppm to 500ppm).

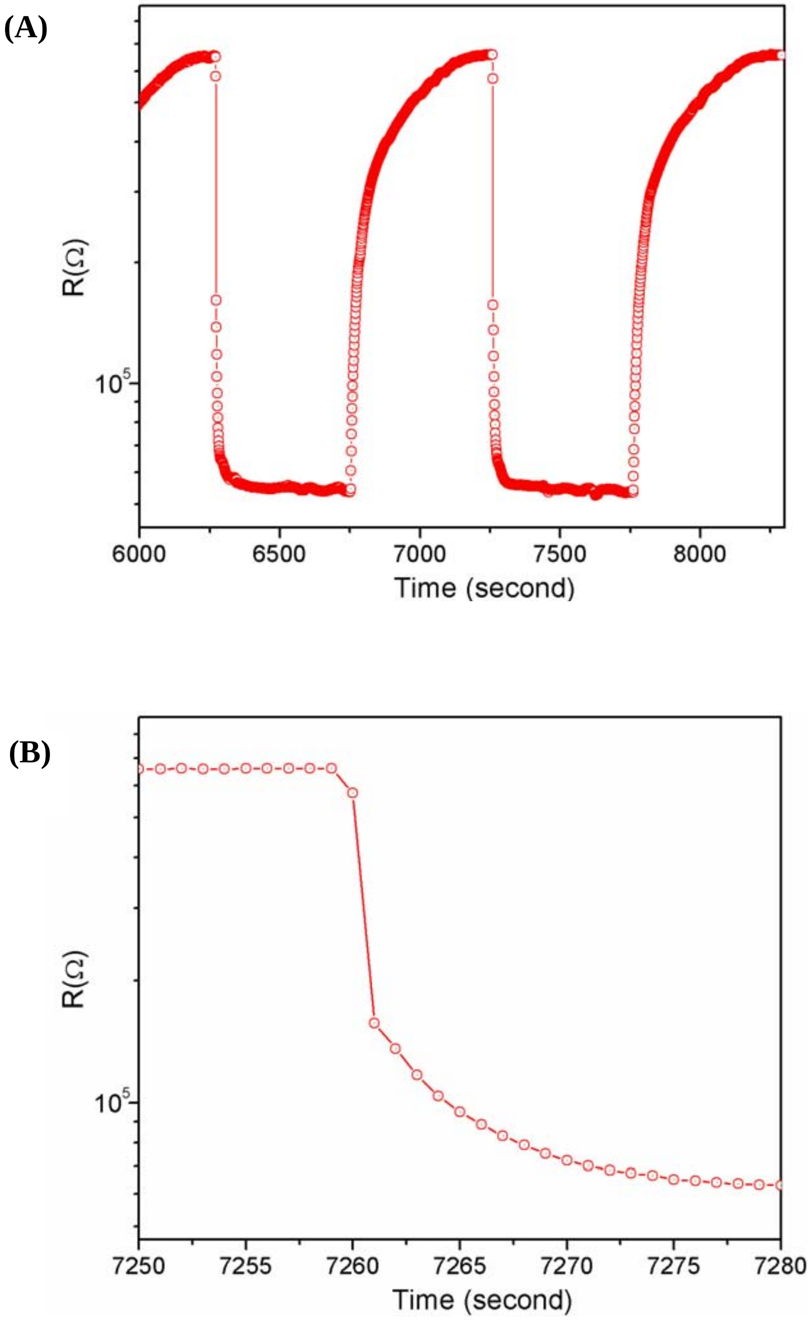

Figure 2.19. Enlarged parts from Figure 2.18: (A) 6000 to 8300 sec; (B) 7250 to 7280 sec.

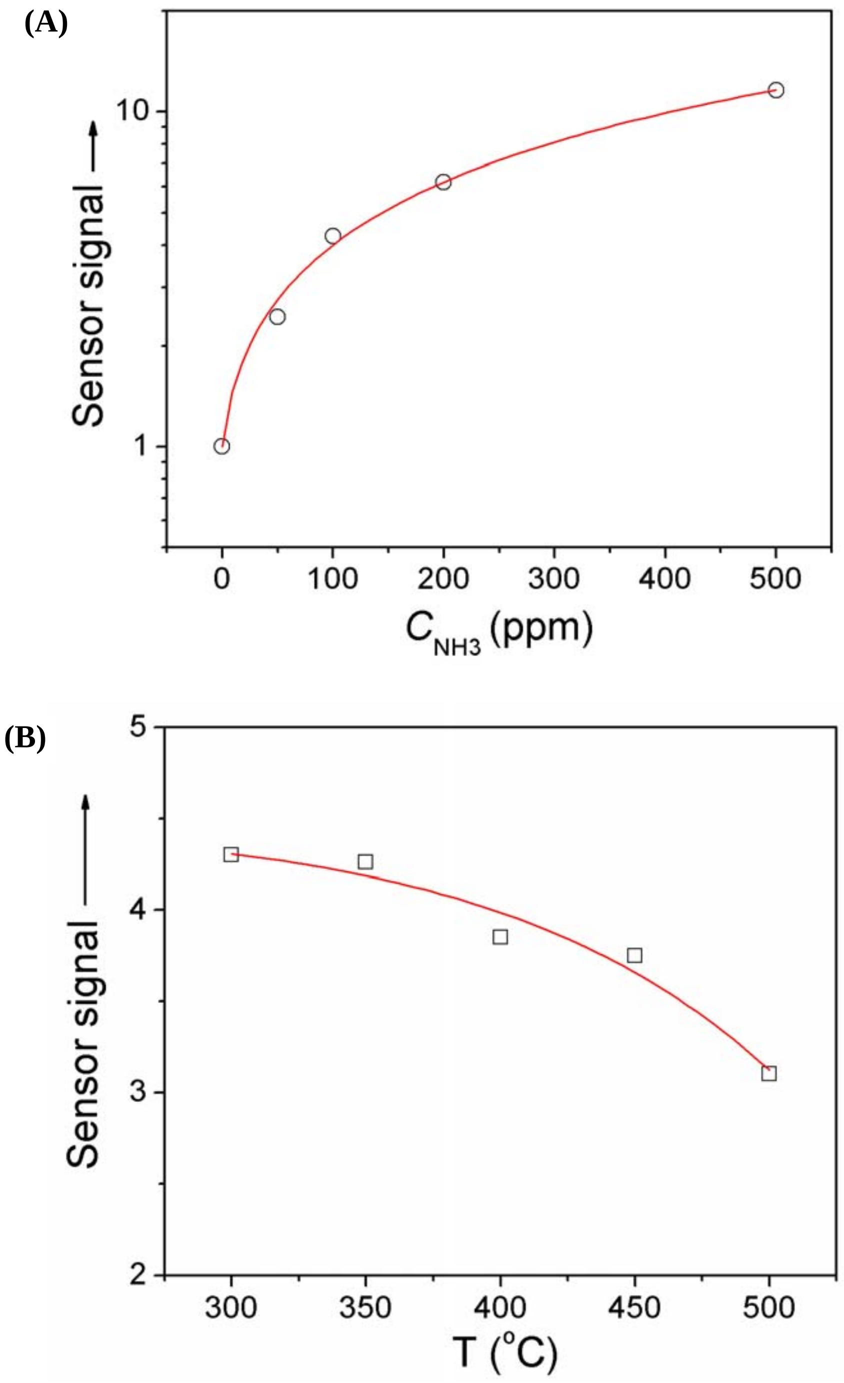

Figure 2.20. (A) Dependence of WO_3 nanofibers sensor signal (S= R_g/R_a) on NH_3 concentrations (C_{NH3}) at 350°C; (B) Dependence of the sensor signal on the operating temperature (based on 100ppm NH_3).

CHAPTER 3

Synthesis of Molybdenum Oxide Nanoplatelets and Nanobelts from the Hybrid Nanocomposites

3.1 Introduction

Nanostructured metal oxides with reduced dimensionality (nanotubes[1, 2], nanowires[3, 4], nanorods[5, 6] and nanobelts[7, 8]) and their applications have been attracting considerable attention. Characterized by their high aspect ratio, nearly perfect crystallinity, structural anisotropy, and small tip radii of curvature, nano-structured oxides are expected to have remarkable optical, electrical, magnetic and ionic transport properties[7, 9-11]. Therefore, fabrication of crystalline metal oxides with lowered dimensionality can often lead to innovative properties and applications. However, it is still a challenge to explore new approaches to tailor the dimensionality and geometry of the oxides with high crystallinity and purity.

As a wide band gap n-type semiconductor, molybdenum oxide (MoO_3) is one of the most intriguing transition metal oxides[12]. It has been widely used in industry as photochromic, electrochromic devices[13, 14], gas sensors[15], and catalysts[16]. In addition, it has been found to be a good precursor for the synthesis of many other important compounds such as MoS2[17, 18], MoSe[19] and Mo[20]. Of the same interest is the peculiar layered structure of α-MoO_3 [21, 22], the most common form of crystalline molybdenum oxides, which offers rich intercalation chemistry. Efforts have been devoted to the preparation of ordered hierarchical arrangement of organic-inorganic composites with layered α-MoO_3 as the host material [23-25]. Conversion of crystalline MoO_3 powder to nanofibers and nanobelts by the hydrothermal method and subsequent thermal treatment have also been realized [26]. To our best knowledge, there is still no report on the morphological organization of molybdenum oxide synthesized directly from its amorphous state with a high purity.

Sol-gel chemistry is widely used to synthesize a variety of nanostructured oxides based on the polymerization of molecular precursors via wet chemical methods [27]. The hydrolysis reaction of appropriate alkoxides often results in the formation of oxides with amorphous or metastable phases, which are not produced by other synthesis routes. In addition, the mild chemical conditions allowed by sol-gel process provide a versatile access to form hybrid organic-inorganic nanocomposites. The degree of interpenetration of the organic and inorganic components can be adjusted from the sub micro range down to the nanometer scale [28].

Herein, we report on a simple method that has successfully realized the shape-controlled growth of crystalline molybdenum oxide. Large scale α-MoO_3 nanoplatelets have been yielded without the use of any catalyst. This method exploits the combination of surfactant/inorganic self-assembly process and host/guest intercalation chemistry to obtain anisotropic crystallization of the molybdenum oxide directly from its amorphous gel. A model has been proposed to explain the formation mechanism of the 2D MoO_3 nanoplatelets. This method is effective, easily controllable and may be applied widely for the production of other 2-D nanostructures.

3.2 Experimental

The molybdenum oxide gel was made by using molybdenum isopropoxide ($Mo(OC_3H_7)_5$, Chemat) as precursor, which was dissolved into 1-butanol to form 0.2M solution. After mechanically agitating for 5 min, the solution was ultrasonicated for 2 hrs, and then aged in a closed container for 24 hrs. A clear blue gel was obtained after aging. The typical blue color indicated the coexistence of different Mo oxidation states, whose relative amount and evolution at elevated temperatures depend on the material typology [29]. On the other hand, poly(ethylene oxide) (PEO, Mw = 400,000, Aldrich) was dissolved in ethanol by continuously stirring at 50°C to form a viscous solution with a concentration of 0.05g/ml. This solution was mixed with the molybdenum oxide sol in the volume ratio of 1:1. Nanocomposite film was formed on Si substrate by dip-coating method. The film was left in air for 3 days. The same dip-coating process was repeated 3 times. A fully hydrolyzed film was obtained. Then the composite film was calcined up to 500°C at a heating rate of 2°C/min, in order to obtain crystallized molybdenum oxide and remove the polymer.

The same procedure has been employed to produce PVP/ $Mo(iPr)_5$ nanocomposites in order to confirm the effects from different polymer surfactants. In this experiment, we used Poly(vinyl pyrrolidone) (PVP, Mw = 1300000, Aldrich). The relative ratio of different components was adjusted to be 0.15mmol PVP + 1ml ethanol + 0.5ml $Mo(iPr)_5$ gel. The composite solution was made ready for dip-coating as well as electrospinning.

Solutions prepared above have all been used for electrospinning. A voltage of 10kV was used. And the collecting distance was decided to be 11cm. Flow rate of the solution was varied from 10 to 50μl/min, in order to study its effect on the fiber's configuration.

Al foils were used as collectors. The as-spun sample experienced a calcination process at the rate of 2^{o}C/min till 500^{o}C. Then the sample was held at 500^{o}C for 3 hours, followed by cooling down in air to room temperature. By calcining the nanocomposites with confined dimensionalities, we are trying to control the consequent growth of molybdenum oxide nanostructures.

Netzsch Simultaneous Thermal Analyzer has been used for DSC and TG analysis to study the heating process. The sample morphologies were characterized using a field emission scanning electron microscope (FESEM) (LEO 1550) with an accelerating voltage of 15 kV. The elements composing the nanofibers were analyzed using Energy Dispersive X-ray Spectroscopy (EDX). High resolution Transmission Electron Microscopy (HRTEM) images of the MoO_3 nanoplatelet were taken with JEOL JEM 3000F with an accelerating voltage of 300kV. The x-ray diffraction measurements were conducted at Beamline X18A of National Synchrotron Light Source (NSLS) at Brookhaven National Lab. The *in situ* x-ray diffraction data were recorded using a position sensitive detector (PSD) while heating the sample within the x-ray beam from 25^{o}C to 525^{o}C. This *in situ* synchrotron XRD set-up has been described in detail in Chapter 2.

3.3 Results and Discussion

3.3.1 Morphology of the molybdenum oxide nanostructure

FESEM images showed that as-prepared products after calcination were mainly composed of nanoplatelets with regular shape, as illustrated in Figure 3.1(A) and (B). Most nanoplatelets have nearly rectangular shape about 1-2 μm across. The thicknesses of the nanoplatelets range from tens of nanometers to around 100 nanometers. The energy dispersive spectrum for samples deposited on a Si wafer confirmed that the nanoplatelets consisted only of oxygen and molybdenum (see Figure 3.1(C)). The x-ray diffraction pattern of this sample provided clear evidence of the crystalline structure (see Figure 3.1(D)). The diffraction peaks could be readily indexed to the orthorhombic phase of MoO_3 (*Pbnm*, JCPDS# 05-0508) with the lattice parameters: a= 3.962 Å, b= 13.858 Å, c= 3.697 Å. For a sample deposited on Si wafer, much stronger diffraction intensities have been found from the (0k0) peaks, suggesting the anisotropic growth of the nanoplatelets. The preferential orientation in the [010] direction is due to their planar geometry.

Figure 3.2 (A) presents a typical TEM image for a single MoO_3 nanoplatelet. The nanoplatelet showed a uniform contrast, which is a general feature of all individual nanoplatelets. The selected area electron diffraction (SAED) pattern of the sample was recorded perpendicular to the planar facet (see Figure 3.2(B) inset). The pattern agreed well with the [010] zone axis diffraction of the orthorhombic MoO_3, as reported in the literatures [11, 30]. We employed SAED on different parts of the sample. The same SAED patterns were observed, implying that the nanoplatelet is single crystalline. High resolution TEM images of the sample showed two sets of parallel fringes with a spacing of 1.98 Å and 1.85 Å, corresponding to (200) and (002) planes respectively (see Figure 3.2 (B)). HRTEM indicated a high degree of crystallinity of the sample, while there was still some disorder, which might be induced by the existence of oxygen vacancies.

3.3.2 Dynamic structure transformation study by *in situ* XRD

In order to understand the dynamic structure transformation of the MoO_3 nanoplatelets from its nanocomposites, *in situ* XRD was carried out by using synchrotron x-ray as the incidence beam. A continuous phase transformation has been observed. Typical diffraction patterns at specific temperatures have been shown in Figure 3.3. The XRD pattern of the nanocomposites was recorded at 25^oC. Two broad peaks near 19^o and 23^o came from characteristic diffraction of semi-crystalline PEO. As temperature increased above the glass transition temperature of PEO (65^oC), no diffraction peak was observed, implying an amorphous characteristic of the hydrolysis product from the sol-gel precursor. Three broad peaks occurred at 270^oC. They could be indexed to monoclinic MoO_2 (*P21/c*, JCPDS# 78-1072). According to the FWHM of the peaks, the crystalline size was calculated to be around 10nm. An obvious phase transformation from monoclinic MoO_2 to orthorhombic MoO_3 started from 300^oC. A mixture of two phases was found from the *in situ* XRD pattern. Some weak peaks which could not be indexed were believed to be from the intermediate compounds during the transition. A pure orthorhombic phase was obtained at 430^oC. This phase was stable up to 500^oC, indexed to the same α-MoO_3 structure (*Pbnm*, JCPDS#05-0508) as in Figure 3.1(D). Preferential diffraction disappeared in the *in situ* XRD pattern due to the different geometry of the sample while collecting the diffraction data.

3.3.3 Thermal analysis by DSC/TG

Thermal analysis of the nanocomposites also provided useful information to understand the kinetic structure evolution process. In Figure 3.4, the differential scanning calorimetry (DSC) curve showed two decomposition peaks at 290°C and 460°C respectively, corresponding to two significant mass losses, which are significant indications of the polymer decomposition. The two-step decomposition of PEO is in agreement with the results of Nazar[24], who explained that the two processes might correspond to aerobic oxidation and oxidation by MoO_3 lattice oxygen. In another word, PEO, intercalated between two layered MoO_3 crystallite, may have a higher decomposition temperature, which resulted in the second strong exothermal peak at 460°C.

3.3.4 Proposed growth mechanism of MoO_3 nanoplatelets

Based on the *in situ* XRD results and thermal analysis of the nanocomposites, a model has been proposed to explain the formation mechanism of the crystalline MoO_3 nanoplatelets. It is well known that α-MoO_3 has vertex-sharing chains of distorted MoO_6 octahedron, which share edges with other similar chains to form layers (see Figure 3.5(A)). These two-dimensional sheets are weakly held together by van der Waals forces, so they can be readily propped open by intercalation species. Crystal growth in the [010] direction is more like the assembling of the layer structure. We suggest that the crystallization of molybdenum oxide from its polymer nanocomposites started from the formation of tiny MoO_2 crystallites, which were distributed uniformly among the polymer chains. As T increased above 300°C, MoO_2 transformed to MoO_3

layer-structured crystallites immediately, which were still surrounded by polymer chains. The in-plane crystal growth of MoO_3 involved the formation of Mo-O bonds with a large energy release during this process. Meanwhile, inter-plane region was intercalated effectively by the polymer surfactant. Since crystal growth in the inter-plane direction has to overcome the intercalation effect of the polymer, it is not energetically preferred. At 500^{o}C, PEO decomposed completely, and crystalline orthorhombic MoO_3 formed with an anisotropic geometry. The schematic of this process is shown in Figure 3.5(B).

3.3.5 Effective factors for the morphology controlled growth

Several factors can be expected to affect the growth of the MoO_3 nanoplatlets from the hybrid nanocomposites, such as the sol-gel concentration, heating rate and temperature, which can affect the sintered products from sol-gel process. Other factors, such as type and concentration of the polymer, may also be the effective in the calcination process. In this research, we are more interested in the effect from the polymer surfactants, which is a key factor for the generalization of our proposed anisotropic growth mechanism.

With samples prepared in the same procedure, we have demonstrated that other polymer surfactants, such as poly(vinyl pyrrolidone) (PVP), can play the same role as PEO. As shown in Figure 3.6, similar MoO_3 nanoplatelets have been produced without changing any other conditions. The only difference is that the crystalline size of each nanoplatelet is larger. This may be the results of a more ordered interaction between the different polymer chains and the molybdenum oxide sol-gel. XRD of the nanoplatelets deposited on Si wafer was indexed to the same orthorhombic phase (*Pbnm*, JCPDS#

05-0508). It also showed strong preferential diffraction from the (0 k 0) peaks (see Figure 3.7).

3.3.6 Electrospinning PEO/Mo(iPr)$_5$ nanocomposite fibers

SEM images of the as-electrospun samples are shown in Figure 3.8. It can be seen that submicron composite fibers can be obtained. Fiber diameters range from 300 nm up to 600 nm. Fibers are not uniform along the longitude direction. The small speckles are proposed to be the hydrolysis product of the sol-gel precursor. They distribute non-uniformly in the polymer template of fibers. The dependence of fiber diameters on the flow rates at constant working voltage for molybdenum oxide-PEO composite fibers has been plotted in Figure 3.9. It can be concluded that a faster feeding rate often results in thicker fibers. But during the experiment, when the flow rate is too high or too low, the jets became unstable. Fibers with non-uniform diameters will be produced (for example, see Figure 3.8 (A) for the SEM image of fibers obtained at 10μl/min).

The nanocomposite fibers experienced the calcination process described in the experimental session. No continuous ceramic fibers have ever been obtained like the pure tungsten oxide ceramic nanofibers as we see in Chapter 2. Instead, we observed closely connected short fibers, or more accurately, nanobelts with the diameters of a few hundred nanometers and an average length of about several microns have formed. Notably, all these individual crystallites look like single crystals without any grain boundaries, as presented in Figure 3.10. Crystallinity and structure of the nanobelts have been determined by TEM and XRD respectively, as demonstrated in Figure 3.11. It is easy to find that the as-prepared MoO_3 nanobelts have the same preferential growth orientation as the MoO_3 nanoplatelets, which we made directly from the nanocomposites. Nothing else changes except the elongated shape of the nanobelts. Based on the model we proposed in section 3.3.4, and with the characteristics of electrospun fibers in mind, we proposed the formation mechanism of the MoO_3 nanobelts from the Polymer/$Mo(iPr)_5$ nanocomposite fibers, as shown in Figure 3.12. The basic idea for this synthesis mechanism is the combination of the confinement effects of the polymer templates and the preferred crystallization process of layered MoO_3 from its sol-gel/polymer nanocomposites. The result from this combined effect is the directed growth of the MoO_3 nanoplatelets along the direction of the polymer nanofiber templates. Lateral growth of the nanobelts is confined by the diameters of the composite nanofibers. In terms of the distribution of MoO_3 precursors inside the polymer nanofibers, the length of MoO_3 nanobelts varies.

3.4 Conclusions

In summary, we have successfully synthesized MoO_3 nanoplatelets from the molybdenum oxide sol-gel and polymer hybrid nanocomposites. All the nanoplatelets showed a lowered dimensionality in the [010] direction. Detailed TEM analysis revealed that the nanoplatelets were single crystal of flat face with good crystallinity. *In situ* XRD illustrated the dynamic structural formation of the orthorhombic MoO_3 nanoplatelets. The function of polymer as the surfactant and intercalation material during the crystallization of the layer structure of MoO_3 has been discussed, interpreting the preferential growth of the nanoplatelets from the nanocomposites. Combining electrospinning process with this anisotropic growth of MoO_3 layered structure from its nanocomposites, we successfully realized the templated growth of these nanoplatelets, which produced MoO_3 nanobelts due to the confinement effect of the polymer nanofibers. This method may also be applied to the growth of low dimensional structures of other materials with layered structure.

References

1. Tenne, R.; Margulis, L.; Genut, M.; Hodes, G., Polyhedral and Cylindrical Structures of Tungsten Disulfide. *Nature* **1992,** 360, (6403), 444-446.

2. Rao, C. N. R.; Govindaraj, A.; Deepak, F. L.; Gunari, N. A.; Nath, M., Surfactant-assisted synthesis of semiconductor nanotubes and nanowires. *Applied Physics Letters* **2001,** 78, (13), 1853-1855.

3. Morales, A. M.; Lieber, C. M., A laser ablation method for the synthesis of crystalline semiconductor nanowires. *Science* **1998,** 279, (5348), 208-211.

4. Duan, X. F.; Lieber, C. M., General synthesis of compound semiconductor nanowires. *Advanced Materials* **2000,** 12, (4), 298-302.

5. Yu, Y. Y.; Chang, S. S.; Lee, C. L.; Wang, C. R. C., Gold nanorods: Electrochemical synthesis and optical properties. *Journal of Physical Chemistry B* **1997,** 101, (34), 6661-6664.

6. Manna, L.; Scher, E. C.; Alivisatos, A. P., Synthesis of soluble and processable rod-, arrow-, teardrop-, and tetrapod-shaped CdSe nanocrystals. *Journal of the American Chemical Society* **2000,** 122, (51), 12700-12706.

7. Pan, Z. W.; Dai, Z. R.; Wang, Z. L., Nanobelts of semiconducting oxides. *Science* **2001,** 291, (5510), 1947-1949.

8. Arnold, M. S.; Avouris, P.; Pan, Z. W.; Wang, Z. L., Field-effect transistors based on single semiconducting oxide nanobelts. *Journal of Physical Chemistry B* **2003,** 107, (3), 659-663.

9. Hu, J. T.; Odom, T. W.; Lieber, C. M., Chemistry and physics in one dimension: Synthesis and properties of nanowires and nanotubes. *Accounts of Chemical Research* **1999,** 32, (5), 435-445.

10. Patzke, G. R.; Krumeich, F.; Nesper, R., Oxidic nanotubes and nanorods - Anisotropic modules for a future nanotechnology. *Angewandte Chemie-International Edition* **2002,** 41, (14), 2446-2461.

11. Li, Y. B.; Bando, Y.; Golberg, D.; Kurashima, K., Field emission from MoO3 nanobelts. *Applied Physics Letters* **2002,** 81, (26), 5048-5050.

12. Hussain, Z., Optical and electrochromic properties of heated and annealed MoO3

thin films. *Journal of Materials Research* **2001,** 16, (9), 2695-2708.

13. Yao, J. N.; Hashimoto, K.; Fujishima, A., Photochromism Induced in an Electrolytically Pretreated Moo3 Thin-Film by Visible-Light. *Nature* **1992,** 355, (6361), 624-626.

14. Yang, Y. A.; Cao, Y. W.; Loo, B. H.; Yao, J. N., Microstructures of electrochromic MoO3 thin films colored by injection of different cations. *Journal of Physical Chemistry B* **1998,** 102, (47), 9392-9396.

15. Taurino, A. M.; Forleo, A.; Francioso, L.; Siciliano, P.; Stalder, M.; Nesper, R., Synthesis, electrical characterization, and gas sensing properties of molybdenum oxide nanorods. *Applied Physics Letters* **2006,** 88, (15).

16. Liu, H. F.; Liu, R. S.; Liew, K. Y.; Johnson, R. E.; Lunsford, J. H., Partial Oxidation of Methane by Nitrous-Oxide over Molybdenum on Silica. *Journal of the American Chemical Society* **1984,** 106, (15), 4117-4121.

17. Margulis, L.; Salitra, G.; Tenne, R.; Talianker, M., Nested Fullerene-Like Structures. *Nature* **1993,** 365, (6442), 113-114.

18. Feldman, Y.; Wasserman, E.; Srolovitz, D. J.; Tenne, R., High-Rate, Gas-Phase Growth of MoS_2 Nested Inorganic Fullerenes and Nanotubes. *Science* **1995,** 267, (5195), 222-225.

19. Hershfinkel, M.; Gheber, L. A.; Volterra, V.; Hutchison, J. L.; Margulis, L.; Tenne, R., Nested Polyhedra of Mx(2) (M=W, Mo X=S, Se) Probed by High-Resolution Electron-Microscopy and Scanning-Tunneling-Microscopy. *Journal of the American Chemical Society* **1994,** 116, (5), 1914-1917.

20. Zach, M. P.; Ng, K. H.; Penner, R. M., Molybdenum nanowires by electrodeposition. *Science* **2000,** 290, (5499), 2120-2123.

21. Andersson, G.; Magneli, A., On the Crystal Structure of Molybdenum Trioxide. *Acta Chemica Scandinavica* **1950,** 4, (5), 793-797.

22. McCarron, E. M., Beta-Moo3 - a Metastable Analog of Wo3. *Journal of the Chemical Society-Chemical Communications* **1986**, (4), 336-338.

23. Tagaya, H.; Ara, K.; Kadokawa, J.; Karasu, M.; Chiba, K., Intercalation of Organic-Compounds in the Layered Host Lattice MoO_3. *Journal of Materials Chemistry* **1994,** 4, (4), 551-555.

24. Nazar, L. F.; Wu, H.; Power, W. P., Synthesis and Properties of a New (Peo)(X)[Na(H_2O)]0.25MoO_3 Nanocomposite. *Journal of Materials Chemistry* **1995,** 5, (11), 1985-1993.

25. Hosono, K.; Matsubara, I.; Murayama, N.; Woosuck, S.; Izu, N., Synthesis of polypyrrole/MoO3 hybrid thin films and their volatile organic compound gas-sensing properties. *Chemistry of Materials* **2005,** 17, (2), 349-354.

26. Song, R. Q.; Xu, A. W.; Deng, B.; Fang, Y. P., Novel multilamellar mesostructured molybdenum oxide nanofibers and nanobelts: Synthesis and characterization. *Journal of Physical Chemistry B* **2005,** 109, (48), 22758-22766.

27. Brinker, C. J.; Scherer, G. W., *Sol-Gel Science: The Physics and Chemistry of Sol-Gel Processing*. Academic Press, Inc: San Diego, 1990.

28. Sanchez, C.; Ribot, F., Design of Hybrid Organic-Inorganic Materials Synthesized Via Sol-Gel Chemistry. *New Journal of Chemistry* **1994,** 18, (10), 1007-1047.

29. Epifani, M.; Imperatori, P.; Mirenghi, L.; Schioppa, M.; Siciliano, P., Synthesis and characterization of MoO3 thin films and powders from a molybdenum chloromethoxide. *Chemistry of Materials* **2004,** 16, (25), 5495-5501.

30. Xia, T. A.; Li, Q.; Liu, X. D.; Meng, J. A.; Cao, X. Q., Morphology-controllable synthesis and characterization of single-crystal molybdenum trioxide. *Journal of Physical Chemistry B* **2006,** 110, (5), 2006-2012.

FIGURES:

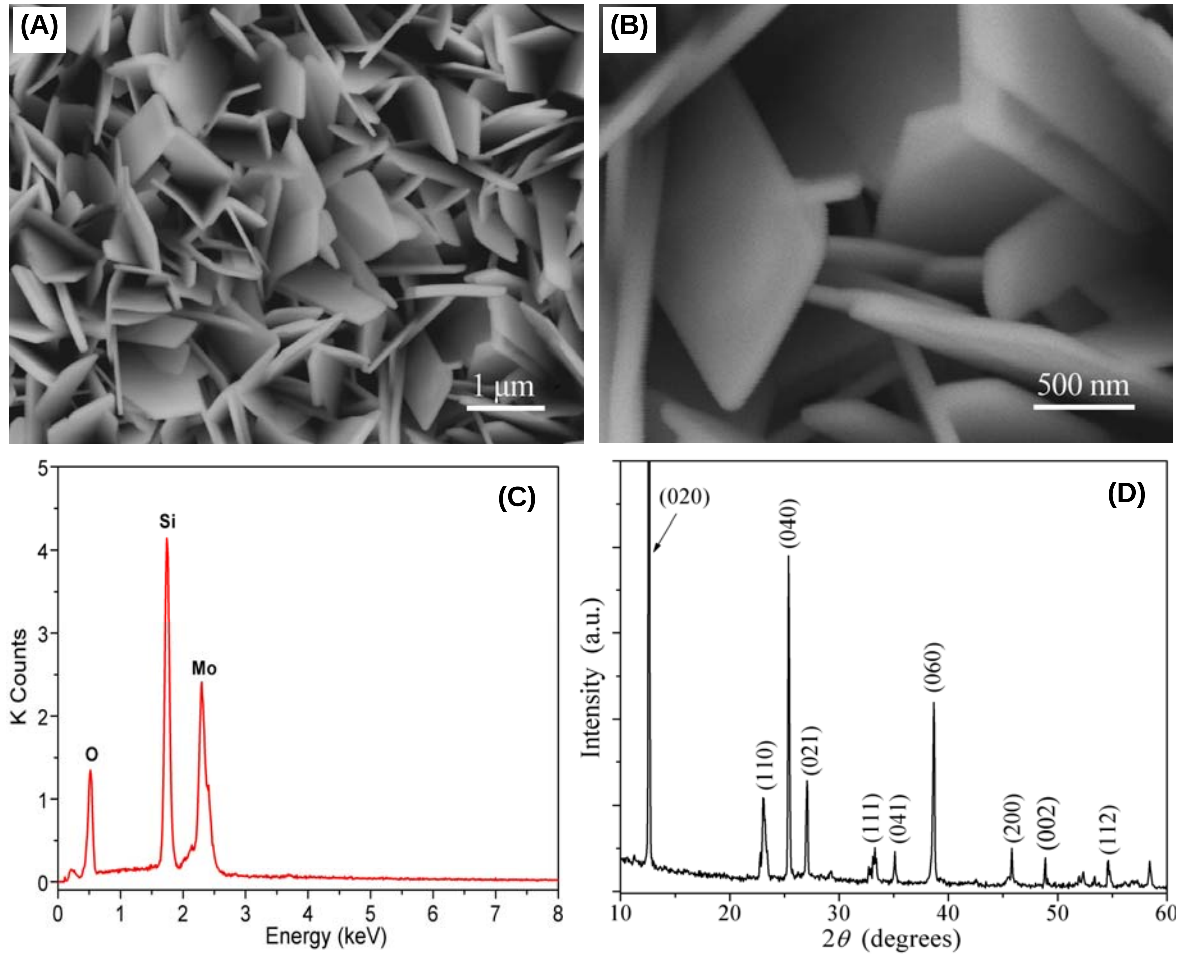

Figure 3.1. SEM images of the MoO_3 nanoplatelets under magnifications of (A)30K and (B)80K; and (C) EDS pattern of the nanoplatelets (Si peak originated from the substrate), (D) XRD of the nanoplatelets sample on Si.

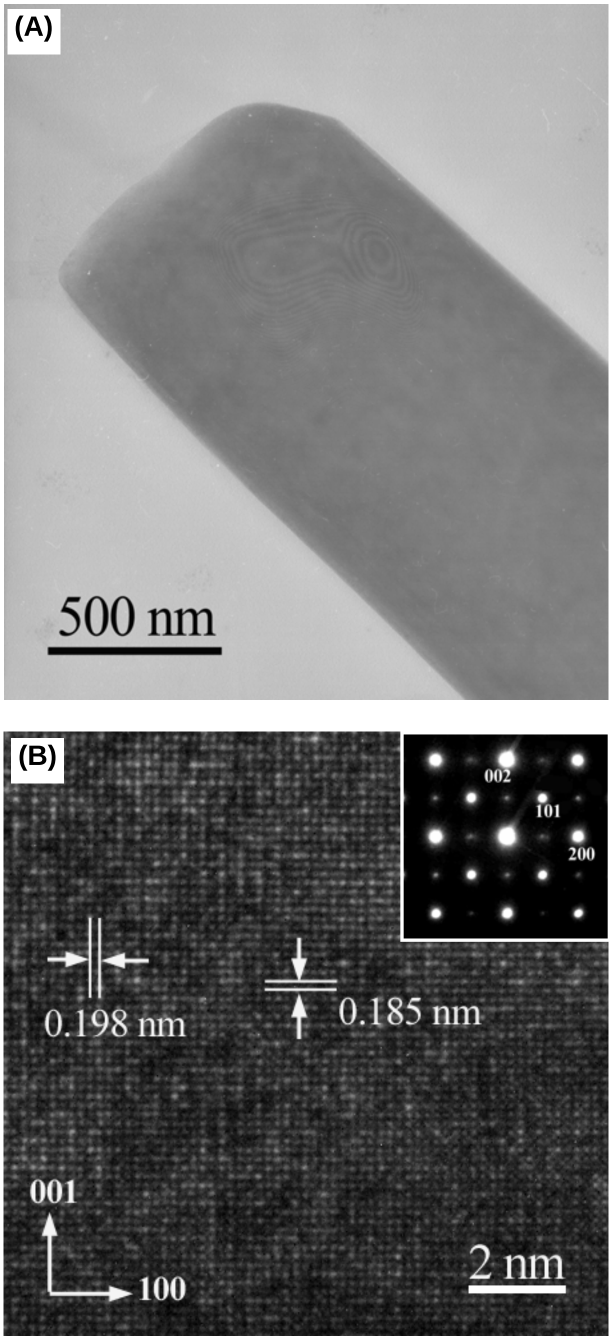

Figure 3.2. (A) TEM image of a single MoO_3 nanoplatelet; (B) High resolution TEM image of the nanoplatelet and the corresponding selected area diffraction pattern (inset).

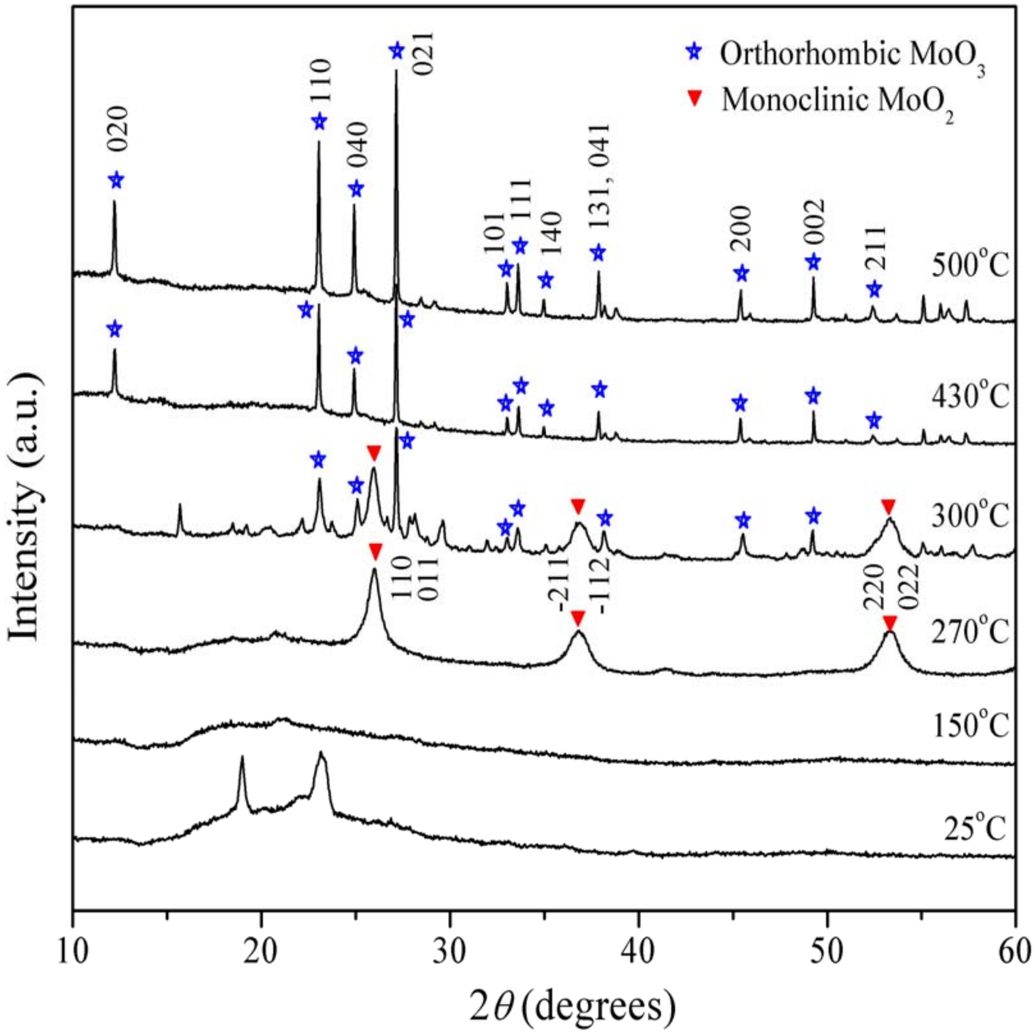

Figure 3.3. Representative *in situ* XRD patterns showing the dynamic structure evolution of the nanoplatelets from the hybrid nanocomposites.

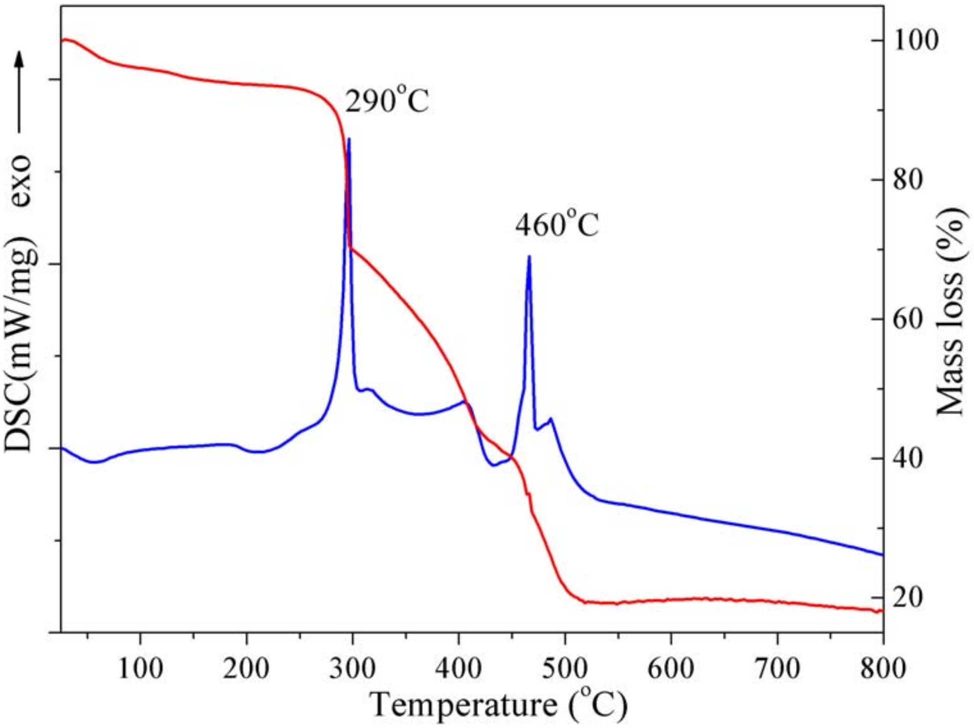

Figure 3.4. DSC/TG analysis of the molybdenum oxide sol-gel and PEO nanocomposites.

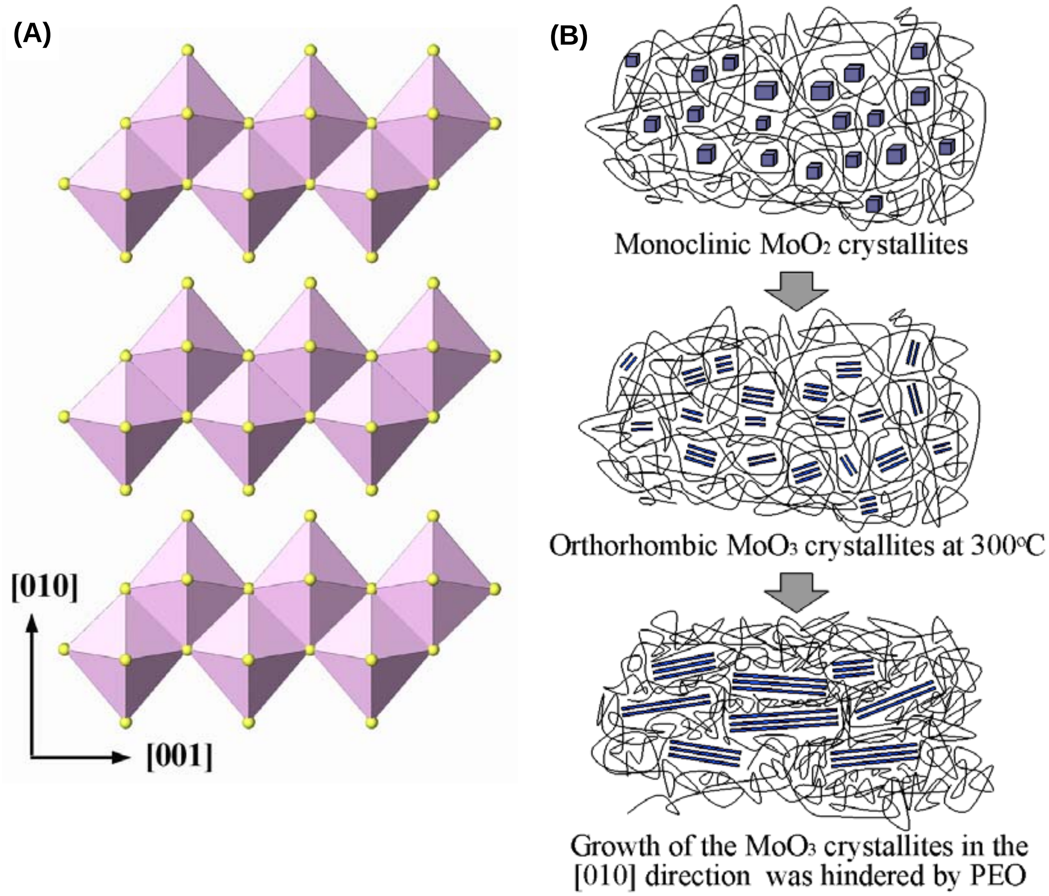

Figure 3.5. (A) Layered structure of α-MoO_3; and (B) proposed crystallization process for the formation of MoO_3 nanoplatelets.

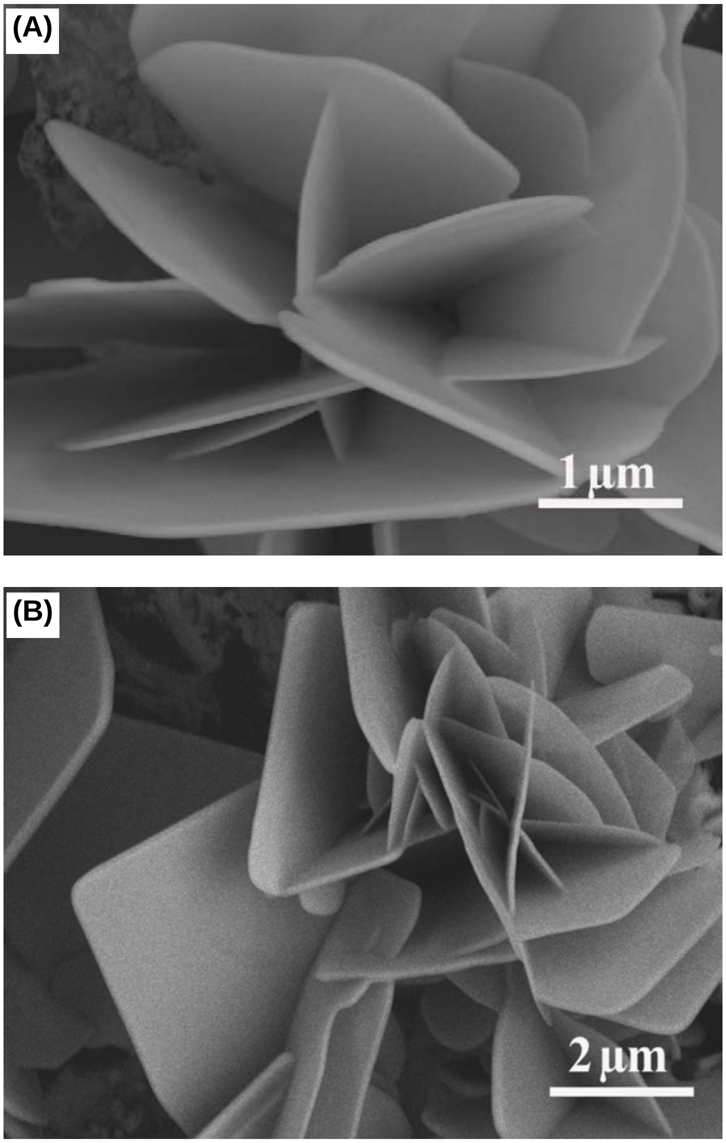

Figure 3.6. SEM images of the MoO_3 nanoplatelets synthesized with PVP as surfactant. Magnifications are (A)×40K and (B)×20K respectively.

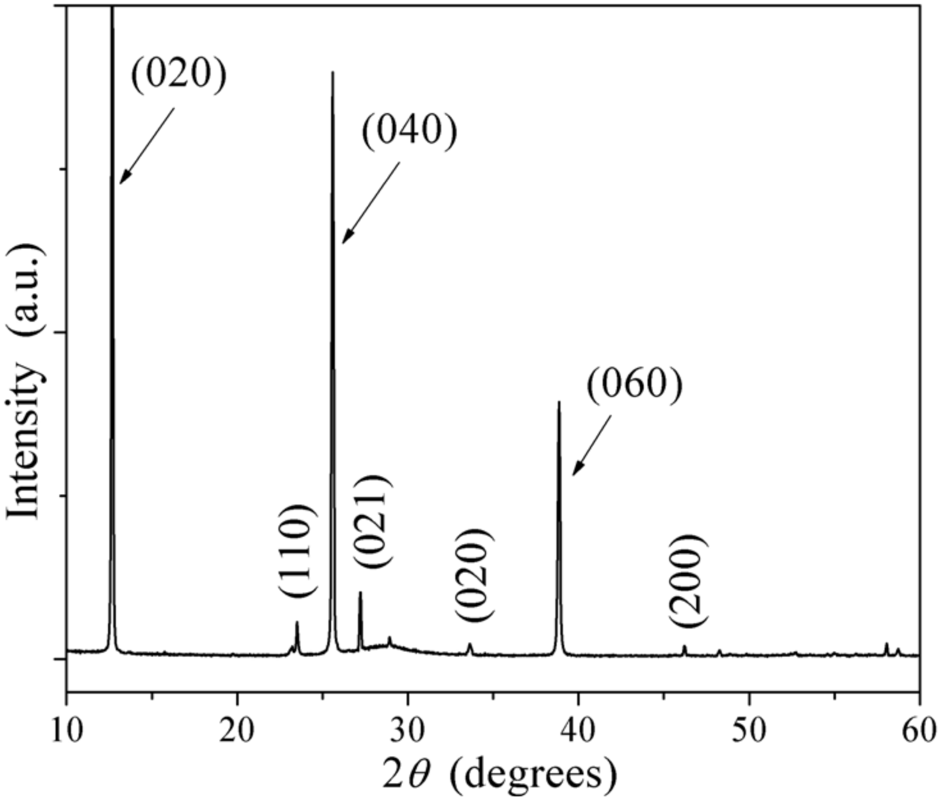

Figure 3.7. XRD of the MoO_3 nanoplatelets sample on Si, showing strong diffraction from (0k0) peaks.

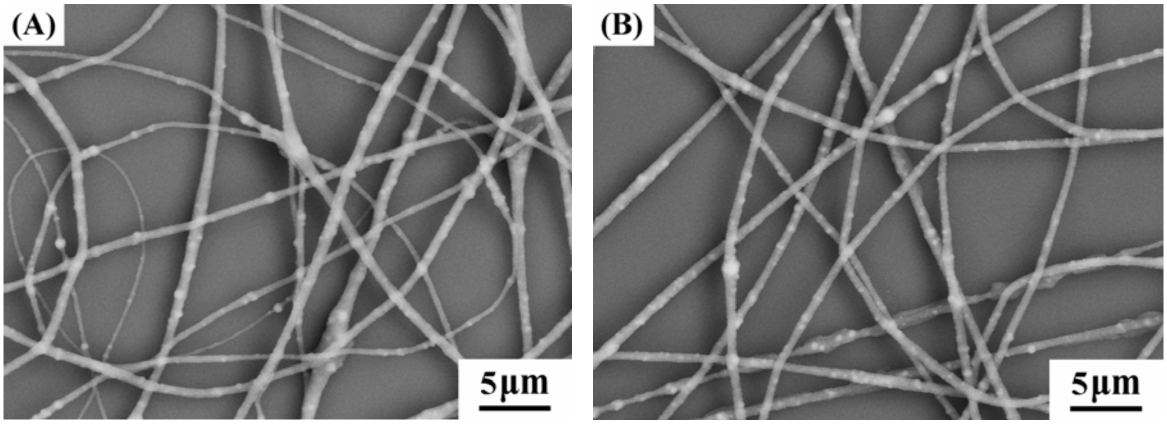

(A) 10µl/min **(B)** 20µl/min

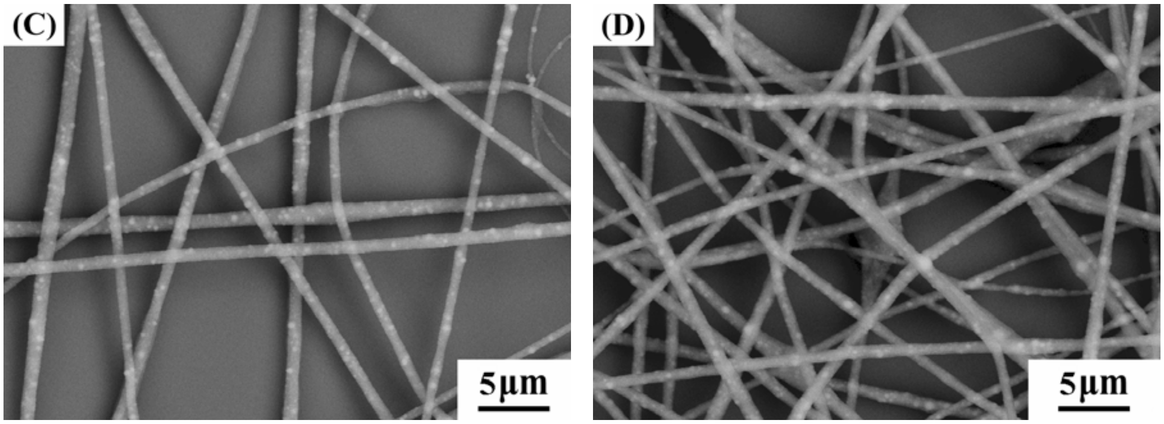

(C) 35µl/min **(D)** 50µl/min

Figure 3.8. SEM images of the as-prepared PEO/molybdenum oxide composite fibers obtained at 10 kV and different flow rates.

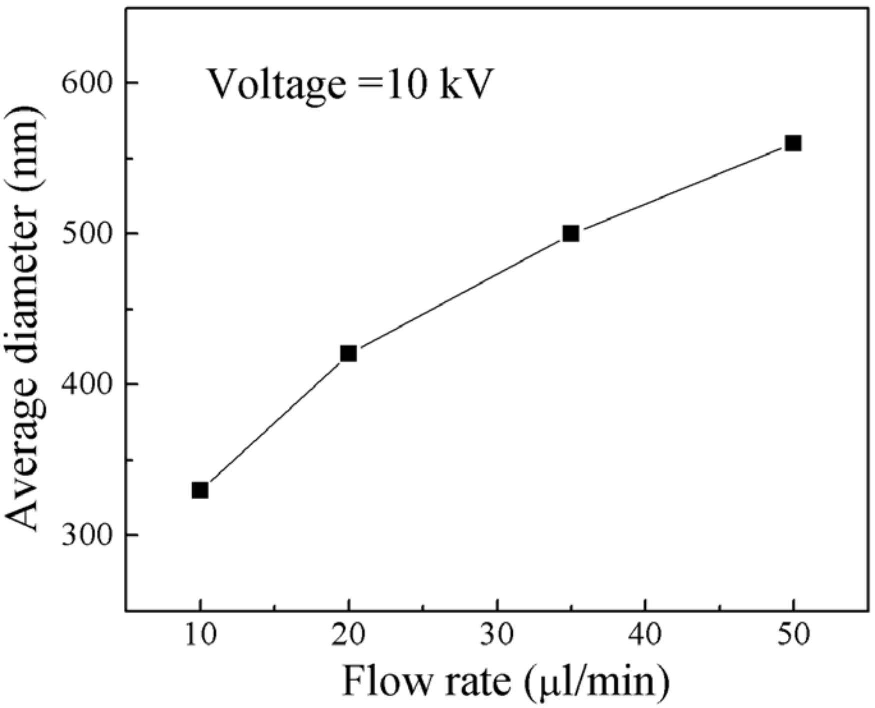

Figure 3.9. The dependence of fiber diameters on the flow rates at constant working voltage for PEO/molybdenum oxide composite fibers.

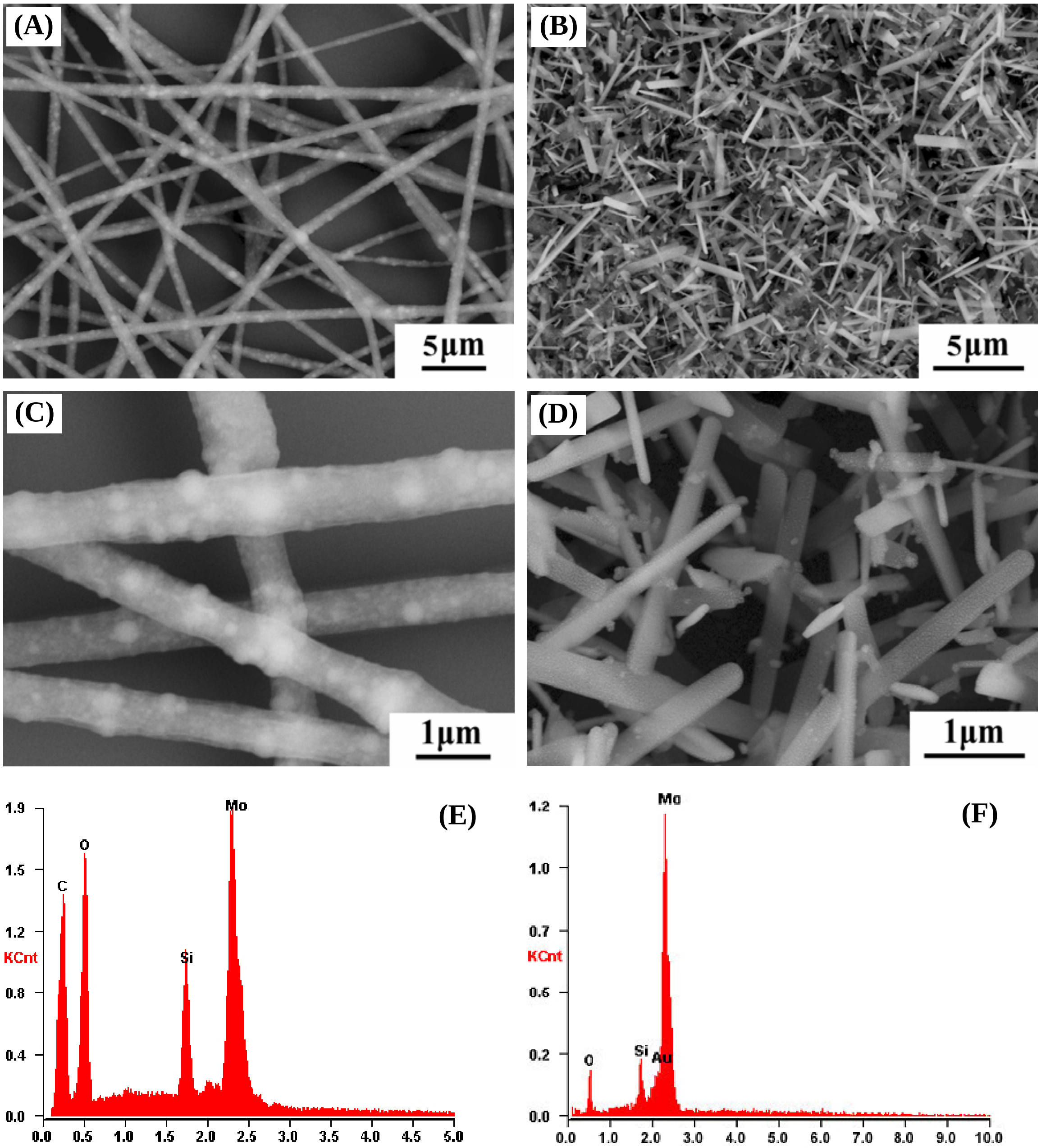

Figure 3.10. SEM images of PEO/Mo(iPr)$_5$ composite nanofiber before calcination (A, C) and after calcinations (B, D), as well as corresponding EDS spectrum after of the nanofibers before (E) and after (F) calcination.

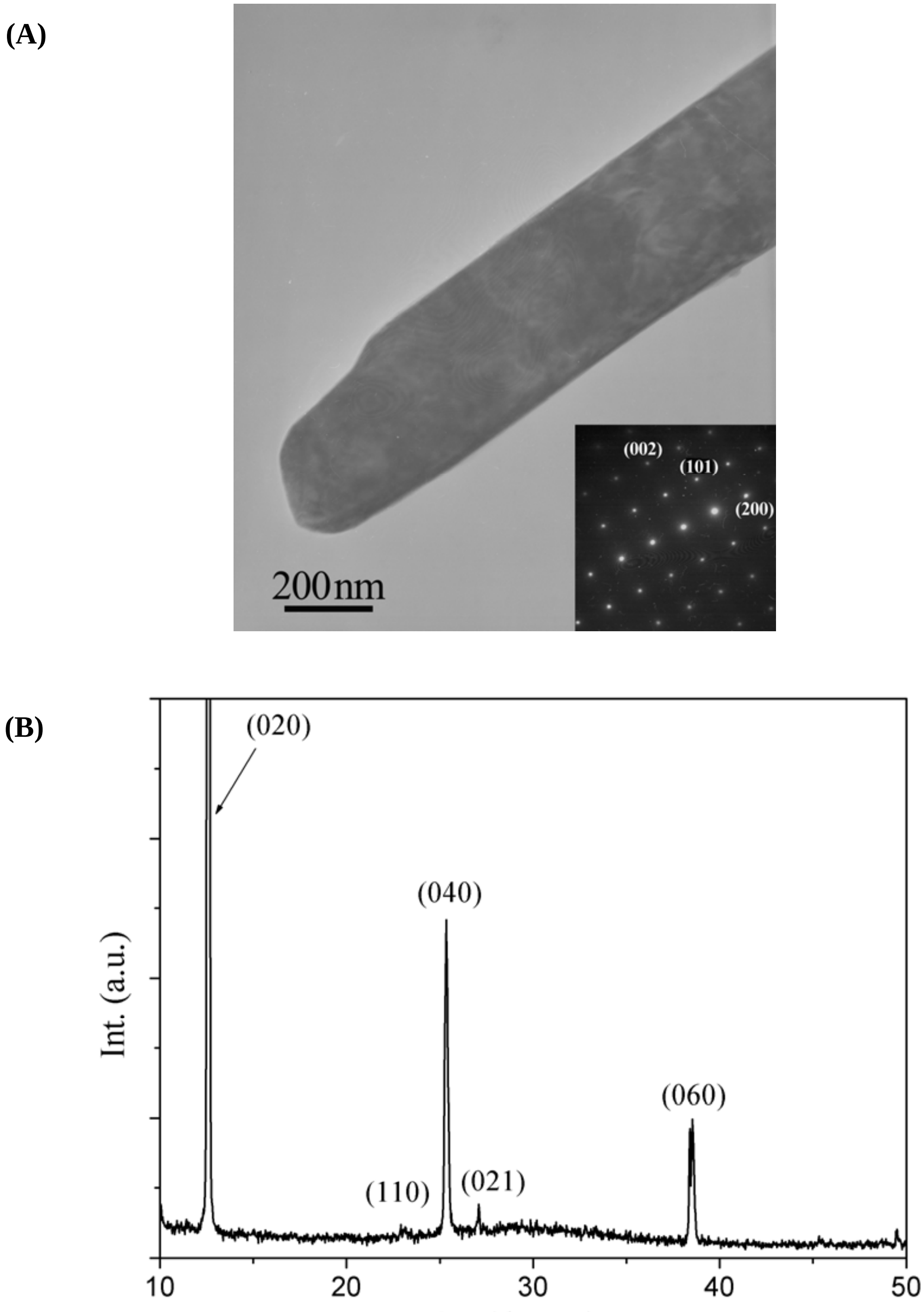

Figure 3.11. (A) TEM image of a single MoO_3 nanobelt; (B) XRD of the MoO_3 nanobelt after calcination, showing strong diffraction from (0k0) peaks.

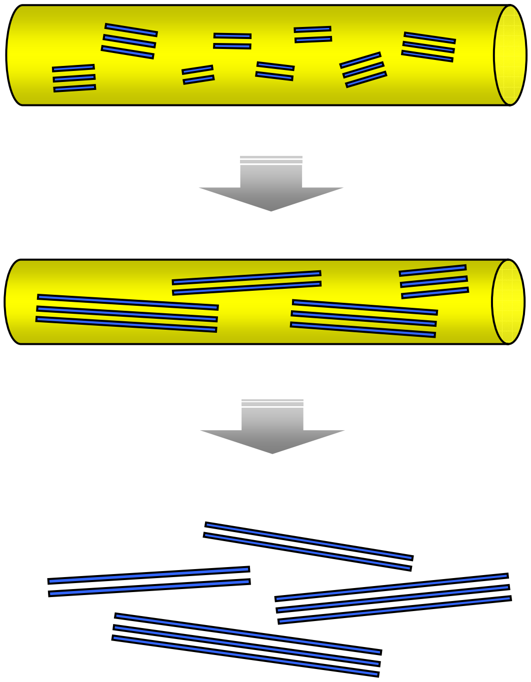

Step 1. Formation of MoO_3 crystallites at low temperatures;

Step 2. Formation of big MoO_3 crystallites with preferred orientation and under the confinement effect from the template of polymer nanofiber;

Step 3. Formation of MoO_3 nanobelts after the removal of polymer template.

Figure 3.12. Proposed mechanism for the confined growth of MoO_3 nanobelts.

CHAPTER 4

Electrospinning Polymer/MWNT Composite Nanofibers

4.1 Introduction

4.1.1 Structure and properties of carbon nanotubes

Since their discovery in 1991 by Iijima and coworkers[1], carbon nanotubes (CNTs) have been investigated intensively by many researchers all over the world. CNTs can be seen as the nearly one-dimensional form of fullerenes. A major feature of the structure of carbon nanotube is the periodically repeated hexagon patterns (honeycomb) forming a graphene sheet. The periodicity arrangement of the hexagons causes each atom to bond to three neighboring atoms, a process of *sp2* hybridization. The strong in-plane covalent bonds (σ-bonds) give CNTs impressive mechanical properties. On the other hand, because of the extreme smallness, CNT structures contain very low defect density or are almost defect free, a major contributing factor to extraordinary properties. The measured specific tensile strength of CNT can be as high as 100 times that of steel, and the graphene sheet is the same stiff as diamond at low strain. It has been reported that the Young's modulus of a single wall carbon nanotube (SWNT) is 1 - 1.2 TPa [2-7], tensile strength of around 37 GPa at a failure strain of around 6% [2, 8, 9].

Depending on the rolling direction of the graphene sheet, single-walled carbon nanotubes (SWNT) of different chirality can be formed. There are three different chiralities: armchair, zigzag, and chiral, as shown in Figure 4.1.

A conventional way of identifying the types of SWNT is by reference to rolling of the graphene sheet. The key geometric parameters associated with the roll-up vector ***r***, can be expressed as the linear combination of the lattice basis (***a*** and ***b***), following the notation in references [10, 11] and Figure 4.2:

$$r = na + mb$$

Depending on their chiral vector, carbon nanotubes with small diameters are either semi-conducting or metallic. The differences in conducting properties are caused by the molecular structure that results in a different band structure and thus a different band gap.

Armchair nanotubes are classified at metallic, while zigzag and chiral nanotubes are classified as semiconductor. Electronic transport in metallic SWNT occurs ballistically over the length of the tube due to the one-dimensional electronic structure that prevent scattering thus allowing SWNT the capability to carry high currents without heat generation[2, 12, 13]. The Young's modulus of SWNT shows small dependence on the tube diameter and chirality [3, 14, 15].

Based on the definition of SWNT, multi-walled nanotubes (MWNT) can be considered as a collection of concentric SWNTs with different diameters. The length and diameter of these structures differ a lot from those of SWNTs and, of course, their properties are also very different.

As mentioned before, carbon nanotubes have superior mechanical properties due to their small sizes and very low defect density. However, a range of tensile modulus (0.4 – 5 TPa) and tensile strength (37 – 200 GPa) of SWNT has been reported over the years. The large variation in the values arising from the different methods of calculation and assumption, primarily due to the assumed thickness of the nanotube wall which lead to a large variation in cross sectional area and thus the modulus and strength. A comparison of Young's modulus of CNTs estimated by various groups of researchers is provided in

Table 4.1. The most impressive feature of SWNTs is the density-normalized tensile modulus and strength, around 19 and 56 times that of steel wire, and 2.4 and 1.7 times that of silicon carbide rods respectively [2, 16]. These mechanical properties motivate further study of lightweight and high strength materials such as SWNT reinforced polymer.

Besides the fantastic mechanical properties, CNTs also have other attractive features, such as their electronic, optical and chemical characteristics, which open a way to future applications. Fundamental and practical nanotube researches have shown possible applications in the fields of energy storage, molecular electronics, nanomechanical devices, and composite materials.

- Electrical conductivity. Depending on their chiral vector, carbon nanotubes with a small diameter are either semi-conducting or metallic. The differences in conducting properties are caused by the molecular structure that results in a different band structure and thus a different band gap. The differences in conductivity can easily be derived from the graphene sheet properties [17]. It was shown that a (n,m) nanotube is metallic as accounts that: $n=m$ or $(n-m) = 3i$, where i is an integer and n and m are defining the nanotube. The resistance to conduction is determined by quantum mechanical aspects and was proved to be independent of the nanotube length [18]. General information on electron conductivity is referred to a review by Ajayan and Ebbesen [19].

- Optical activity. Theoretical studies have revealed that the optical activity of chiral nanotubes disappears if the nanotubes become larger [20].Therefore, it is expected that other physical properties are influenced by these parameters too. Use of the optical activity might result in optical devices in which CNTs play an important role.

- Chemical reactivity.[21] Compared with a graphene sheet, the chemical reactivity of a

CNT is enhanced as a direct result of the curvature of the CNTs' surface. Carbon nanotube reactivity is directly related to the pi-orbital mismatch caused by an increased curvature. Therefore, a distinction must be made between the sidewall and the end caps of a nanotube. For the same reason, a smaller nanotube diameter results in increased reactivity. Covalent chemical modification of either sidewalls or end caps has shown to be possible. For example, the solubility of CNTs in different solvents can be controlled this way. Direct investigation of chemical modifications on nanotube behavior is difficult as the raw nanotube samples are still not pure enough.

4.1.2 Dispersion and functionalization of CNTs

It is essential to have a good dispersion and orientation of the CNTs in order to combine their properties with other materials and optimize the properties of the final product, especially in the nanocomposite application. Pure CNTs have smooth and uniform surfaces along the axis. So they have high affinity to attract each other and form aggregates, packed ropes, or entangle into networks due to strong van der Waals attraction in between them. Another important reason for the poor dispersion of as-produced CNTs is due to the existence of large amount of impurities, such as graphite sheets, amorphous carbon, metal catalyst and the smaller fullerenes. These impurities will also interfere with the desired properties of the CNTs and impair maximum translation of their properties to the meso- and macro structural levels. Therefore, it is essential to purify and functionalize CNTs in order to obtain good dispersion of CNTs with high purity. Common methods used to purify the CNTs include oxidation, acid treatment, annealing, ultrasonication and etc.

Oxidative treatment of the CNTs is a good way to remove carbonaceous impurities [22-26] or to clear the metal surface [24, 25, 27-30]. These impurities have relatively more defects or a more open structure so that the damage to CNTs is less than the damage to the impurities. The efficiency and the yield of the procedure are highly dependent on a lot of factors, such as metal content, oxidation time, environment, oxidizing agent and temperature.

In general the acid treatment will remove the metal catalyst. First of all, the surface of the metal must be exposed by oxidation or sonication. The metal catalyst is then exposed to acid and solvated. The CNTs remain in suspended form. When using a treatment in HNO_3, the acid only has an effect on the metal catalyst[22, 24]. The mild acid treatment (4 M HCl reflux) is basically the same as the HNO_3 reflux, but here the metal has to be totally exposed to the acid to dissolve it.

After the purification process, ultrasonication technique has to be used to obtain individually dispersed nanotubes instead of bundles, by which particles are separated due to ultrasonic vibrations. Agglomerates of different nanoparticles will be forced to vibrate and will become more dispersed. The separation of the particles depends on the surfactant, solvent and reagent used. The solvent influences the stability of the dispersed tubes in the system.

Recently, further functionalization of the nanotubes has been introduced in order to increase the solubility of them in specific solvents. Common methods include CNT oxidation and introduction of carboxyl-based couplings, electrochemical modification of nanotubes and photochemical functionalization of nanotubes. These methods have been elaborated upon in several papers [31-34].

4.1.3 Carbon nanotube reinforced polymer composites

Based on their properties, one of the most important applications of carbon nanotubes will be working as reinforcements in composite materials. Because of the stiffness of carbon nanotubes, they are ideal building blocks for structural applications. For example, they may be used as reinforcements in high strength, low weight, and high performance composites. Theoretically, SWNTs could have a Young's Modulus of 1 TPa. MWNTs are weaker because the individual cylinders slide with respect to each other. A main advantage of using nanotubes for structural polymer composites is that nanotube reinforcements will increase the toughness of the composites by absorbing energy during their highly flexible elastic behaviors. Other advantages are the low density of the nanotubes, an increased electrical conduction and better performance during compressive load. Nanotubes also sustain large strains in tension without showing signs of fracture. In other directions, nanotubes are highly flexible [19]. And the main problem remained is to create a good interface between nanotubes and the polymer matrix, as nanotubes are very smooth and have a small diameter, which is nearly the same as that of a polymer chain.

Another possibility, which is an example of a non-structural application, is filling of photoactive polymers with nanotubes. PPV (Poly-p-phenylenevinylene) filled with MWNTs and SWNTs is a composite, which has been used for several experiments. These composites show a large increase in conductivity with only a little loss in photoluminescence and electro-luminescence yields. And the composite is more robust than the pure polymer.

Polymer/carbon nanotube composites could also be used in other areas. For instance, they could be used as low-cost conducting materials. As reported by Sandler et al [35] the electrical percolation threshold occurs at 0.0025 wt. % CNT and at 1 wt. % CNT the composite exhibits a conductivity of 2 S/m. Sreekumar et al [36] also reported noticeable increase in electrical conductivity of specially prepared high content SWNT/oleum films. The conductivity was an order magnitude lower than individual SWNT but much higher than that of the SWNT bucky paper (a nonwoven mesh of SWNT). Liu et al [37] studied the supercapacitor properties of SWNT/PAN and SWNT/activated carbon films. The results indicated that the SWNT activated carbon film exhibited a non-linear discharging behavior and the power and energy densities were significantly higher. Kymakis et al [38] found that the optical and dielectric properties of SWNT/poly(3-octylthiophenes) composite film can be specifically designed by controlling the volume fraction of SWNT in the composite.

4.1.4 Carbon nanotubes reinforced polymer composite fibers by electrospinning

Aside from CNT reinforced polymer bulk composites, another area of high interest is polymer/CNT composite fibers. It had been proved by Griffith that strength of the fiber increases as fiber diameter decreases [39]. This trend has been utilized in commercial carbon fibers and has illustrated tremendous improvement in mechanical properties. It is hypothesized that if the fiber diameter is further decreased to the nanoscale levels, and also if the fiber is reinforced with CNTs, then the properties might increase further. Due to the extreme fineness of the CNT, which imposes tremendous difficulty in handling and processing of the material, the use of a carrier media or polymer matrix to assemble them into continuous fibers is necessary. This would enable them to be integrated into higher order structures, thus bridging the dimensional and properties gap between the nanoscale and macroscopic structures.

Utilizing polymer as a carrier media to assemble the CNTs into continuous filament allows well-controlled alignment and tailored distribution of the CNTs within an external structure. Tailoring the multiple outstanding properties of CNTs with appropriate polymer matrix systems in filament or fine fiber forms enabled them to be integrated into textile structures for advanced composite applications. Electrospinning provides a relatively simple and versatile method to produce polymer and its composite nanofibers. In conventional fiber spinning, alignment of the reinforcement (CNT) is mainly achieved by the flow of the polymer solution/melt and by post treatment such as mechanical drawing or stretching. The unique feature in electrospinning is that alignment of the CNT is induced by three factors: the flow of the polymer solution, the presence of electrostatic charge, and nanometer diameter confinement [40]. Flow induced alignment can be visualized as a “logs in the river” analogy as shown in Figure 4.3 where the SWNT tends to orient in the direction of flow along the fiber. The presence of electrostatic charge further orients the CNT along the fiber due to the stretching of the polymer jet. Stretching of the polymer jet also induces molecular orientation. Lastly, diameter confinement is introduced due to the fact that the produced fibers are in the nanometer diameter and the SWNTs are ~1 - 2 µm in length. Normally, the SWNTs appear in bundles of relatively longer length. Therefore, orientation of the SWNT ropes along the fiber direction is confined by the diameter of the nanofibers.

By electrospinning polyethylene oxide (PEO) solution containing a low concentration of MWNT, Dror et al. successfully prepared PEO/CNT composite fibers [41]. Ko’s group [40] and Haddon’s group [42] have also reported the preparation of single-walled carbon nanotubes filled polymer nanofibers respectively [32]. These nanofibers were highly reinforced due to the addition of CNTs. More recently, Hou and Ge et al. have prepared oriented polyacrylonitrile (PAN)/CNT nanofibers with high concentrations of well-aligned CNTs [31, 43]. However, all of these earlier attempts paid much attention only to the significantly increased mechanic properties of the composite nanofibers. A detailed study of electrical properties of these highly ordered composite nanofibers have not be addressed. Remarkable electrical properties of these carbon nanotubes filled composite nanofibers are becoming more interesting for future applications in nanoelectronics and sensing device design.

In this chapter, an oxidation method was used to introduce carboxylic acid (-COOH) functional group to the as-purchased MWNTs. Conducting poly(vinyl acetate) (PVAc) nanofibers filled with functionalized MWNTs and as-purchased raw MWNTs were fabricated by electrospinning. The relationship between the electrospinning parameters and the composite nanofiber morphologies has been investigated. Alignment of the composite nanofibers has been achieved by using a rotating drum as the collector. An AFM-based three-point-bending method was developed to study the mechanical properties of individual composite nanofibers with various concentrations of f-MWNTs. Electrical properties of a single composite fiber have been investigated at room temperature as well as cryogenic states.

4.2 Experimental

4.2.1 Materials

Unbundled MWNTs were obtained from Ahwahnee Technology Inc. Poly(vinyl acetate) (PVAc, Mw=500,000) was purchased from Sigma-Aldrich. N, N'-dimethylformamide (DMF) (certified A.C.S., Fisher Scientific Inc.), a good solvent for both PVAc and MWNTs, was utilized to prepare the electrospinning solution.

4.2.2 Functionalization of MWNT

MWNT were acquired from Ahwahnee Technology Inc. Two types of MWNT were used: (1) MWNT purchased directly from the company without further purification; (2) MWNT treated by reflux in 6 M HNO_3 for 12 h followed by filtration and a wash with deionized water. The oxidization method has been introduced in some references [31, 32, 34] [44]. The specific procedure has been developed by Dr. Samuilov and Koo in the Department of Materials Science and Engineering of Stony Brook University, referring to the procedures in the references. It has been described as following:

a. 500 mg of MWNT were dispersed in 50 ml of acid mixture;

(3:1 = H_2SO_4(98wt%):HNO_3, volume ratio)

b. The mixture was ultra-sonicated for 3 hours in a water bath;

c. The solution was stirred for 5 hours at 55°C;

d. The temperature was decreased to 35°C and kept it stirred for 43 hours;

e. The mixture was filtered by using 0.1 micron PVDF filter;

f. The filtered oxidized MWNT was extensively washed with deionized water until pH became neutral;

g. The powder was dried in the oven for 1 day (~ 90^{o}C).

4.2.3 Preparation of the PVAc/MWNT composite solutions

The electrospinning set-up is shown in Figure 4.4. A syringe was attached to a pump (KDS200, KD Scientific Inc.) which provided a steady solution flow rate of 20μl /min during electrospinning. A high voltage power supply (Gamma High Voltage Research, 0-30 kV) was employed to generate a high potential of 11kV to a 25 gauge blunt end syringe needle (I.D. 0.26mm, Popper & Sons Inc.). The electrospun nanofibers were collected onto a piece of static aluminum foil as well as high-speed rotating drum, which was intended to align the as-spun composite fibers.

In this experiment, PVAc was selected as the polymer template for making composite nanofibers because it has proved to be able to form uniform ultrathin fibers (tens of to hundreds of nanometers in diameter) from its DMF solution, while DMF is also a good solvent for suspending MWNTs. Pure PVAc nanofibers were first prepared by electrospinning for comparison. The most stable electrospun jet and uniform PVAc fibers were obtained when the PVAc concentration was 0.18g/ml in DMF. Therefore, in all of the subsequent experiments, PVAc concentrations were fixed at 0.18g/ml. The procedure for preparing the PVAc-MWNT composite solutions was described as following: (1) a certain amount of MWNT was suspended in DMF solvent and stored in a sonicator for 3 hours in order to obtain a good dispersion of MWNT in DMF; (2) PVAc was then added to the MWNT/DMF suspension and stirred for 48 hours to get a uniform and viscous composite solution; (3) the composite solution was loaded into a 5 ml glass syringe (Popper & Sons, Inc.) for electrospinning.

4.3 General Characterization Methods

TEM is an effective tool for observation of the CNT orientation in the electrospun nanofibers since the CNT possesses a higher density compared with polymer matrix. The nanotubes containing hollow structures have a darker concentric tubular structure embedded within the polymer nanofibers in the TEM image compared with the uniform template. A Philips CM12 TEM with a LaB6 filament at 120kV was employed to investigate the dispersion of MWNTs in the solution and the alignment of carbon nanotubes within the nanofibers. Field emission Scanning Electron Microscopy (FE-SEM, LEO 1550) has been utilized at an accelerating voltage of 15 kV in order to get a general morphology of the composite nanofibers. Raman spectroscopy was recorded by a Thermo Nicolet Almega® micro-Raman spectrometer with a 785 nm probe beam.

A single composite fiber was collected between two gold electrodes (on a piece of Si chip) with the interval distance of 10μm between the two electrodes. I-V characteristic curves of a single composite nanofiber were measured by a 2-point probe method by a multimeter (Keithley Model 6430) with an applied voltage up to 0.5V.

4.4 Results and Discussion

4.4.1 Dispersion of MWNTs in the solution

The dispersion of MWNTs in the polymer solution was directly determined by the dispersion of MWNTs in the DMF suspension. MWNTs before and after functionalization were dispersed in the DMF solvent with the same concentration, followed by ultra-sonication for 3 hours. A uniform ink-like black solution was obtained for the suspension of functionalized MWNT (f-MWNT) without any precipitation. The suspension was homogeneous even after staying in air for 3 days. For the un-functionalized MWNT (u-MWNT), MWNT could not be dispersed uniformly. An obvious phase separation happened soon after stopping sonication. A random drop of each suspension was dropped onto a TEM grid and dried in air naturally. Dispersions of these two different kinds of MWNTs in the suspension were observed, as shown in Figure 4.5. It can be seen that MWNTs before functionalization formed agglomerates in the dispersion. Amorphous carbon on the outer wall of CNTs made the nanotubes look thicker and rougher. Greatly improved dispersion of MWNTs was obtained for the f-MWNTs. They were not entangled with each other any more. And the amount of amorphous carbon was significantly less after purification. The improvement of the MWNTs' dispersion can be attributed to two factors. One is the decrease in the amount of impurities such as catalysts and amorphous carbon, which came from the growth of CNTs; the other is the introduction of carboxylic groups into the MWNTs after the oxidation process, which improved the interactions between MWNTs and the solvent DMF. An interaction model of DMF and MWNTs modified with carboxylic groups has been suggested in Hou and Ge's paper [31].

4.4.2 Morphology of the PVAc/MWNTs composite nanofibers

Composite nanofibers were prepared by electrospinning PVAc/MWNT composite solution with various mass concentrations of carbon nanotubes. The rotation speed of the drum collector was 1000 rpm, corresponding to a linear velocity of about 3.0m/s at the surface of the drum. Both f-MWNTs and u-MWNTs were used for preparing the nanofibers. Based on our SEM image (Figure 4.6(A)) of the as-prepared pure PVAc fibers from the 0.18g/ml PVAc solution, fibers were obtained with uniform diameter distribution around 100nm, as also presented in Figure 4.6 (A’). However, after adding 5wt% u-MWNTs, the composite fibers demonstrated a discrete size distribution (Figure 4.6(B) and (B’)). The fiber diameters ranged from tens of nanometers to a few hundred nanometers. The alignment of the fibers was poor, especially for thinner fibers. Such a non-uniform distribution of fiber diameters implied an unstable electrospinning process after adding u-MWNTs into the polymer solution, which resulted in the non-homogeneity of the composite solution. And the sink flow and high extension of the electrospun jet cannot overcome the entanglement force of the MWNTs. Therefore, the surface tension of the solution was significantly non-homogeneous. This could prevent the electrospinning process from happening smoothly. Further study of the as-spun fibers by TEM showed entangled MWNTs in most thick fibers (see Figure 4.7 (A)), while fibers with diameters less than 50nm hardly have any CNTs embedded in them. This phenomenon was greatly improved by using f-MWNTs. Figure 4.6(C) demonstrated SEM picture of the PVAc/MWNTs composite nanofibers containing 5% f-MWNTs by weight. Composite fibers with centralized size distribution were obtained, as shown in Figure 4.6(C’). Much better alignment of the composite fibers was also achieved by using the collector with the same rotating speed. From TEM pictures, CNTs were found to align parallel to the axis direction of the nanofibers (see Figure 4.7(B)(C)). In some fibers, several carbon nanotubes could be aligned side by side in a single polymer fiber of around 100nm in diameter (see Figure 4.7 (D), arrows point at 4 parallel MWNTs). In a large scale, the parallel alignment of the composite fibers also resulted in the ordering of CNTs aligned in separate nanofibers. It is notable that carbon nanotubes are not separately aligned due to the good dispersion state of the f-MWNTs at a high concentration. Most of them were found to connect with each other. Arrows in Figure 4.7 (B, C) point at the junction of two consecutive MWNTs respectively. The parallel and serial connections of MWNTs along the polymer nanofibers provided effective channels for electrons transportation, which made it possible to obtain conducting composite nanofibers.

4.4.3 Raman spectrum

The existence of MWNTs in the aligned composite fibers was confirmed by Raman spectroscopy. The MWNTs wrapped in PVAc matrix showed strong Raman scattering as pure MWNTs. Figure 4.8 is the Raman spectra of the nano-composite fibers with various concentrations of MWNTs. Two characteristic peaks were observed for all the compositions. The strong peak at 1329 cm^{-1} could be explained as disorder-induced features due to the finite particle size effect or lattice distortion of graphite crystals in the CNTs [31, 45]. The other strong peak at around 1578 cm^{-1} was assigned as a graphite order peak. These two characteristic peaks were also called D line and G line respectively [31, 45]. The intensity of CNT Raman scattering peaks increased with the increase of the MWNT concentrations in the composite nanofibers, although the intensity was not proportional to the MWNT concentration.

4.4.4 I-V characteristics of the composite nanofibers

Electrical conductivity of a single composite nanofiber was measured by a simple 2-point probe method. Nanofibers with different concentrations of f-MWNTs were measured. Figure 4.9(A) showed representative temperature-dependent current-voltage (I-V) characteristics of a single composite fiber loaded between two gold electrodes. The composite fiber was made from a PVAc/DMF solution containing 5wt% f-MWNT. In contrast with some reported results [45], non-linear I-V characteristics were obtained for the fiber from 100K to room temperature, implying the semi-conducting property of this fiber. Further calculation of the conductance ($G_0 = \left.\frac{dI}{dV}\right|_{V=0}$) at various temperatures was plotted in Figure 4.9(B). The data can be well fitted by a straight line, indicating a linear relationship between $\ln G_0$ and 1/T. This behavior is similar to that of the semiconductor-metal contact. From simple band theory, we know that the excitation of valence band to conducting band is proportional to $\exp(-E_a/k_B T)$ [46], where E_a is the activation energy for the semiconductor. As for the temperature dependence of the composite nanofibers conductance, linear relationship between $\ln G_0$ and 1/T gives us activation energy of our semiconducting PVAc/MWNT composite nanofibers, which is 55±4meV, as calculated from 10 different samples. It is notable that the semiconducting characteristics demonstrated by the composite nanofiber are the integrated property of all the carbon nanotubes embedded in the fiber. It is well established theoretically that the electronic structure of a carbon nanotube depends much on the nanotube chirality and diameters [47-51]. Carbon nanotubes obtained from the regular method are usually a mixture of metallic, semiconducting, and semi-metallic carbon nanotubes. Therefore, the properties of the composite fiber could be affected by the intrinsic properties of the carbon nanotubes used as well as the factors that may affect the electron transportation along the fiber axis direction. The specific mechanism of the conductivity of these composite fibers needs further study.

The room temperature DC conductivities calculated for the PVAc/MWNT composite fibers were plotted with respect to the MWNT to polymer weight ratio (see Figure 4.10). It is known that pure PVAc is not a conducting material with the conductivity of the order of 10^{-13} S/m [52]. The presence of carbon nanotubes significantly improved the conductivity of the polymer fibers due to their highly conductive graphitic structures. A percolation behavior was observed with the percolation threshold of around 0.5wt%. Beyond this limit, conductivity increases slowly with the increase of the MWNT mass fraction. This percolation limit is higher than that of other polymer/MWNT composites in the references [45, 53, 54]. It is related with the intrinsic properties of the MWNT used. Another explanation can be that electron transportation channel was narrowed down to only 1D in the single aligned composite fiber with diameter of 100nm, while carbon nanotubes may form 3D networks in the bulk polymer/MWNT composites or thicker composite fibers. The lower dimension of the conducting nanofiber enhanced the percolation limit required for high conductivity.

4.5 AFM for Mechanical Properties Test

4.5.1 Introduction to the AFM force curve

The Atomic Force Microscope (AFM) offers the opportunity not only to measure the topography of surfaces but also to investigate the mechanical properties of surfaces and fibers on the nanometer scale. The mechanism behind the mechanical property test is to use the AFM tip to apply nano-scale force onto the nano-surface and cause small strain on top of the surface. Based on the available elastic theories, the Young’s modulus of the nano-surface can be calculated in terms of the known mechanic parameters of the material, the cantilever, and the AFM tip. A new method has been applied here for the measurement of the Young's modulus of individual electrospun nanofiber in this research: three point bending method. This method is based on the elastic response of the materials from the force curve by AFM. The AFM used in this experiment was AFM (Dimension 3100, Digital Instruments (DI)) operated in contact mode.

A force calibration plot is an observation of tip-sample interactions, which yields information regarding the sample and tip. In Force Calibration mode, the x and y voltages applied to the piezo tube are zero and a triangular waveform is applied to z electrodes of the piezo tube. The cantilever tip moves up and down relative to the stationary sample, as a result of the applied voltage (see Figure 4.11).

As the piezo moves the tip up and down, the cantilever-deflection signal from the photodiode is monitored. The force curve just plots the cantilever deflection signal as a function of the voltage applied to the piezo tube. The values of both axes can be transformed from voltage to distance by proper calibration. By adjusting the detailed parameters controlling the microscope, a complete force curve can be displayed. A typical example force curve is shown in Figure 4.12, which was obtained from a contact mode AFM using a silicon nitride tip. The horizontal axis plots the tip movement relative to the sample. By extending the z-axis piezo crystal, the tip descends toward the sample and the tip-sample distance decreases. The descent plots from right to left from point 0 to 4 in Figure 4.12. By retracting the z-axis piezo crystal, the tip ascends away from the sample, and the tip-sample distance increases. The ascent plots from left to right from point 4 to 6 in Figure 4.12. Cantilever deflection plots on the vertical axis of the graph. When the cantilever deflects downward, it plots on the graph's downward vertical; when it deflects upward, it plots on the upward vertical. A detailed process is described step by step as following:

Starting from point 0 to 1, piezo tube extends; tip descends toward the sample surface, but no contact yet. As tip approaching the sample surface, an attractive force near the surface pull tip down (point 1→2). The tip begins to press into the surface, and the cantilever bends upward. The deflection of the cantilever vs. descending distance of the piezo is plotted as a straight line from point 2 to 4. After reaching the z limit, piezo tube retracts. The tip ascends until forces are in equilibrium with surface force. Then tip ascends further, but cantilever bends downward as surface attraction holds onto the tip. At a certain critical point 5, the bending force overwhelms the surface attraction. And cantilever rebounds sharply upward (point 5→ 6). Then the tip continues ascending without any contact with the sample surface (point 6 → 0). A circle ends at point 0. In the whole process, the value of z can be directly recorded by the controller electronics system, while the cantilever deflection can be read as voltage signal. AFM provides an alternative distance display of cantilever deflection. But a reference material must be used in order to correlate voltage change signal to cantilever deflection distance.

4.5.2 Three point bending method

In the three point bending method, the nanofiber was taken as an isotropic beam suspended over a microsized groove etched on a silicon wafer (see Figure 4.13). Due to the adhesion between the fiber and the silicon substrate and the much greater length of the nanofiber than the suspended length, it is reasonable to assume that both ends of the nanofibers are fixed and remain in place even after the test is conducted. The AFM tips were dulled by strongly tapping them with the AFM against a hard Si substrate for more than 20 min. The resultant radii of curvature of the tips were comparable to the fiber diameters, and thus it was unlikely that they would penetrate the fiber.

As shown in Figure 4.13, Force calibration curves were obtained using an AFM operated in contact mode. Raw AFM data were translated to force–displacement curves by converting the tip deflection ΔZ_c to a force using the cantilever spring constant and the height change of the AFM probe ΔZ, using $\delta(Z) = \Delta Z - \Delta Z_c$, where $\delta(Z)$ is the displacement of the middle point of the fiber, ΔZ is the AFM probe's position change relative to the initial contact point. According to the standard cubic equation for the displacement of a suspended elastic string with fixed ends (in the small deflection approximation):

$$\delta = \delta_B + \delta_S = FL^3 / 192EI + f_s FL / 4GA$$

where δ_B is the displacement caused by tension, δ_S is the displacement caused by shear effect, A is the cross-sectional area of the fiber, E is the Young's modulus of the fiber, L is the suspended length of the fiber, f_s is the shape factor (equal to 10/9 for a cylindrical beam), G is the shear modulus, I is the second moment of area of the beam ($I = \pi D^4/64$ for a filled cylinder). This equation describes the force due to elongation of the string caused by displacement at L/2. And we assume that the material is linearly elastic in this model [55, 56]. The ratio δ_B / δ_S increases with the ratio of beam length to diameter. When *G* and *E* are of comparable magnitude, shear effects become important only for relatively short beams. In this experiment, the ratio of beam length to diameter is large enough for neglecting δ_S, which is due to the contribution of shear. If the initial tension T_0 is zero, we can get:

$$\delta = FL^3 / 192EI$$

Therefore, Young's modulus E can be calculated, if δ , F, L and I are known.

4.5.3 Mechanical properties of CNT reinforced polymer composite nanofibers

Samples were obtained by aligning the fibers onto a piece of Si chip, in which several trenches had been etched. The trenches were 20μm wide and 5μm deep. Alignment was achieved by rotating the collector in a way described earlier (Figure 4.4). Figure 4.14 shows the representative SEM image of the fibers suspended over the trenches. The realistic beam length can be calibrated by measuring the angle between the fiber and the edge of the trench.

Figure 4.15 shows the AFM tip used for the three point bending method. (A) and (B) are the same tip before and after dulling against a piece of Si wafer. It is ready to see that the resulted radius of the curvature of the tip was around 200nm, which was comparable to the fiber diameters. Thus, it can be prevented from penetrating the fibers.

In order to obtained observable cantilever deflection, a silicon nitride cantilever with nominal spring constant of 0.32N/m was used. First, a piece of cleaned Si wafer was used as the reference material to calibrate the deflection sensitivity of the force curve (see Figure 4.16(A)), so that the following cantilever deflection distances can be read directly from the force curve. Then the AFM probe was aligned to the center of the suspended fiber (L/2) by continuously scanning the suspended fibers and step-by-step careful zoom-in. Finally, the force curve was obtained from the middle of one of the individually suspended electrospun nanofibers.

In this experiment, a series of PVAc/MWNT composite fibers with different diameters have been measured. Some typical force curves and AFM 3-d images of the fibers are shown in Figure 4.16. In order to used formula (1), the loading force was calculated by $F = k \cdot \Delta Z_c$, where k=3.2N/m; the fiber deflection was obtained by $\delta(Z) = \Delta Z - \Delta Z_c$; L is obtained by measuring the width of the trench and the angle of the fiber with respect to the trench walls; $I = \pi D^4/64$ for a filled cylinder. Therefore, Young' moduli can be calculated from all the available parameters.

The variation Young' modulus with the fiber diameters is plotted in Figure 4.17. Composite fibers with diameters less than 300nm have much higher Young's modulus (more than 100GPa) than both the bulk polymer and their fibular counterparts. It can be attributed to two reasons. One is the formation of highly oriented molecular chains of the polymer aligned along the fiber direction during the electrospinning process. This has been suggested as a common reason for the strengthening of ultrathin polymer fiber than bulk materials. The other reason is the addition of MWNT. The theoretic modulus for a single regular MWNT is around 1TPa. In the composite fibers, it has been observed by TEM that most MWNTs are oriented along the fiber direction. For thinner fibers with MWNT in them, they tend to align better, while MWNT tend to agglomerate or curve in thick fibers. Therefore, it is reasonable to deduct that thinner fibers may have orders of higher elastic modulus due to the oriented MWNTs in them. This tendency has been indicated in Fig.4.17 by fitting the data with an exponential decay curve. A significant decrease of the elastic modulus happens with the increase of the fiber diameters. Especially when the fiber diameters are larger than 350nm, Young's modulus decreases to lower than 50GPa. And that value is only a few GPa for fibers with diameters higher than 650nm.

Sources of errors in the results come from the nominal value of the cantilever spring constant, the measurement of the fiber diameter and the length of the suspended fiber, the difference between the middle point of the suspended fiber and the realistic contact position for the force curve, and also, the reading from the force curve for the deflection parameters.

4.6 Conclusions

We have successfully functionalized MWNTs using an oxidization method. Continuous and well-aligned PVAc/MWNT composite nanofibers were fabricated by electrospinning a composite solution of PVAc/DMF and the f-MWNTs prepared above. Compared with u-MWNTs, the functionalized CNTs were found to have a more homogeneous dispersion in the solution state and align better along the axes of the electrospun polymer fibers. DC electrical properties of a single composite fiber with f-MWNTs were investigated at room temperature as well as cryogenic states. It was found that the presence of aligned CNTs provided an effective channel for electrical conductance along the nanofiber. The composite nanofibers (containing 5wt% f-MWNTs) demonstrated a semi-conducting property, with activation energy of 55±4meV as calculated from the I-V characteristics dependence on temperatures. Conductivity of the composite nanofiber was enhanced by ten orders compared with that of the pure polymer, with a percolative threshold of 0.5% mass fraction of MWNT in the composites.

By loading the aligned nanofibers on top of a microsized groove etched on a silicon wafer, the condition for three point bending measurement was established. AFM tip was employed as a probe, which could apply a measurable deflection and force onto the suspended nanofiber at a force calibration mode, so that the Young’s modulus of a single nanofiber can be calculated based on the basic beam bending theories. AFM force calibration curve measurements show that polymer nanofibers tend to have a higher Young's modulus than their bulk counterparts, due to the highly aligned molecular chains formed during the electrospinning process. The polymer nanofibers containing MWNTs exhibit even higher Young's modulus than their fibular counterparts because of the reinforcement effects from the highly aligned MWNTs along the fiber axis. The mechanical properties of the composite nanofibers improve significantly with decreased fiber diameters. For the composite nanofibers with diameters less than 300nm, the nanofibers displayed a modulus over 100GPa.

References

1. Iijima, S., Helical Microtubules of Graphitic Carbon. *Nature* **1991,** 354, (6348), 56-58.

2. Baughman, R. H.; Zakhidov, A. A.; de Heer, W. A., Carbon nanotubes - the route toward applications. *Science* **2002,** 297, (5582), 787-792.

3. Salvetat-Delmotte, J. P.; Rubio, A., Mechanical properties of carbon nanotubes: a fiber digest for beginners. *Carbon* **2002,** 40, (10), 1729-1734.

4. Yakobson, B. I.; Campbell, M. P.; Brabec, C. J.; Bernholc, J., High strain rate fracture and C-chain unraveling in carbon nanotubes. *Computational Materials Science* **1997,** 8, (4), 341-348.

5. Nardelli, M. B.; Yakobson, B. I.; Bernholc, J., Mechanism of strain release in carbon nanotubes. *Physical Review B* **1998,** 57, (8), R4277-R4280.

6. Zhang, P. H.; Lammert, P. E.; Crespi, V. H., Plastic deformations of carbon nanotubes. *Physical Review Letters* **1998,** 81, (24), 5346-5349.

7. Nardelli, M. B.; Yakobson, B. I.; Bernholc, J., Brittle and ductile behavior in carbon nanotubes. *Physical Review Letters* **1998,** 81, (21), 4656-4659.

8. Walters, D. A.; Ericson, L. M.; Casavant, M. J.; Liu, J.; Colbert, D. T.; Smith, K. A.; Smalley, R. E., Elastic strain of freely suspended single-wall carbon nanotube ropes. *Applied Physics Letters* **1999,** 74, (25), 3803-3805.

9. Yu, M. F.; Files, B. S.; Arepalli, S.; Ruoff, R. S., Tensile loading of ropes of single wall carbon nanotubes and their mechanical properties. *Physical Review Letters* **2000,** 84, (24), 5552-5555.

10. Harris, P. J. F., *Carbon Nanotubes and Related Structure: New Materials for the Twenty-First Century*. Cambridge University Press: New York, 1999.

11. Saito, R.; Dresselhaus, G.; S., D. M., *Physical Properties of Carbon Nanotubes*. Imperial College Press: London, 1998.

12. Petit, P.; Loiseau, A., Carbon Nanotubes: from Science to Applications. *C. R. Physique* **2003,** 4, (9), 967.

13. Dresselhaus, M.; Dresselhaus, G.; Eklund, P.; Saito, R., Carbon Nanotubes. In PhysicsWeb: 1998.

14. Lu, J. P., Elastic properties of carbon nanotubes and nanoropes. *Physical Review Letters* **1997,** 79, (7), 1297-1300.

15. Hernandez, E.; Goze, C.; Bernier, P.; Rubio, A., Elastic properties of C and BxCyNz composite nanotubes. *Physical Review Letters* **1998,** 80, (20), 4502-4505.

16. Wong, E. W.; Sheehan, P. E.; Lieber, C. M., Nanobeam mechanics: Elasticity, strength, and toughness of nanorods and nanotubes. *Science* **1997,** 277, (5334), 1971-1975.

17. Avouris, P., Carbon nanotube electronics. *Chemical Physics* **2002,** 281, (2-3), 429-445.

18. Tans, S. J.; Devoret, M. H.; Dai, H. J.; Thess, A.; Smalley, R. E.; Geerligs, L. J.; Dekker, C., Individual single-wall carbon nanotubes as quantum wires. *Nature* **1997,** 386, (6624), 474-477.

19. Ajayan, P. M.; Zhou, O. Z., Applications of carbon nanotubes. In *Carbon Nanotubes*, 2001; Vol. 80, pp 391-425.

20. Damnjanovic, M.; Milosevic, I.; Vukovic, T.; Sredanovic, R., Full symmetry, optical activity, and potentials of single-wall and multiwall nanotubes. *Physical Review B* **1999,** 60, (4), 2728-2739.

21. Niyogi, S.; Hamon, M. A.; Hu, H.; Zhao, B.; Bhowmik, P.; Sen, R.; Itkis, M. E.; Haddon, R. C., Chemistry of single-walled carbon nanotubes. *Accounts of Chemical Research* **2002,** 35, (12), 1105-1113.

22. Borowiak-Palen, E.; Pichler, T.; Liu, X.; Knupfer, M.; Graff, A.; Jost, O.; Pompe, W.; Kalenczuk, R. J.; Fink, J., Reduced diameter distribution of single-wall carbon nanotubes by selective oxidation. *Chemical Physics Letters* **2002,** 363, (5-6), 567-572.

23. Huang, S. M.; Dai, L. M., Plasma etching for purification and controlled opening of aligned carbon nanotubes. *Journal of Physical Chemistry B* **2002,** 106, (14), 3543-3545.

24. Chiang, I. W.; Brinson, B. E.; Huang, A. Y.; Willis, P. A.; Bronikowski, M. J.; Margrave, J. L.; Smalley, R. E.; Hauge, R. H., Purification and characterization of single-wall carbon nanotubes (SWNTs) obtained from the gas-phase decomposition of CO (HiPco process). *Journal of Physical Chemistry B* **2001,** 105, (35), 8297-8301.

25. Harutyunyan, A. R.; Pradhan, B. K.; Chang, J. P.; Chen, G. G.; Eklund, P. C., Purification of single-wall carbon nanotubes by selective microwave heating of catalyst

particles. *Journal of Physical Chemistry B* **2002,** 106, (34), 8671-8675.

26. Farkas, E.; Anderson, M. E.; Chen, Z. H.; Rinzler, A. G., Length sorting cut single wall carbon nanotubes by high performance liquid chromatography. *Chemical Physics Letters* **2002,** 363, (1-2), 111-116.

27. Hou, P. X.; Liu, C.; Tong, Y.; Xu, S. T.; Liu, M.; Cheng, H. M., Purification of single-walled carbon nanotubes synthesized by the hydrogen arc-discharge method. *Journal of Materials Research* **2001,** 16, (9), 2526-2529.

28. Kajiura, H.; Tsutsui, S.; Huang, H. J.; Murakami, Y., High-quality single-walled carbon nanotubes from arc-produced soot. *Chemical Physics Letters* **2002,** 364, (5-6), 586-592.

29. Moon, J. M.; An, K. H.; Lee, Y. H.; Park, Y. S.; Bae, D. J.; Park, G. S., High-yield purification process of singlewalled carbon nanotubes. *Journal of Physical Chemistry B* **2001,** 105, (24), 5677-5681.

30. Chiang, I. W.; Brinson, B. E.; Smalley, R. E.; Margrave, J. L.; Hauge, R. H., Purification and characterization of single-wall carbon nanotubes. *Journal of Physical Chemistry B* **2001,** 105, (6), 1157-1161.

31. Hou, H. Q.; Ge, J. J.; Zeng, J.; Li, Q.; Reneker, D. H.; Greiner, A.; Cheng, S. Z. D., Electrospun polyacrylonitrile nanofibers containing a high concentration of well-aligned multiwall carbon nanotubes. *Chemistry of Materials* **2005,** 17, (5), 967-973.

32. Balasubramanian, K.; Burghard, M., Chemically functionalized carbon nanotubes. *Small* **2005,** 1, (2), 180-192.

33. Velasco-Santos, C.; Martinez-Hernandez, A. L.; Fisher, F. T.; Ruoff, R.; Castano, V. M., Improvement of thermal and mechanical properties of carbon nanotube composites through chemical functionalization. *Chemistry of Materials* **2003,** 15, (23), 4470-4475.

34. Bekyarova, E.; Davis, M.; Burch, T.; Itkis, M. E.; Zhao, B.; Sunshine, S.; Haddon, R. C., Chemically functionalized single-walled carbon nanotubes as ammonia sensors. *Journal of Physical Chemistry B* **2004,** 108, (51), 19717-19720.

35. Sandler, J. K. W.; Kirk, J. E.; Kinloch, I. A.; Shaffer, M. S. P.; Windle, A. H., Ultra-low electrical percolation threshold in carbon-nanotube-epoxy composites. *Polymer* **2003,** 44, (19), 5893-5899.

36. Sreekumar, T. V.; Liu, T.; Kumar, S.; Ericson, L. M.; Hauge, R. H.; Smalley, R. E.,

Single-wall carbon nanotube films. *Chemistry of Materials* **2003,** 15, (1), 175-178.

37. Liu, T.; Sreekumar, T. V.; Kumar, S.; Hauge, R. H.; Smalley, R. E., SWNT/PAN composite film-based supercapacitors. *Carbon* **2003,** 41, (12), 2440-2442.

38. Kymakis, E.; Amaratunga, G. A. J., Optical properties of polymer-nanotube composites. *Synthetic Metals* **2004,** 142, (1-3), 161-167.

39. Griffith, A. A., *The Phenomena of Rupture and Flow in Solids*. Philosophical Transactions of the Royal Society of London: London, 1921; Vol. A221.

40. Ko, F.; Gogotsi, Y.; Ali, A.; Naguib, N.; Ye, H. H.; Yang, G. L.; Li, C.; Willis, P., Electrospinning of continuons carbon nanotube-filled nanofiber yarns. *Advanced Materials* **2003,** 15, (14), 1161-1163.

41. Dror, Y.; Salalha, W.; Khalfin, R. L.; Cohen, Y.; Yarin, A. L.; Zussman, E., Carbon nanotubes embedded in oriented polymer nanofibers by electrospinning. *Langmuir* **2003,** 19, (17), 7012-7020.

42. Sen, R.; Zhao, B.; Perea, D.; Itkis, M. E.; Hu, H.; Love, J.; Bekyarova, E.; Haddon, R. C., Preparation of single-walled carbon nanotube reinforced polystyrene and polyurethane nanofibers and membranes by electrospinning. *Nano Letters* **2004,** 4, (3), 459-464.

43. Ge, J. J.; Hou, H.; Li, Q.; Graham, M. J.; Greiner, A.; Reneker, D. H.; Harris, F. W.; Cheng, S. Z. D., Assembly of Well-Aligned Multiwalled Carbon Nanotubes in Confined Polyacrylonitrile Environments: Electrospun Composite Nanofiber Sheets. *Journal of the American Chemical Society* **2004,** 126, (48), 15754-15761.

44. Ciraci, S.; Dag, S.; Yildirim, T.; Gulseren, O.; Senger, R. T., Functionalized carbon nanotubes and device applications. *Journal of Physics-Condensed Matter* **2004,** 16, (29), R901-R960.

45. Sundaray, B.; Subramanian, V.; Natarajan, T. S.; Krishnamurthy, K., Electrical conductivity of a single electrospun fiber of poly(methyl methacrylate) and multiwalled carbon nanotube nanocomposite. *Applied Physics Letters* **2006,** 88, (14), 143114.

46. Hummel, R., *Electronic Properties of Materials*. Springer: New York 1992.

47. Hamada, N.; Sawada, S.; Oshiyama, A., New One-Dimensional Conductors - Graphitic Microtubules. *Physical Review Letters* **1992,** 68, (10), 1579-1581.

48. Saito, R.; Fujita, M.; Dresselhaus, G.; Dresselhaus, M. S., Electronic-Structure of

Chiral Graphene Tubules. *Applied Physics Letters* **1992,** 60, (18), 2204-2206.

49. Blase, X.; Benedict, L. X.; Shirley, E. L.; Louie, S. G., Hybridization Effects and Metallicity in Small Radius Carbon Nanotubes. *Physical Review Letters* **1994,** 72, (12), 1878-1881.

50. Kane, C. L.; Mele, E. J., Size, shape, and low energy electronic structure of carbon nanotubes. *Physical Review Letters* **1997,** 78, (10), 1932-1935.

51. Dresselhaus, M. S.; Dresselhaus, G.; Ecklund, P. C., *Science of Fullerenes and Carbon Nanotubes*. Academic Press: San Diego, 1996.

52. Segal, E.; Haba, Y.; Narkis, M.; Siegmann, A., Polyaniline/PVAc blends: Variation with time of structure and conductivity of films cast from aqueous dispersions. *Journal of Applied Polymer Science* **2001,** 79, (4), 760-766.

53. Safadi, B.; Andrews, R.; Grulke, E. A., Multiwalled carbon nanotube polymer composites: Synthesis and characterization of thin films. *Journal of Applied Polymer Science* **2002,** 84, (14), 2660-2669.

54. Martin, C. A.; Sandler, J. K. W.; Shaffer, M. S. P.; Schwarz, M. K.; Bauhofer, W.; Schulte, K.; Windle, A. H., Formation of percolating networks in multi-wall carbon-nanotube-epoxy composites. *Composites Science and Technology* **2004,** 64, (15), 2309-2316.

55. Salvetat, J. P.; Briggs, G. A. D.; Bonard, J. M.; Bacsa, R. R.; Kulik, A. J.; Stockli, T.; Burnham, N. A.; Forro, L., Elastic and shear moduli of single-walled carbon nanotube ropes. *Physical Review Letters* **1999,** 82, (5), 944-947.

56. Tan, E. P. S.; Lim, C. T., Physical properties of a single polymeric nanofiber. *Applied Physics Letters* **2004,** 84, (9), 1603-1605.

57. Yakobson, B. I.; Brabec, C. J.; Bernholc, J., Nanomechanics of carbon tubes: Instabilities beyond linear response. *Physical Review Letters* **1996,** 76, (14), 2511-2514.

58. Lu, J. P., Elastic properties of single and multilayered nanotubes. *Journal of Physics and Chemistry of Solids* **1997,** 58, (11), 1649-1652.

59. Krishnan, A.; Dujardin, E.; Ebbesen, T. W.; Yianilos, P. N.; Treacy, M. M. J., Young's modulus of single-walled nanotubes. *Physical Review B* **1998,** 58, (20), 14013-14019.

60. Li, F.; Cheng, H. M.; Bai, S.; Su, G.; Dresselhaus, M. S., Tensile strength of single-walled carbon nanotubes directly measured from their macroscopic ropes. *Applied*

Physics Letters **2000,** 77, (20), 3161-3163.

61. Zhou, G.; Duan, W. H.; Gu, B. L., First-principles study on morphology and mechanical properties of single-walled carbon nanotube. *Chemical Physics Letters* **2001,** 333, (5), 344-349.

62. Tu, Z. C.; Ou-Yang, Z., Single-walled and multiwalled carbon nanotubes viewed as elastic tubes with the effective Young's moduli dependent on layer number. *Physical Review B* **2002,** 65, (23).

63. Demczyk, B. G.; Wang, Y. M.; Cumings, J.; Hetman, M.; Han, W.; Zettl, A.; Ritchie, R. O., Direct mechanical measurement of the tensile strength and elastic modulus of multiwalled carbon nanotubes. *Materials Science and Engineering a-Structural Materials Properties Microstructure and Processing* **2002,** 334, (1-2), 173-178.

64. Chang, T. C.; Gao, H. J., Size-dependent elastic properties of a single-walled carbon nanotube via a molecular mechanics model. *Journal of the Mechanics and Physics of Solids* **2003,** 51, (6), 1059-1074.

65. Li, C. Y.; Chou, T. W., Elastic moduli of multi-walled carbon nanotubes and the effect of van der Waals forces. *Composites Science and Technology* **2003,** 63, (11), 1517-1524.

TABLES:

Table 4.1. Comparison of the Young's moduli of carbon nanotubes estimated by various groups.

Authors	E(TPa)	υ	Year	Method	Reference
Yakobson	5.5	0.19	1996	Molecular Dynamic	[57]
Lu	1	0.28	1997	Molecular Dynamic	[58]
Krishnan et al	1.25	-	1998	Theoretical	[59]
Yu et al	0.27-0.95	-	2000	Experimental	[9]
Li et al	0.79	-	2000	Experimental	[60]
Zhou et al	0.77	0.032	2001	Theoretical	[61]
Tu	4.7	0.34	2002	Theoretical	[62]
Demczyk et al	0.9	-	2002	Experimental	[63]
Chang and Gao	1.325	0.26	2003	Molecular Dynamic	[64]
Li and Chou	1.05	-	2003	Finite Element Modeling	[65]

FIGURES:

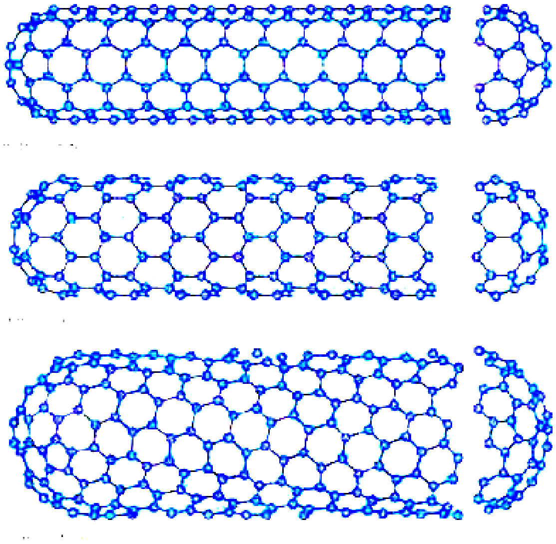

Figure 4.1. Some SWNTs with different chiralities: armchair structure, zigzag structure and chiral structure. The difference in structure is easily shown at the open end of the tubes. (Adapted from http://www.personal.rdg.ac.uk/~scsharip/tubes.htm)

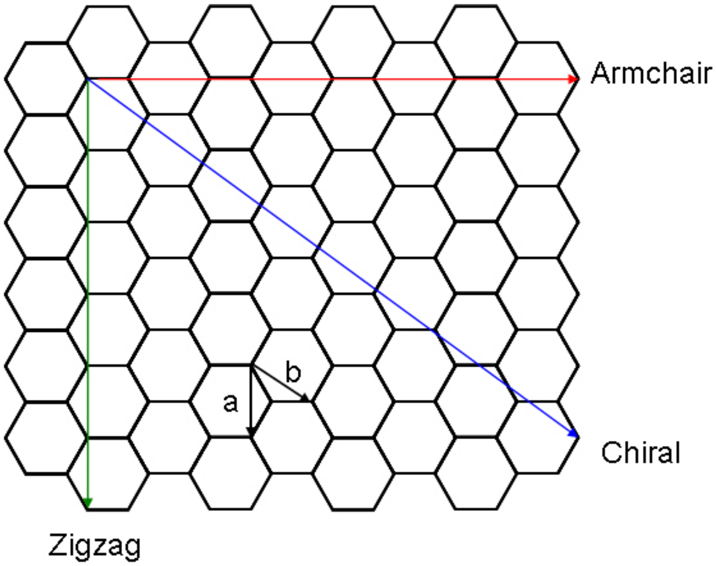

Figure 4.2. SWNTs of different chiral vectors: armchair, helicity of 0°; zigzag, helicity of 30°; and chiral, helicity between 0° and 30°.

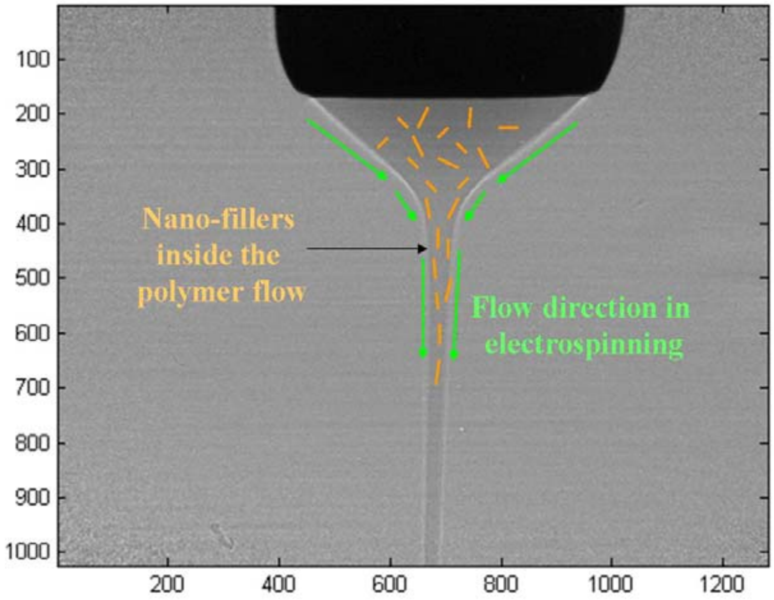

Figure 4.3. X ray transmission image of the tailor cone formed at the beginning of the electrospinning process, schematically showing the flow induced "logs in the river analogy" alignment of nanofillers inside the nanofiber.

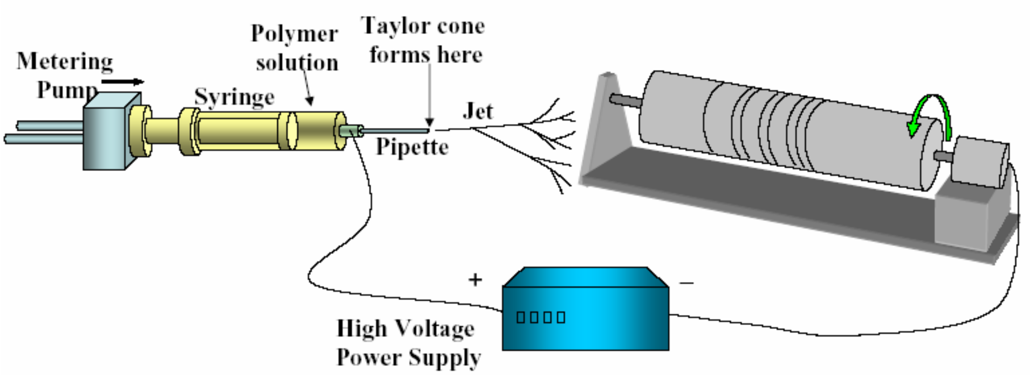

Figure 4.4. Schematic of the electrospinning set-up used for producing aligned nanofibers.

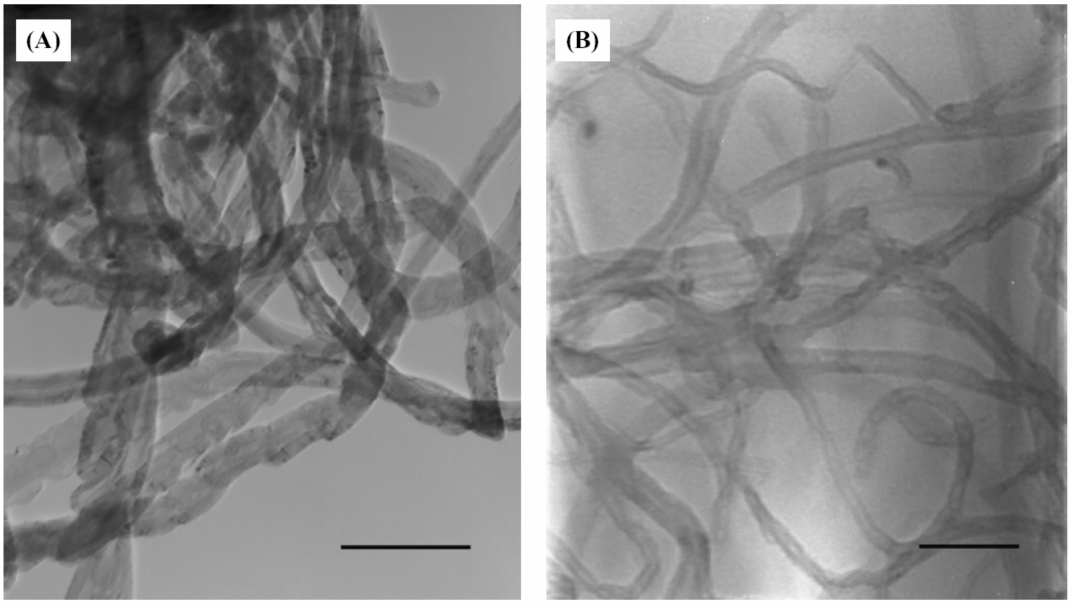

Figure 4.5. TEM images of the MWNTs before **(A)** and after **(B)** purification and functionalization. (Scale bars are 100nm for both images)

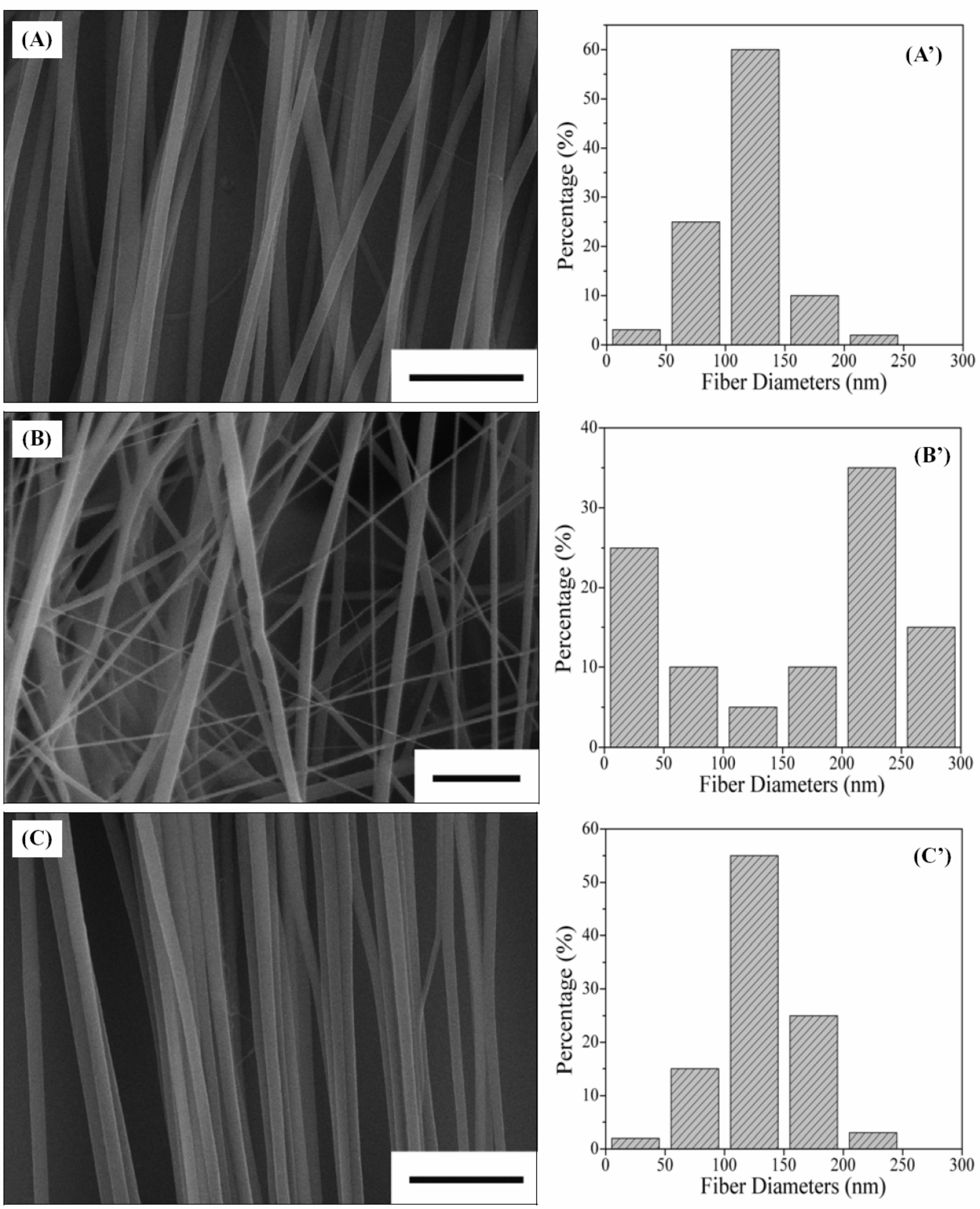

Figure 4.6. SEM pictures of PVAc nanofibers containing **(A)** no carbon nanotubes **(B)** 5wt% u-MWNTs, and **(C)** 5wt% f-MWNTs. Scale bars are 1μm in all three images. **(A')(B')(C')** are corresponding size distributions of the fiber diameters. All samples were collected by a rotating drum with rotation speed of 1000 rpm.

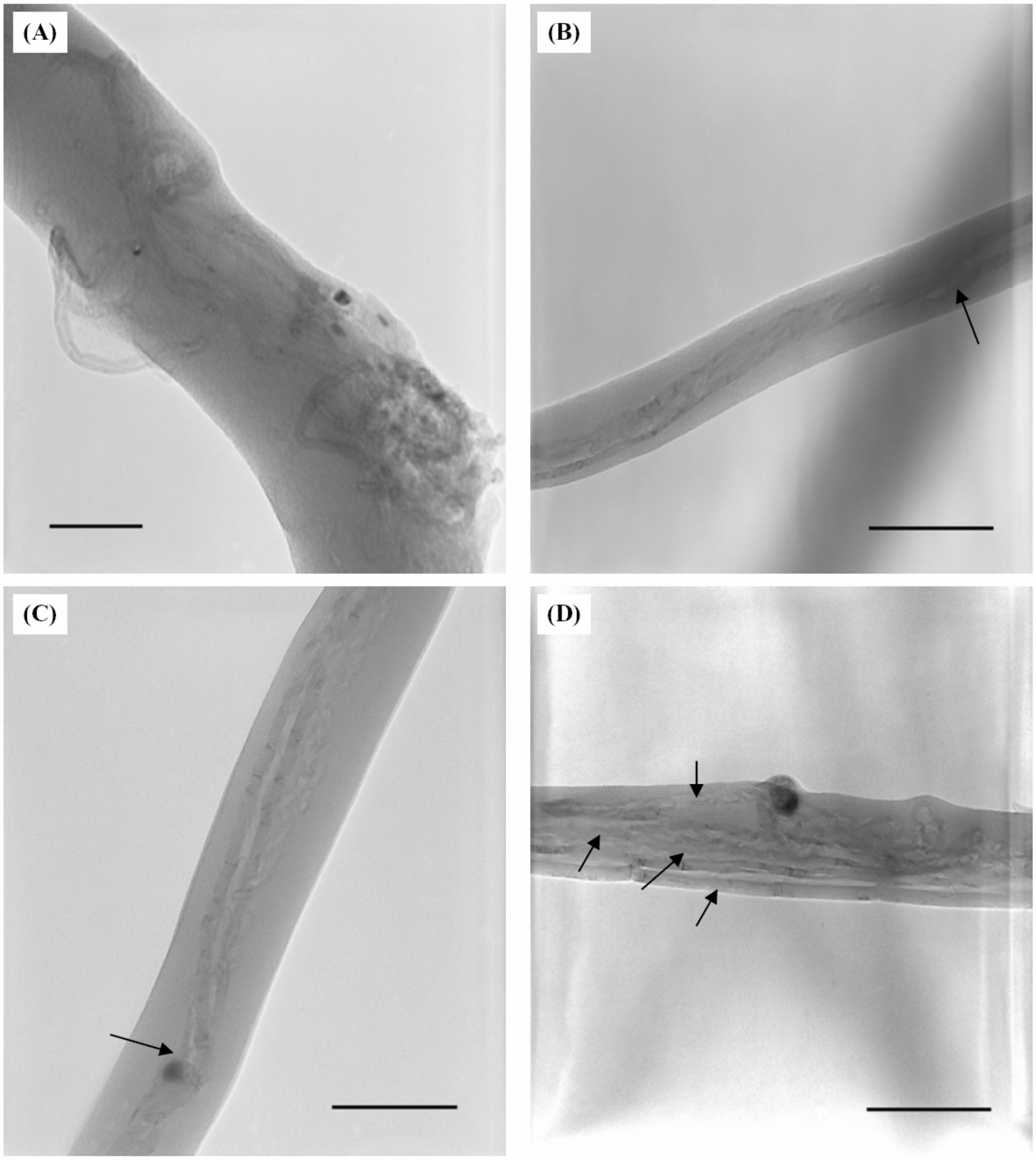

Figure 4.7. TEM images of the MWNT/PVAc nanofibers: **(A)** a thick fiber made from solution with 5wt% u-MWNTs; and nanofibers made from a solution with **(B)**1%, **(C)**3%, **(D)** 5wt% f-MWNTs, showing well-aligned MWNTs along the fiber axis direction. (Scale bars are 100nm in all the images)

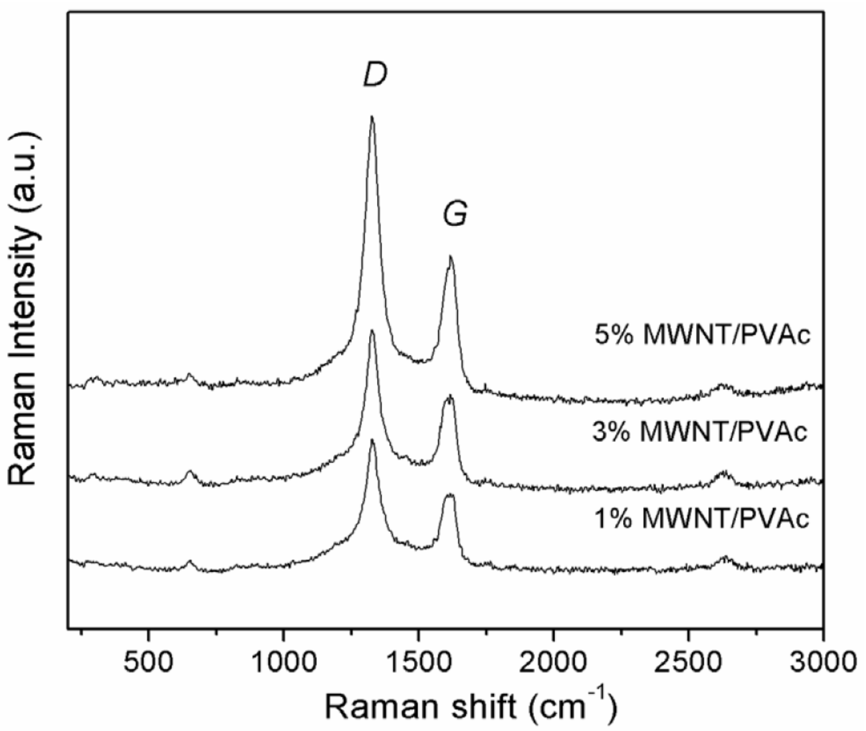

Figure 4.8. Raman spectra of the PVAc nanofibers with different weight percentages of MWNT.

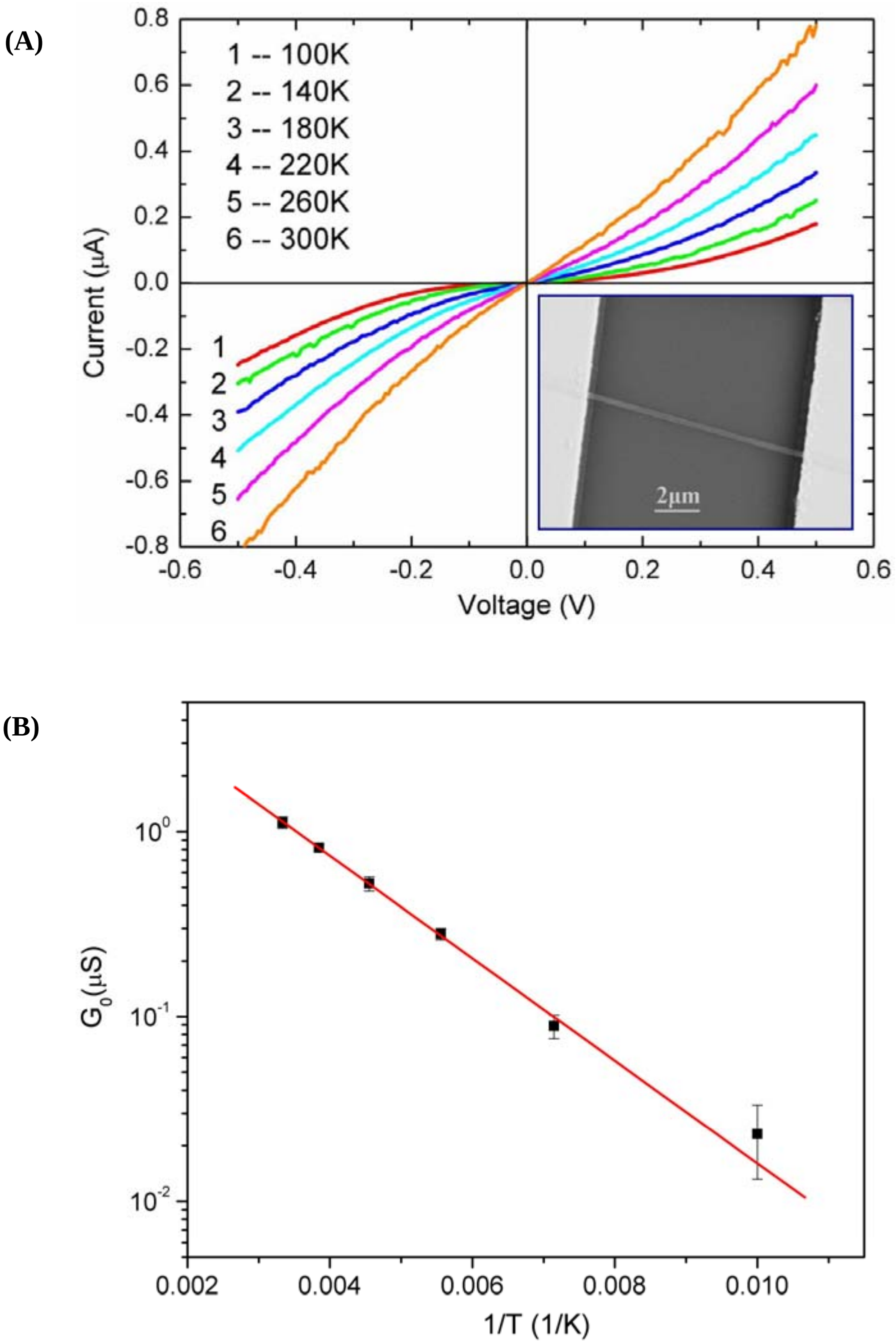

Figure 4.9. (A) I-V characteristics of a single composite fiber, showing non-linear curves from 100K to 300K. The inset is the SEM image of the single fiber measured between two good electrodes; **(B)** Conductance (G_0) dependence on the 1/T of the same composite nanofiber in (A). Red line: fitting of $G_0(T) \sim \exp(-E_a/k_BT)$, resulting an $E_a \sim 55\pm4$ meV.

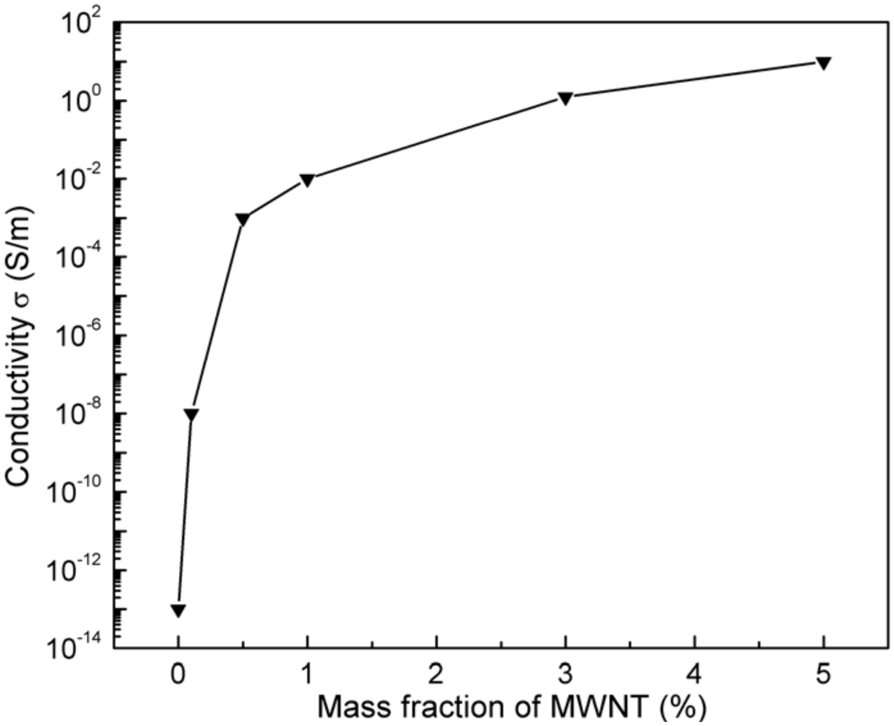

Figure 4.10. Conductivity (σ) dependent on the mass fraction of MWNT (%) for single PVAc/MWNT composite nanofibers.

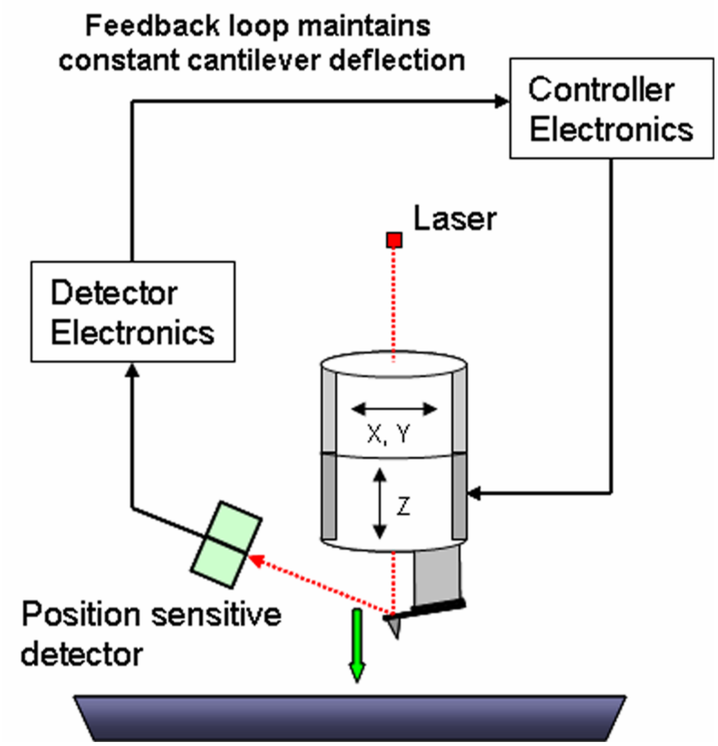

Figure 4.11. Schematic principle of the contact mode AFM.

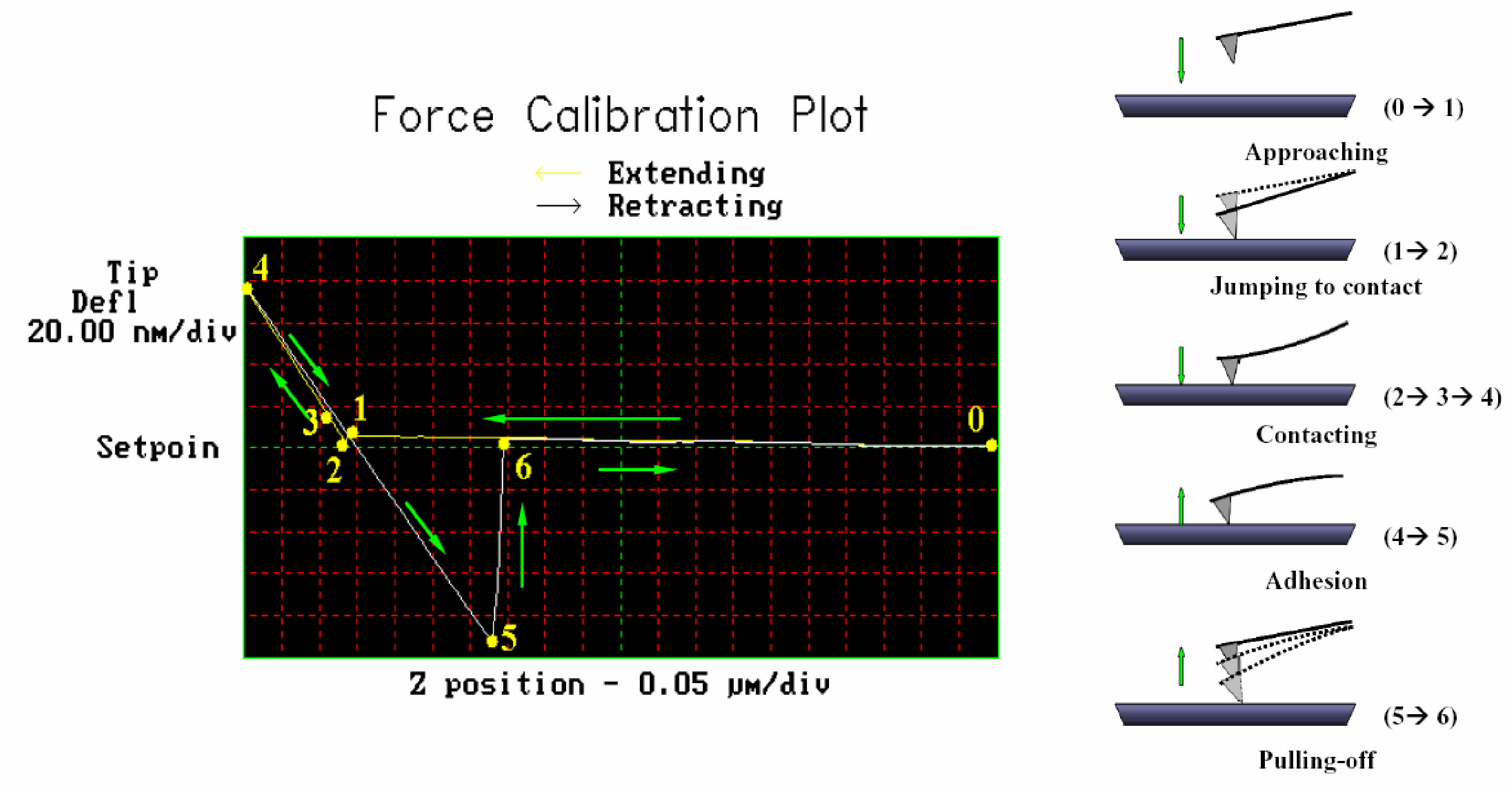

Figure 4.12. An experimental force curve with schematic labeling at corresponding tip-sample interaction points.

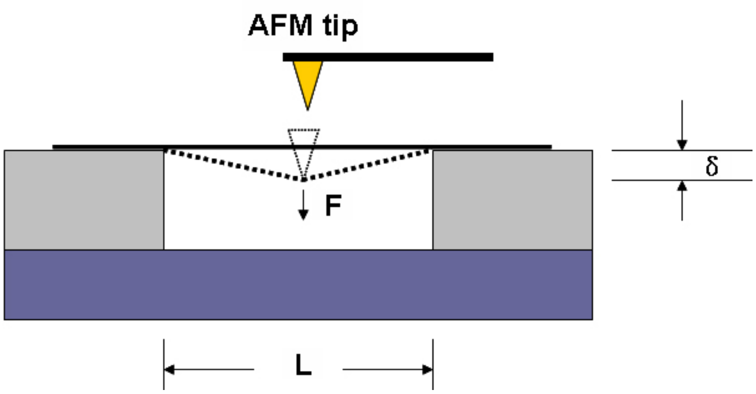

Figure 4.13. Side-view of the three point bending experiment by AFM.

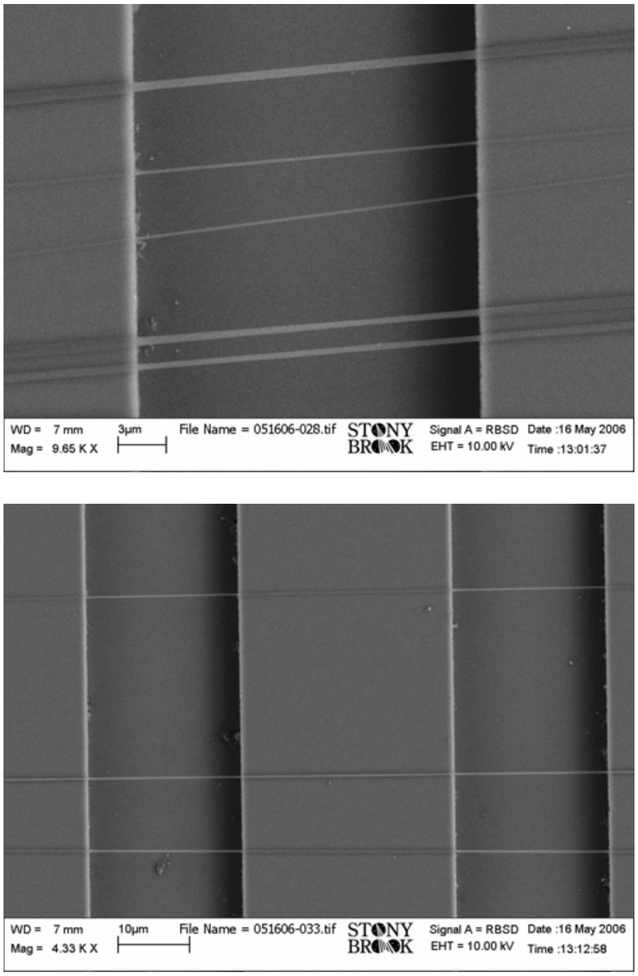

Figure 4.14. SEM images of the suspended PVAc/MWNT composite nanofibers over a 20μm wide trench on the Si chip.

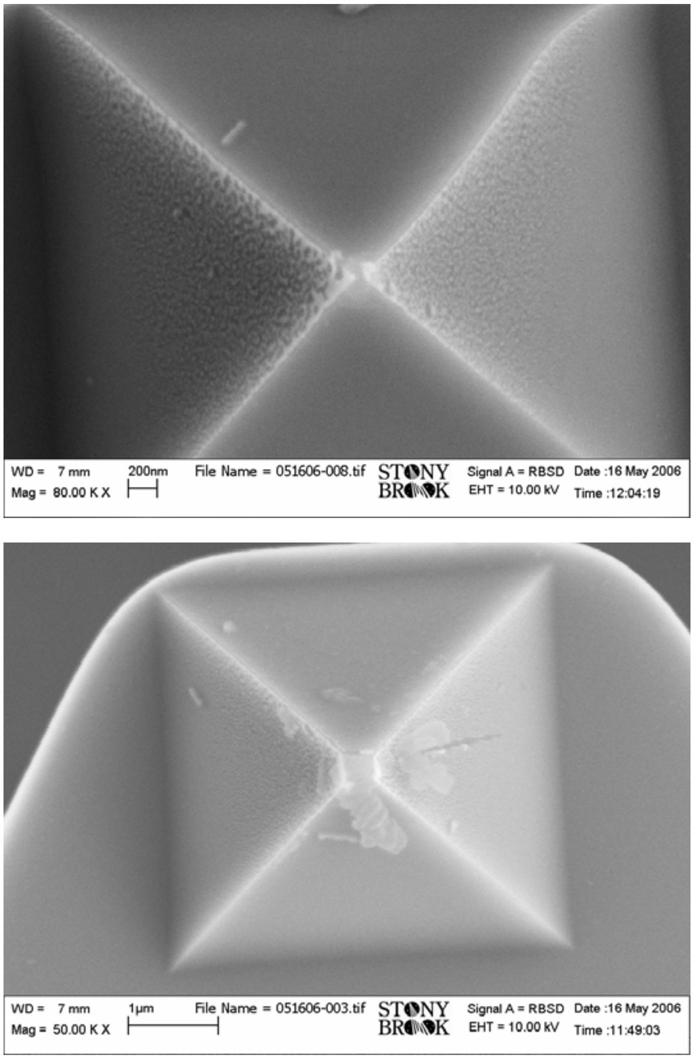

Figure 4.15. SEM images of the AFM probe tip before and after dulling against the Si wafer, showing the curvature radius of the tip was around 200nm, which was impossible to penetrate the fiber.

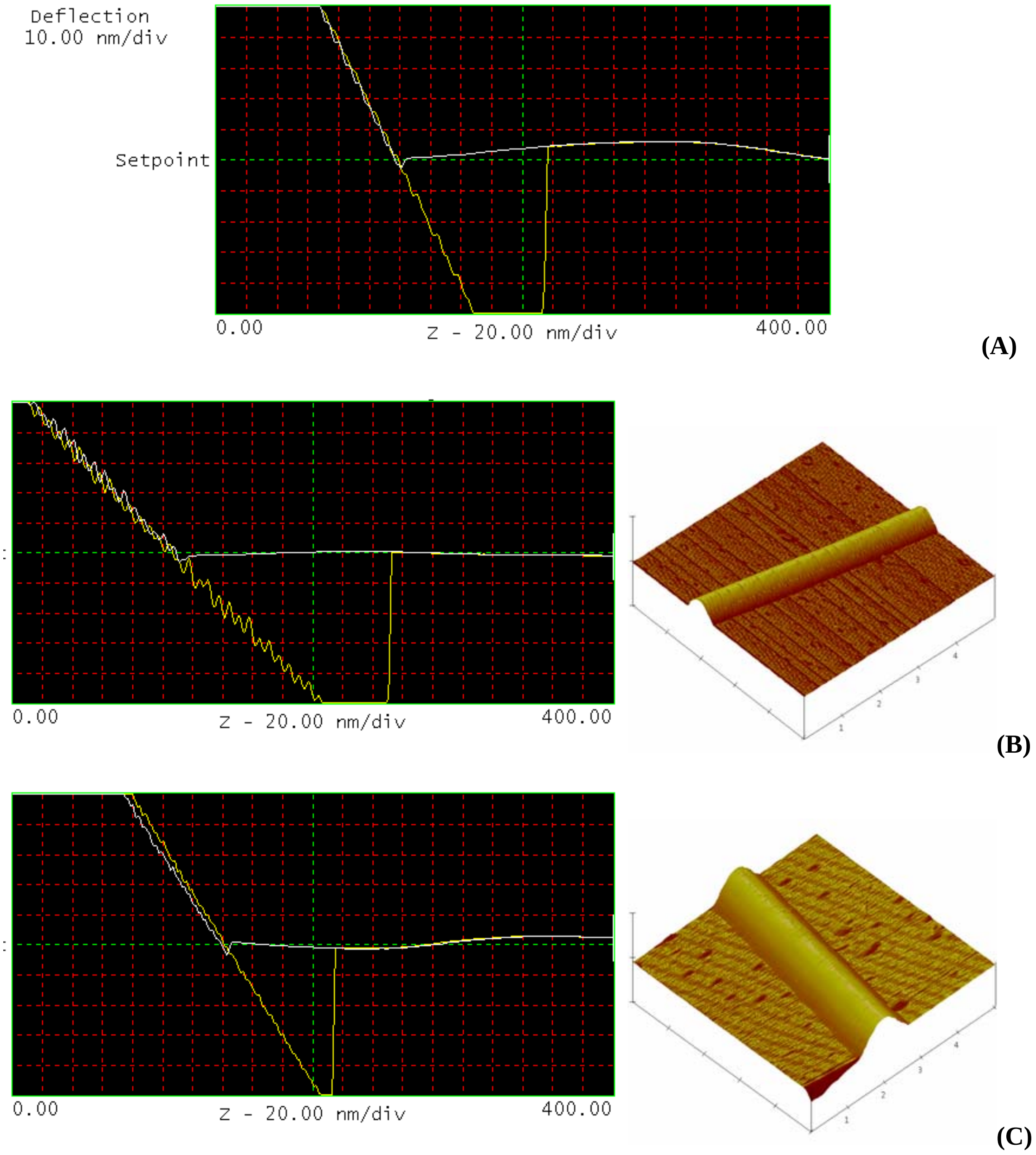

Figure 4.16. Force curves of a piece of clean silicon wafer **(A)**; and MWNT-PVAc composite nanofiber with diameters of 375nm **(B)**; 675nm **(C)**; 290nm **(D)**; 660nm **(E)**. Vertical scales of each graph are all 10nm/div.

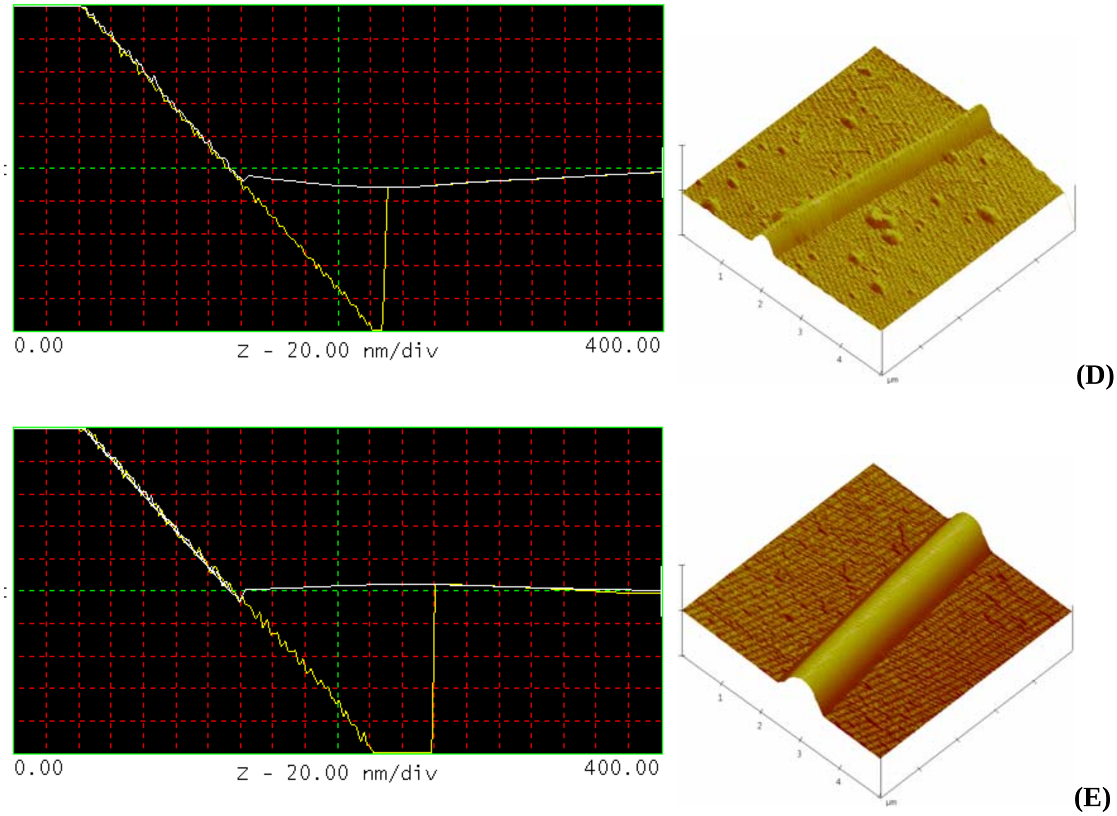

Figure 4.16. (Continued) Force curves of a piece of clean silicon wafer **(A)**; and MWNT-PVAc composite nanofiber with diameters of 375nm **(B)**; 675nm **(C)**; 290nm **(D)**; 660nm **(E)**. Vertical scales of each graph are all 10nm/div.

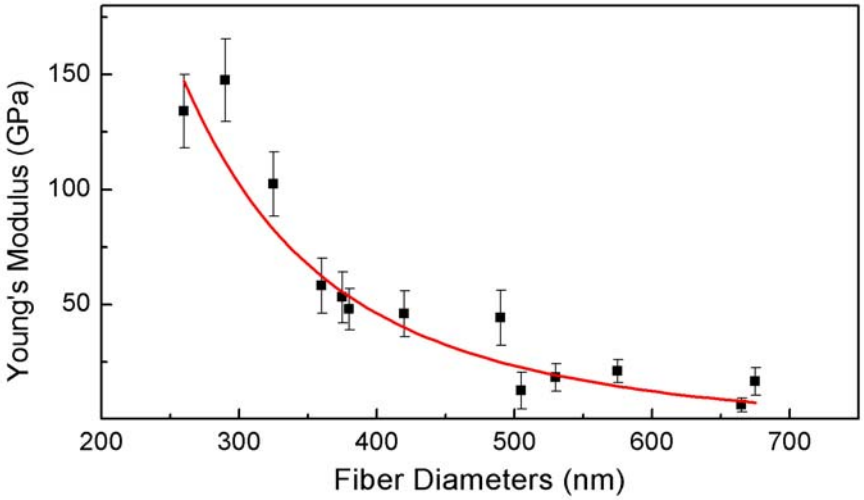

Figure 4.17. The variation of Young' moduli with the diameters of PVAc/MWNT composite nanofibers.

CHAPTER 5

Polymer/MWNT Composite Nanofibers for Gas Sensing Applications

5.1 Introduction

There has been constant endeavor searching for new and better sensing materials in the past due to the importance and wide applications of sensor devices for monitoring living and industrial environments, and for use in chemical, medical, military and homeland security applications [1]. The existing materials, which have found realistic applications for gaseous molecule detection, include semiconducting ceramic metal oxides[1], polymer/carbon black composite layers [2-4], conducting polymers[5] and silicon based transistor devices [6]. In 2001, Kong et al demonstrated, for the first time, the chemical sensors based on individual single-walled carbon nanotubes (SWNTs)[7]. The large surface area provided by the hollow structures and outside walls of nanotubes provides them a very large gas absorptive capacity [8]. In addition, at room temperatures the adsorption of some gas molecules on SWNTs can cause a significant change in electronic and transport properties of the nanotube due to the charge transfer and charge fluctuation [8]. Therefore, the resistance across electrically contacted nanotubes can be modified upon exposure to various gaseous molecules such as NO_2, NH_3, N_2, CO_2, and H_2O. These serve as the basis for carbon nanotube gaseous molecular sensors.

Multiwalled carbon nanotubes (MWNTs) can be considered as a material comprised of concentric “shells” of single walled carbon nanotubes[9]. Although the electronic conduction in MWNTs becomes more complicated due to additional electronic coupling between adjacent shells, the major role is played by the outermost shell, which endows MWNTs similar properties as SWNTs while acting for gaseous molecular detection [10].

Although great progresses have been made in the processing and application of carbon nanotubes, there is still lack of effective means to bridge the gap between the superior properties of carbon nanotubes and meso- and macro-scale structures [11]. The existence of Van der Waals forces between MWNTs makes them intractable to separate and disperse uniformly in the composites, and it is still difficult to obtain long MWNTs in an aligned manner, which limits their applications in device design. The objective of this research is to use a combination of carbon nanotubes and electrospinning processes to produce unique microsized chemical and gaseous sensors. Interdigitated contact structure will be used for the sensing elements. Preliminary measurements of the carbon nanotubes show this nanotube contained film over the sensing elements which had a resistance value of a few hundred ohms at room temperature. This is a more conductive film comparing to metal oxide films, such as SnO_2 or ZnO, that are now widely used in gas sensor research. Devices which use many nanotubes produce lower electrical noise than those with individual tubes. Evaluation of the carbon nanotube film for potential gaseous sensing will be carried out.

5.2 Design of the Chip

As shown in Figure 5.1, the design calls for metal lines 3mm wide with the above design spacing between the lines. The design is a two level mask set

-1st level is for the electrodes (blue).

-2nd level is for the opening of the passivation (green).

Each die was 7x7mm so that the 2x2 array would fit inside the 15mm field size of the GCA AS200 5x Stepper at Cornell Nanoscale Science and Technology Facility (CNF).

5.3 Feasibility Demonstration of the Sensor Based on Polymer/MWNT Composite Nanofibers

5.3.1 Experimental set-up

The feasibility demonstration of the gas sensor was made using set up with the sketch shown on the Figure 5.2. Sensors were placed in a shielding chamber 2 with micro-manipulators, connected to the outer circuit. The actual pictures of the electrical part of the experimental set up and the signal conditioning with A/D converter are shown on the Figures 5.3.

5.3.2 Data acquisition

Composite nanofibers were prepared by electrospinning MWNT/PVAc composite solution with functionalized carbon nanotubes. 5% mass concentrations of MWNTs were used, because that is a sound concentration that can be used to make uniformly distributed MWNTs in the polymer matrix. Specific process for making the composite nanofibers has been described in details in Chapter 4. Herein, the composite nanofibers have been deposited onto the sensor chip (Figure 5.4), which has a series of parallel metal electrodes on the surface of the silicon wafer, prepared by the photolithographic method. Representative SEM and TEM images of the as-deposited composite nanofibers are shown in Figure 5.5 A) and B) respectively. These nanofibers have been testified to be conducting by our previous experiments (see Chapter 4). They worked as the connection between the electrodes, providing the channel for electron transportation, so that a certain resistivity can be measured between the two electrodes.

The sensors were tested by using three different gases: H_2, CO_2 and breath (the most important component, which distinguishes breath from ambient atmosphere is, probably, water vapor). In order to estimate the time constants (adsorption rate) and the regeneration rates, the regimes of testing of the sensor response were chosen as 1) impulse, and 2) steady-state gas exposure. The "impulse" regime was realized with the tube brought on a specific distance (dependently on the distance the amplitude of the signal was changing). The "steady-state" regime was realized by filling the chamber with the gas if interest.

Comparative detection measurements of three different sensors were carried out at room temperature. To establish the influence of the temperature on the response of the sensor, the detection also was carried at the temperature $T{\sim}50^{o}C$, using a "button"- type electric heater. The general view of the sensor's response curves of the signal on the screen of the computer after current-voltage conversion and digitizing is shown on the Figure 5.6.

The typical range of amplitudes of the current change of the sensors in respond to the gases was in the range of 3-25 %. In order to observe the details of the response curves, the signal was amplified. And an input offset was applied to keep the signal within the dynamic range of the analog/digital converter.

5.3.3 Qualitative testing of the sensors

The sensors were preliminary tested for checking their working conditions in regards of the resistance change under the exposure by high, but uncontrolled concentrations of the gases. The output of the sensor on CO_2, breathing and H_2 gas exposure is shown in Figure 5.7 (A) and (B) respectively.

There is a fundamental difference in the response of the sensors to the water vapor (breathing) and adsorption of the gases H_2 and CO_2. The adsorption of the gases H_2 and CO_2 causes the resistance of the sensor decreasing, while H_2O adsorption causes the increasing of the resistance of the sensor. The possible explanation of the opposite sign of the sensor responds to H_2O vs. CO_2 and H_2 could be based on the taking into consideration he polarity of the adsorbed molecules.

Water has two very polar covalent bonds between oxygen and hydrogen. Because water molecule is bent (the oxygen atom is sp^3 hybridized), the two bond dipole moments add up to give water a relatively large molecular dipole moment (Figure 5.8 (A)). This molecular dipole moment creates a Field-effect to a carbon nanotube, while the water molecule is adsorbed. The current through nanotube is reduced then.

Carbon dioxide has two polar covalent C-O bonds. However, the bond dipole moments exactly cancel each other since they are pointing in exactly opposite directions. Thus, CO_2 has no molecular dipole moment. For the molecular model shown on the right (Figure 5.8 (B)), the non-polar carbon dioxide are shown adsorbed on the carbon nanotube surface. CO_2 and H_2 molecules while being adsorbed “repair” the dangling bonds on the surface of the carbon nanotubes, decrease the scattering of the current carriers in the tube and thus increase the current flow.

5.4 Quantitative Measurements of the Polymer/MWNT Sensors

5.4.1 Design of the mass flow control bench

The sketch of the gas flow bench for the precise measurement of the sensitivity, linearity, bias stability, thermal stability, regeneration rate of the gas sensor devices based on the polymer/carbon nanotube nanofibers is shown in Figure 5.9.

The measurement of the sensitivity of the sensors based on the carbon nanotube monolayer are being developed using testing gas flow bench (Figure 5.9). The measurement of the electrical signals is processed using DC technique. The signals will be digitized using standard acquisition boards, and the experimental information will be processed using computers.

Figure 5.10 shows the signal conditioning system based on the SRS current pre-amplifier, Keithley DC voltage source, Keithley multimeter, A/D converter (PCMCIA card NI 4150), and a computer with NI Virtual Bench logger software. Also, there is a controller for programmable flow control valves. Figure 5.10 also shows the gas flow chamber, as a quartz tube with the leads to the gas sensor and the thermocouple for the temperature of the sensor measurements and control using the outer heater; the programmable flow control valves and the gas cylinders with N_2 as gas carrier, H_2 and CO_2 as the gases for testing. The assembled configuration allows controllable flow rate of the testing gases from 1 to 100sccm in the controllable flow rates from 10 to 1000sccm.

5.4.2 Sensitivity, linearity, thermal stability, regeneration rate, bias stability of the gas sensor devices based on the electrospun nanofibers of polymer with MWNTs

Hydrogen has been employed in different fields such as hydrogenation process, petroleum transformation, welding, cryogenic cooling, chemical production of substances, rocket engines, etc. The hydrogen utilization as a clean energy source in fuel cells has been recently researched. Fuel cells are currently used in vehicle and power generators. They are electrochemical devices that can directly convert chemical energy to electrical one, obtaining water as the only waste product. Hydrogen is a colorless and odorless gas, flammable for concentrations higher than 4%. That is why its transport and storage raise many safety questions.

Hydrogen detecting and monitoring sensors are useful for several industries, however inexpensive small and chemically inert sensors have not been developed and commercialized yet. That is why we will concentrate on the quantitative characterization of our sensor devices regarding hydrogen detection.

Sensors were placed in a one-inch diameter quartz tube as a test cell and electrically connected to the outer circuit for their characterization by DC electrical measurements. The carrier gas was ultra-dry grade nitrogen at a constant flow. Detection concentrations of hydrogen were varied from 0.1 to 10 10% (from 1 to 100 sccm in nitrogen flow with the constant rate 1000 sccm). A 1000 sccm nitrogen constant flow was used to achieve a base line. Then the flow controller was used to change the gas flows obtaining the different concentrations. The allowed exposure and recovery times were 5 min duration. The output of the A/D converter proportional to the resistance of the sensor was recorded approximately every 10 ms.

Figure 5.11 shows the response curves for the sensor in real time. The detected output signal variation depends on the detected hydrogen concentration. The desorption processes are relatively slow. Sensor does not reach saturation during the exposure times (5min) but it has fast response time.

The Figure 5.12 was used for the estimation of the sensitivity limit of the sensor. The extrapolation of the linear dependence down to the “0”-output signal (more precisely to the nose level) gives us a chance to determine a minimum detection level of hydrogen flow in N_2 as 0.1 sccm of H_2 in 1000 of N_2, which is a few ppm.

The response time is defined as the time to achieve a steady response state after switching gas concentrations. Figure 5.13(A) shows a complete sensor response to hydrogen. The response time is of the order of a few seconds and is limited by the geometry and internal volumes of the flow bench. Note that the response time of the sensor to the hydrogen was determined as less than 80 ms under the conditions of fast gas delivery to the sensor.

The bias stability of the gas sensor was defined as the stability of the sensor output over a long period of time. We can see the stability and reproducibility of the sensor from the measurement of this parameter. Figure 5.13(B) is the sensor bias stability of the polymer/MWNT composite sensor. The output signals measured only showed a slight and gradual decrease over 30 min, indicating a relatively good stability of the sensor if it works under the hydrogen atmosphere continuously. The bias stability curve also explained the shifting-down of the sensor base-line during the measurement in Figure 5.11.

5.4.3 Sensitivity of the gas sensor devices based on the MWNTs

In order to compare the sensing properties of Polymer/MWNTs composite nanofibers with that of the pure MWNT layers, experiments have been carried out to measure the sensing properties of the sensor with pure MWNTs as the sensing elements. 0.024g functionalized MWNTs were dispersed in 4ml DMF to form a uniform suspension. The solution was drop-deposited onto the same sensor chips with parallel metal electrodes. After the DMF evaporated, a network of nanotubes lay on the electrodes to bridge the electrodes (see Figure 5.14). The DMF was chosen because the amide group can easily attach to the surface of the functionalized carbon nanotubes. This ensures good-quality MWNT deposition on top of the electrodes area. The samples were then dried in air to get rid of the DMF residue. The density of the MWNTs across the electrodes can be adjusted by varying the concentration of the MWNT-DMF solution.

Figure 5.16(A) shows non-linear dependence of the sensor response in linear scale. But the response of the sensor in semi-log scale is linear (Figure 5.16(B)). Figure 5.16(B) was also used for the estimation of the sensitivity limit of the sensor. The extrapolation of the linear dependence down to the “0”-output signal (more precisely to the noise level) gives us a chance to determine a minimum detection level of hydrogen flow in N_2 as 0.1sccm of H_2 in 1000 of N_2, which is a few ppm. The MWNT sensor showed very similar response behavior as the polymer/MWNT nanocomposite sensors, implying that the real sensing element in the composite sensor is the MWNT.

To establish the influence of the temperature on the response of the sensor, the detection was carried out in the temperature range from 25 to 50^{o}C. Figure 5.17 and 5.18 show the drift on the sensor response dependently upon the temperature. Figure 5.19 is the bias stability of the MWNT sensor. The output signals showed a gradual decrease over 30 min, which is greater than the response of the nanocomposite sensors, indicating the disadvantage of using the pure MWNT layer as sensing element. The electrospun polymer matrix scaffold provides a more stably assembled MWNTs for the gaseous sensing applications.

5.5 Conclusions

The sensor devices, based on the electrospun polymer nanofibers with multiwalled carbon nanotubes have shown feasible gas sensing properties. There is a fundamental difference in the response of the sensor to the water vapor (breathing) and adsorption of the gases H_2 and CO_2. The adsorption of the gases H_2 and CO_2 causes the resistance of the sensor to decrease, while H_2O adsorption causes the increase of the resistance of the sensor. The difference in the sensor responses is due to the modification of the electron state of the carbon nanotube surfaces while it interacts with various gas molecules.

Quantitative experiments with precise gas flow control, temperature variation and its influence on the adsorption rate of the gases have been carried out on the composite nanofibers. The sample showed measurable response to ppm-scale H_2 at room temperature, indicating an energy effective hydrogen sensor could be realized by using these composite nanofibers as sensing elements. The estimated minimum detection level of hydrogen flow in N_2 is 0.1sccm of H_2 in 1000sccm of N_2, which is a few ppm of concentration. The response times are of the order of a few seconds and are limited by the geometry and internal volumes of the flow bench.

The sensor devices show significant temperature and bias stability. The self-assembled arrays of MWNTs have also shown feasible hydrogen detection properties, which is very similar to the response signals from the above composite nanofibers. The similarity between the sensing behavior of the composite nanofibers and pure MWNT layers implies that the real sensing elements is the MWNTs, while the electrospun polymer matrix works as a scaffold for easily assembling the carbon nanotubes and providing effective nanoporous channels for the interaction between the sensing elements and the gas molecules.

References

1. *Special issue on gas sensing materials*. Materials Research Society: 1999; Vol. 24.

2. Lonergan, M. C.; Severin, E. J.; Doleman, B. J.; Beaber, S. A.; Grubb, R. H.; Lewis, N. S., Array-based vapor sensing using chemically sensitive, carbon black-polymer resistors. *Chemistry of Materials* **1996,** 8, (9), 2298-2312.

3. Safadi, B.; Andrews, R.; Grulke, E. A., Multiwalled carbon nanotube polymer composites: Synthesis and characterization of thin films. *Journal of Applied Polymer Science* **2002,** 84, (14), 2660-2669.

4. Goh, H. W.; Goh, S. H.; Xu, G. Q.; Pramoda, K. P.; Zhang, W. D., Dynamic mechanical behavior of in situ functionalized multi-walled carbon nano tube/phenoxy resin composite. *Chemical Physics Letters* **2003,** 373, (3-4), 277-283.

5. Miasik, J. J.; Hooper, A.; Tofield, B. C., Conducting Polymer Gas Sensors. *Journal of the Chemical Society-Faraday Transactions I* **1986,** 82, 1117-&.

6. McConnell, H. M.; Owicki, J. C.; Parce, J. W.; Miller, D. L.; Baxter, G. T.; Wada, H. G.; Pitchford, S., The Cytosensor Microphysiometer - Biological Applications of Silicon Technology. *Science* **1992,** 257, (5078), 1906-1912.

7. Kong, J.; Franklin, N. R.; Zhou, C. W.; Chapline, M. G.; Peng, S.; Cho, K. J.; Dai, H. J., Nanotube molecular wires as chemical sensors. *Science* **2000,** 287, (5453), 622-625.

8. Zhao, J. J.; Buldum, A.; Han, J.; Lu, J. P., Gas molecule adsorption in carbon nanotubes and nanotube bundles. *Nanotechnology* **2002,** 13, (2), 195-200.

9. de Pablo, P. J.; Graugnard, E.; Walsh, B.; Andres, R. P.; Datta, S.; Reifenberger, R., A simple, reliable technique for making electrical contact to multiwalled carbon nanotubes. *Applied Physics Letters* **1999,** 74, (2), 323-325.

10. Salvetat, J. P.; Briggs, G. A. D.; Bonard, J. M.; Bacsa, R. R.; Kulik, A. J.; Stockli, T.; Burnham, N. A.; Forro, L., Elastic and shear moduli of single-walled carbon nanotube ropes. *Physical Review Letters* **1999,** 82, (5), 944-947.

11. Calvert, P., Nanotube composites - A recipe for strength. *Nature* **1999,** 399, (6733), 210-211.

FIGURES:

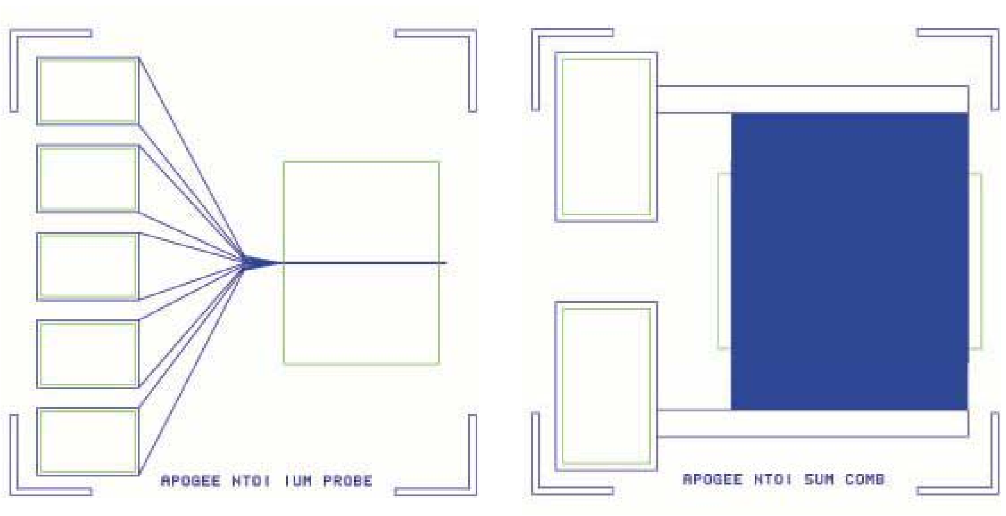

(A) **(B)**

Figure 5.1. Images of the design for electrode chip with the following configurations: 1 mm probe electrode (A); and 1 mm interdigitated comb electrode (B).

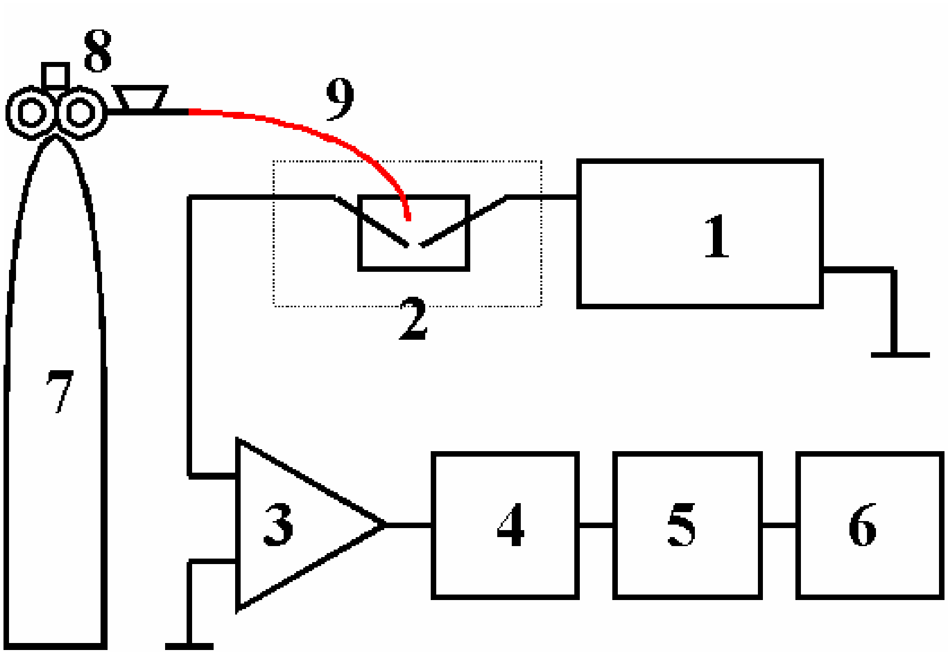

Figure 5.2. The sketch of the set up used for the feasibility demonstration:
1 - DC power supply Keithley 2400;
2 - Chamber with the sensor and micro-manipulators;
3 - Current amplifier;
4 - Signal conditioning board CB-27T (National Instruments);
5 - Analog/Digital converter – PCMCIA card NI-4350;
6 - Computer with NI data lodging software;
7 - Gas tank (H_2 and CO_2);
8 - Pressure regulator;
9 – Tube for gas flow.

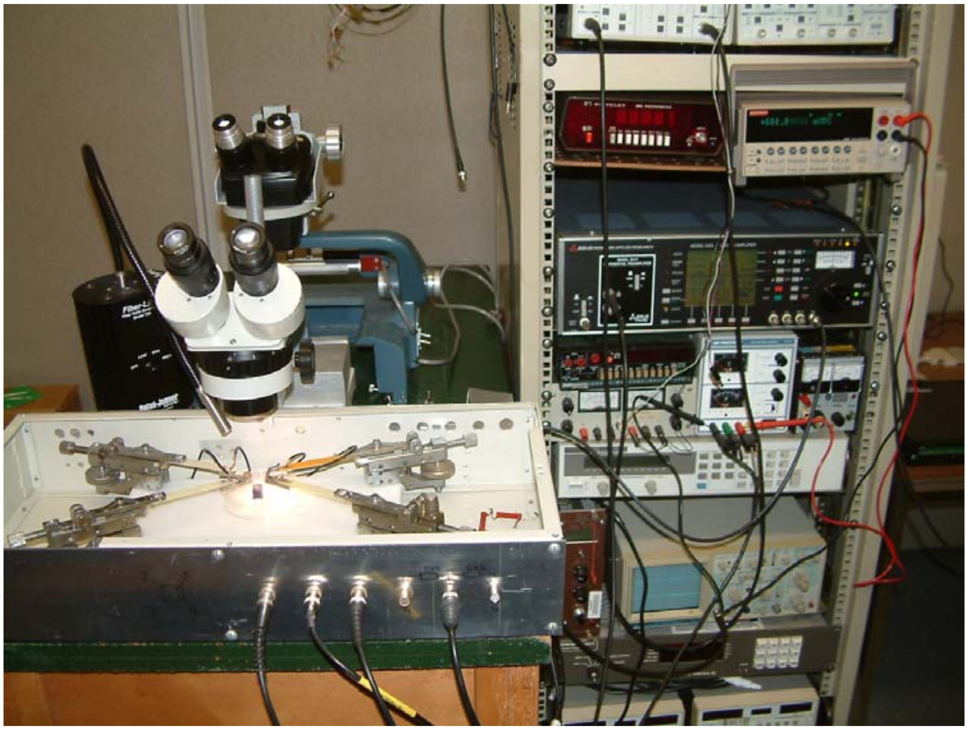

Figure 5.3. Electrical signal acquisition cell with micro-manipulators, signal conditioning equipment (lock-in amplifier, current and voltage Stanford Research pre-amplifiers, power supplies).

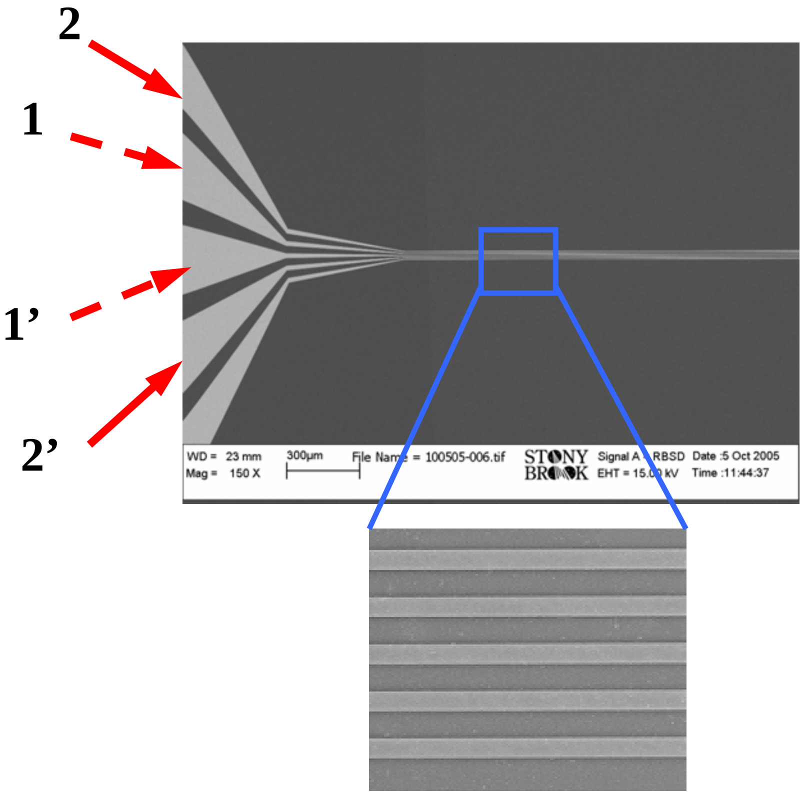

Figure 5.4. Metal electrodes with 0.5μm separation at different magnification. The signal can be detected from 1-1’ (low surface area) or 2-2’ (high surface area) pairs of the electrodes.

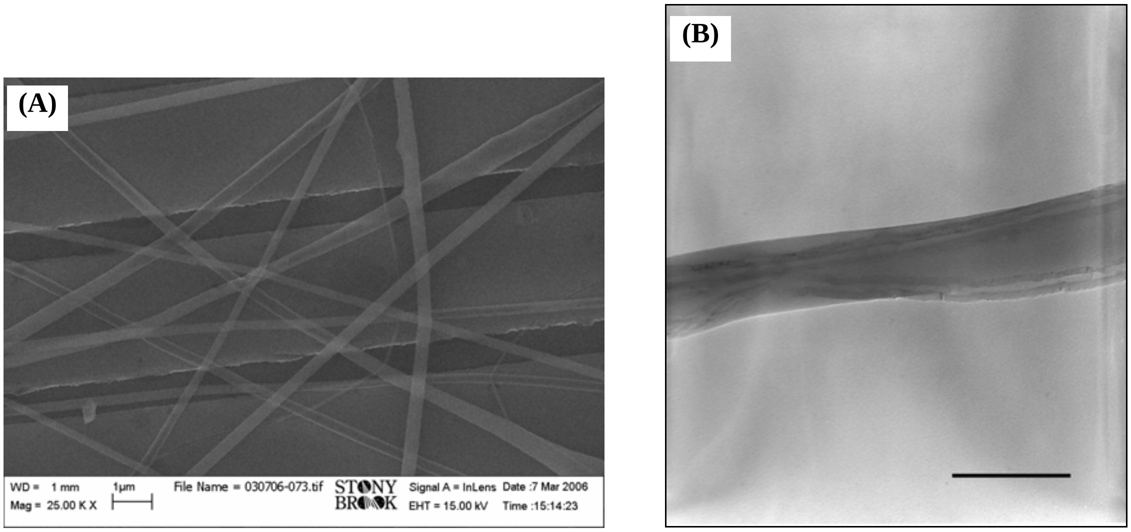

Figure 5.5. (A) SEM image of the array of polymer/MWNT nanofibers; (B) TEM image of the polymer nanofiber with aligned carbon nanotube (Scale bar is 100 nm).

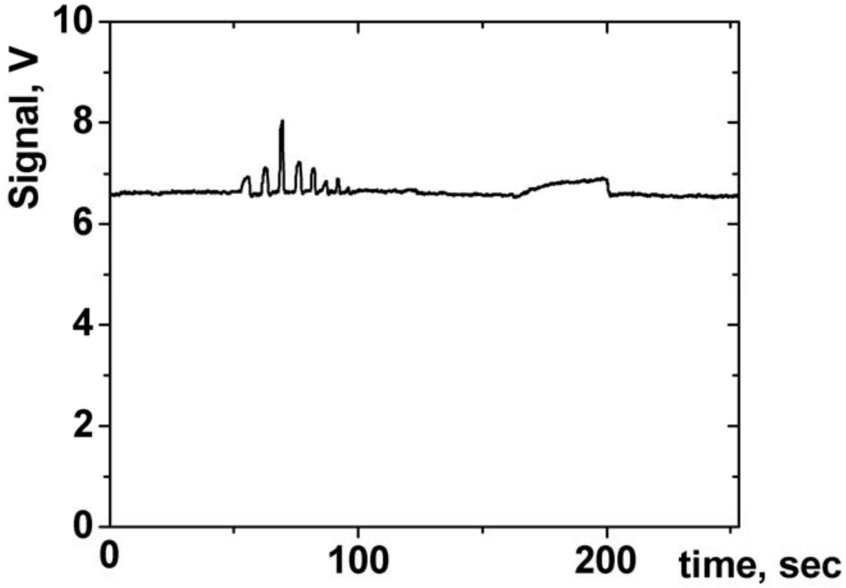

Figure 5.6. General view of the signal on the screen of the computer after current-voltage conversion and digitizing.

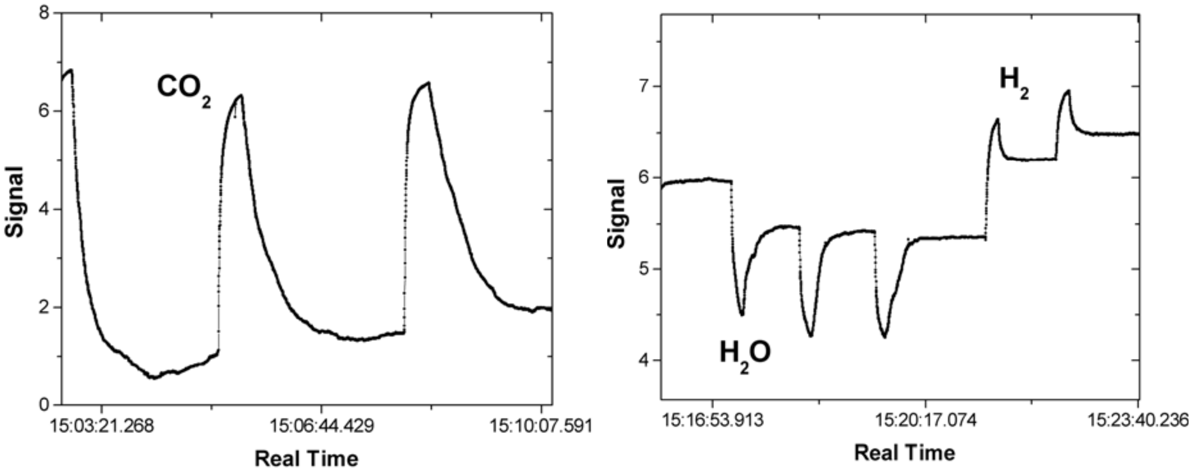

(A)

(B)

Figure 5.7. The output of the sensor with 5µm probe electrode: (A) CO_2, (B) H_2O and H_2

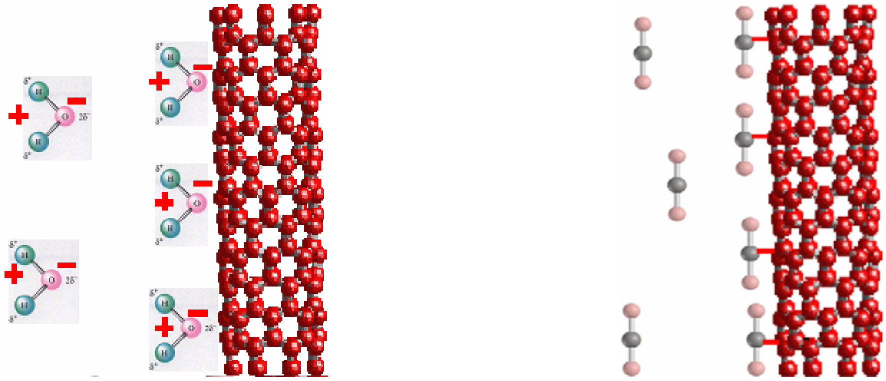

(A)

(B)

Figure 5.8. The model of (A) water molecules and (B) carbon dioxide molecules adsorption on the surface of carbon nanotubes.

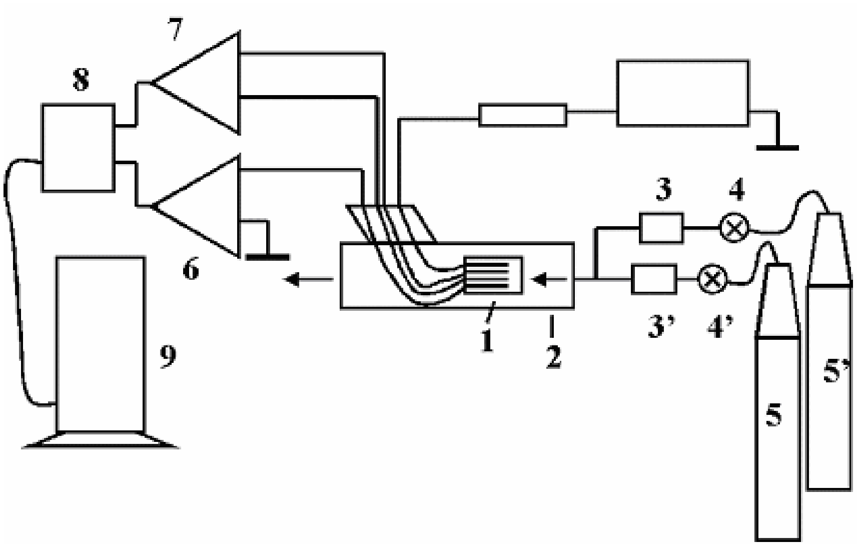

Figure 5.9. The experimental set up for the quantitative measurements of the gas sensors : 1- sensor; 2 - testing gas flow bench; 3, 3'- digital flow controllers; 4,4'- valves and pressure regulators; 5, 5'-gas tanks; 6-current pre-amplifier; 7- voltage preamplifier; 8-A/D converter; 9-computer.

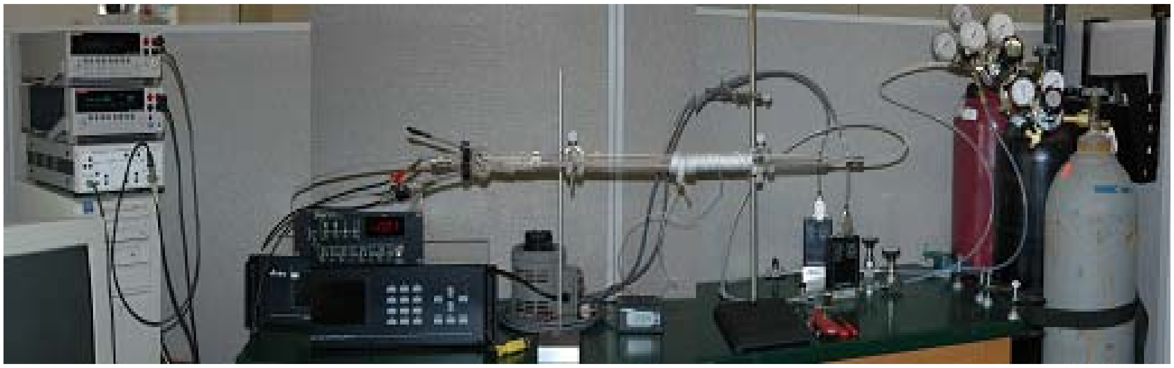

Figure 5.10. Picture of the real mass-flow control bench for quantitative test of the gas sensors.

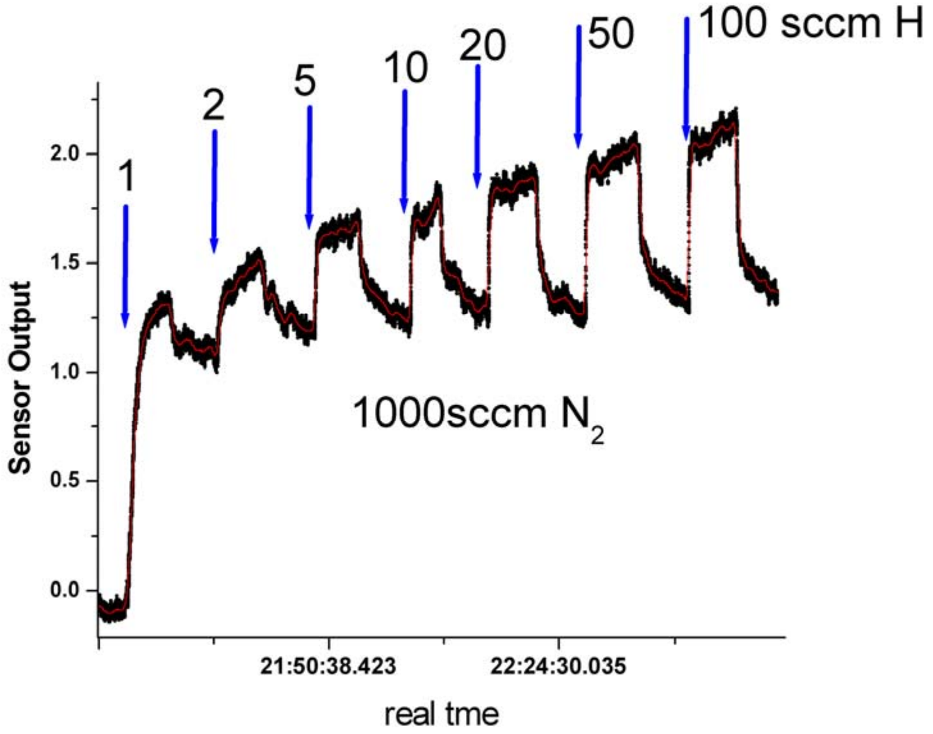

Figure 5.11. The response curves for the sensor made from polymer/MWNT in real time.

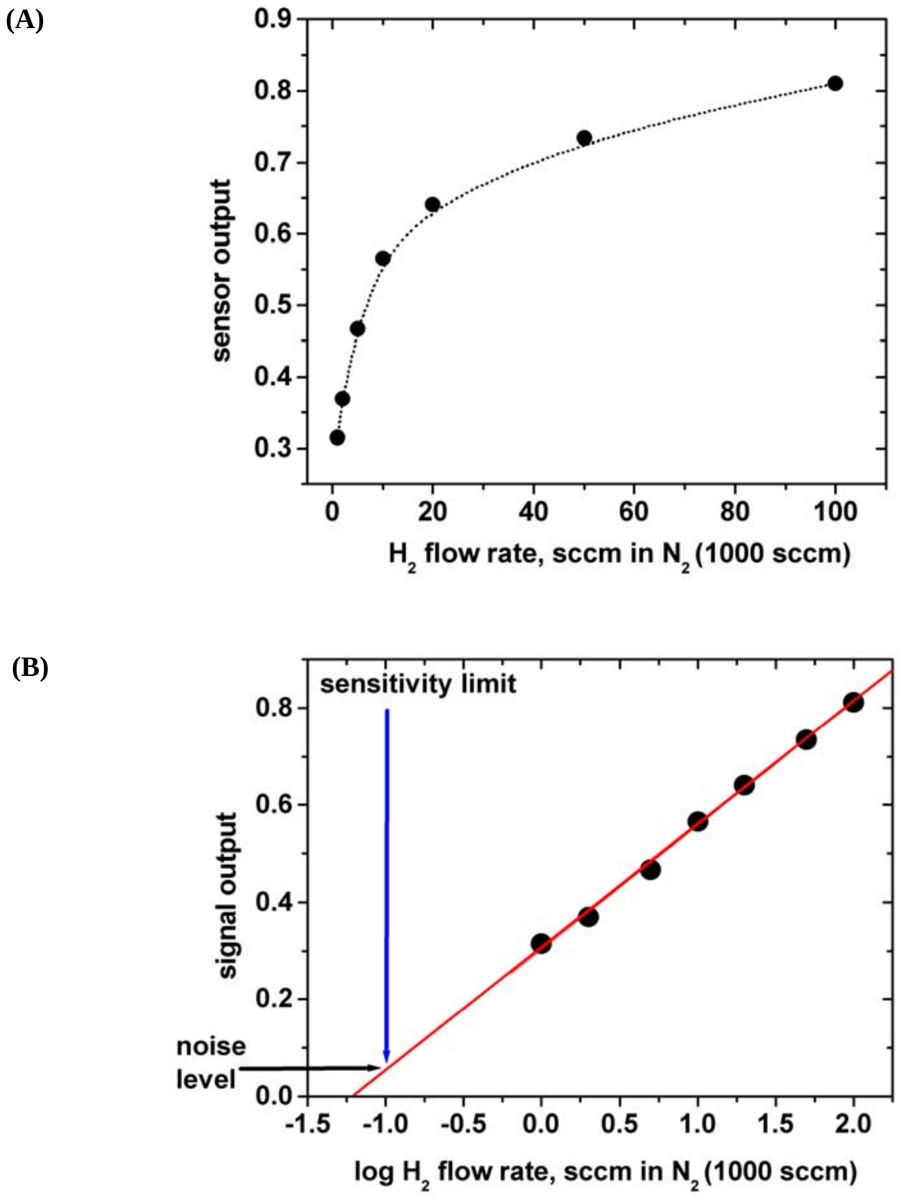

Figure 5.12. The dependence of the response of the nanocomposite sensor on H_2 flow rate in linear (A) and semi-log scale (B).

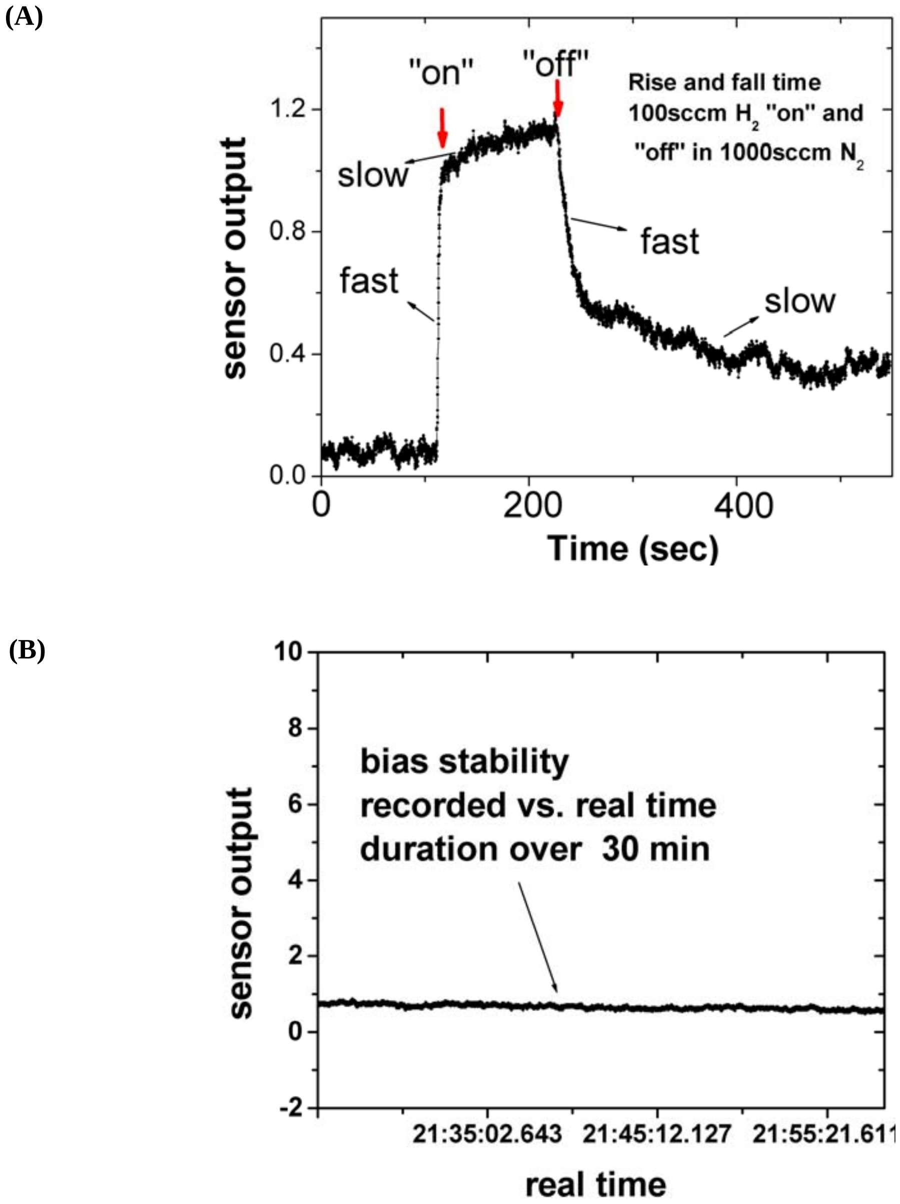

Figure 5.13. (A) The response curve for the polymer/MWNT sensor; (B) bias stability of the sensor.

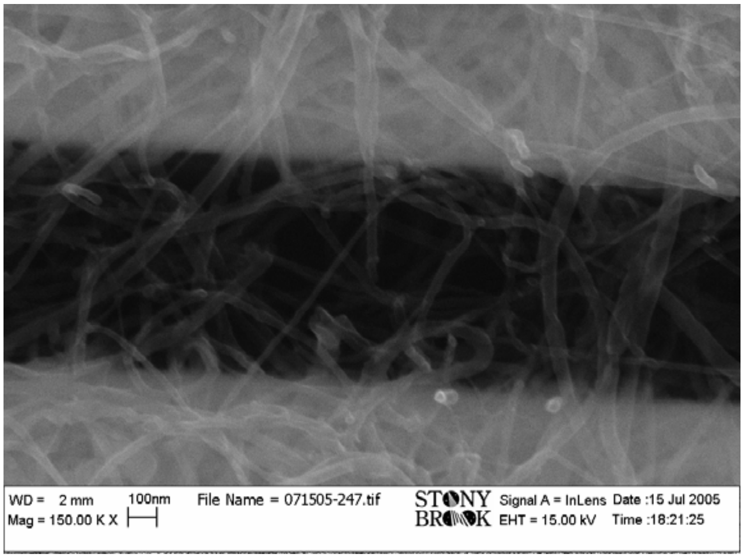

Figure 5.14. Functionalized MWNT carbon nanotube arrays (layers) between the metal electrodes with 0.5μm separation.

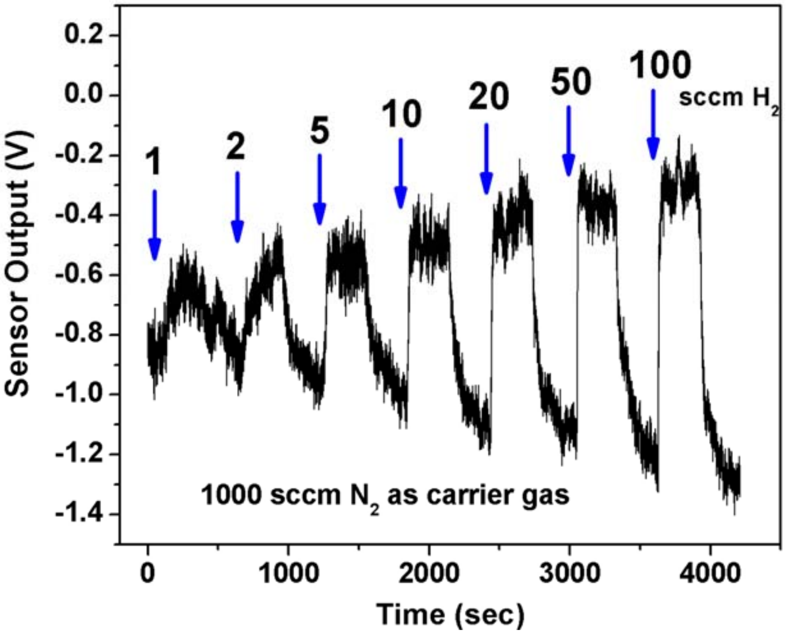

Figure 5.15. The response curves for the MWNT sensor in real time.

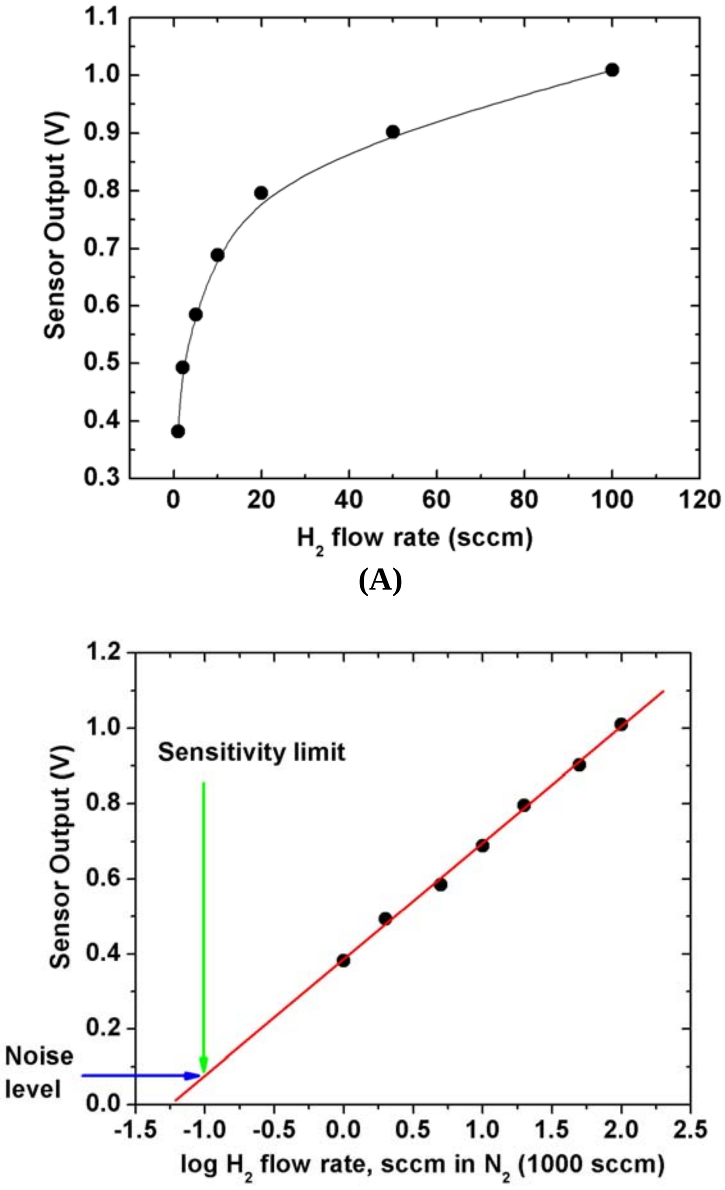

(A)

(B)

Figure 5.16. (A) Non-linear dependence of the MWNT sensor response on the hydrogen concentration in linear scale; (B) Linear dependence of the sensor response on the hydrogen concentration in semi-log scale.

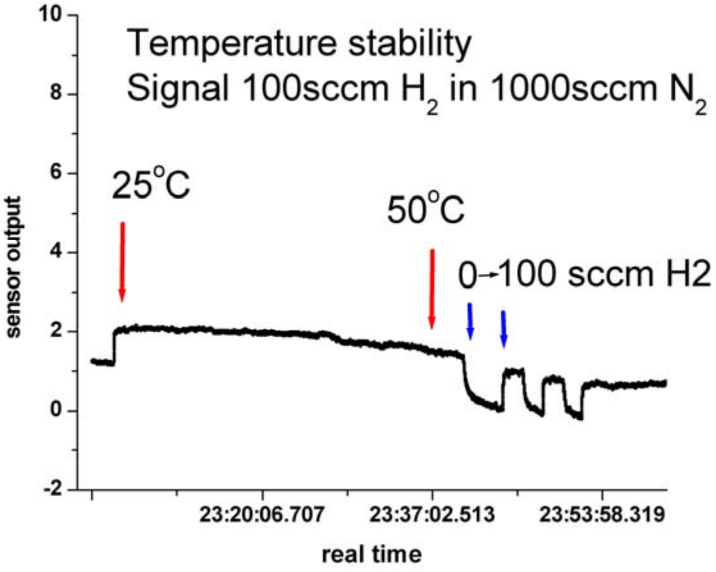

Figure 5.17. The continuous drift on the sensor response with changing temperatures.

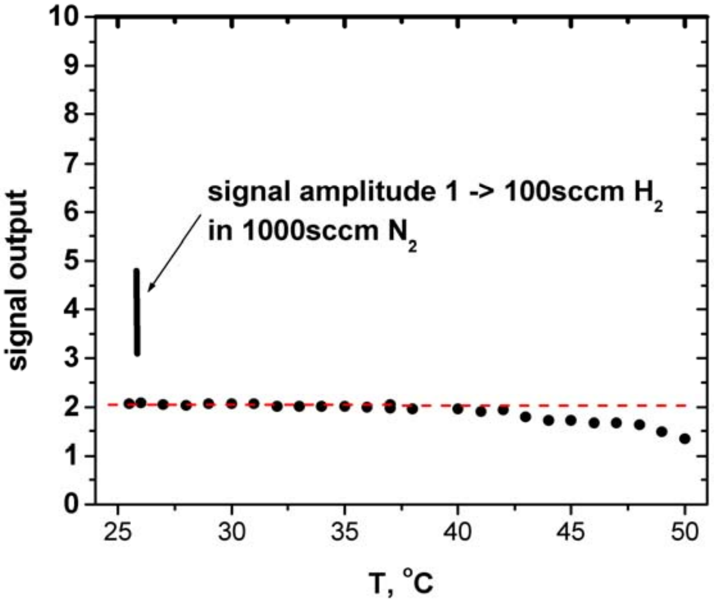

Figure 5.18. The drift of the signal output dependent on the temperature.

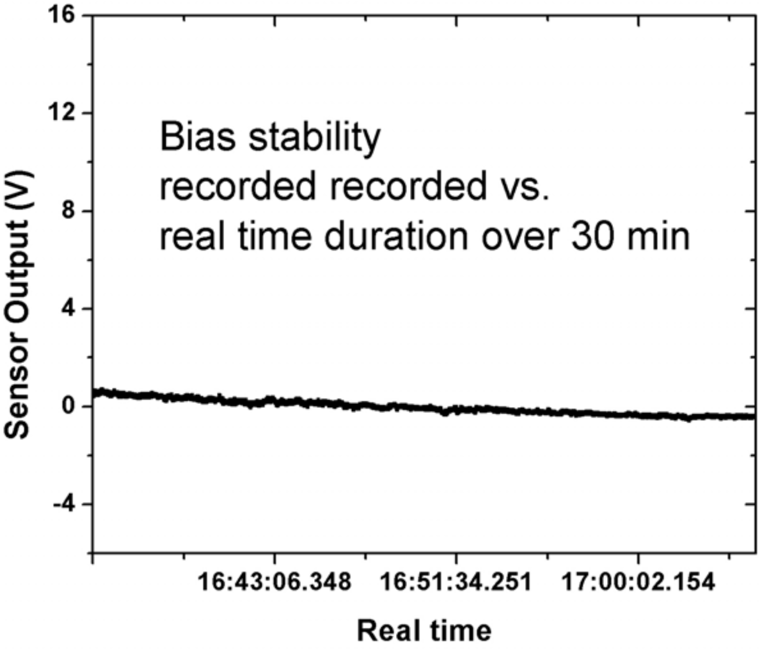

Figure 5.19. Bias stability of the MWNT sensor.

CHAPTER 6

Highlights of This Research and Future Work

6.1 Highlights of This Research

This work is a tentative study on the processing and properties of 1D nanostructures fabricated by electrospinning technique. A series of 1D nanocomposite materials with peculiar morphologies and properties have been prepared successfully by this method, including both polymer/metal oxide nanowires, nanobelts, nanoplatelets and MWNT reinforced composite nanofibers.

Although electrospinning technique has been introduced for producing 1D nanofibers for tens of years, we have greatly extended the capability of this technique in the processing of some novel nanostructures with improved properties compared with their bulk counterparts. At the same time, some advanced characterization methods have been designed and developed to investigate these nanostructures from a basic science view point of their formation mechanism as to their specific properties. Highlights in this research are listed below:

1. For the first time, tungsten oxide polycrystalline nanofibers have been successfully prepared by combining electrospinning method with sol-gel processing. Systematic studies have been carried out to determine the detailed processing parameters for the morphology control of the ceramic nanofibers after post-calcination process.

2. A synchrotron-based *in situ* x-ray diffraction cell has been designed and applied to monitor the phases formed *in situ* at high temperatures. This has provided a better picture of exact phase transformation regions when XRD spectrum is taken *in situ* at smaller

temperature intervals.

3. The as-prepared tungsten oxide ceramic nanofibers have been successfully applied for gas sensor devices. Sensitivity of these polycrystalline nanofibers toward ammonia has shown significant improvement compared with the reported results for the WO_3 bulk materials or thin films. This is attributed to the high porosities and nanoscaled crystallites provided by the unique morphology composed of multilayer of WO_3 nanofibers.

4. An intercalated growth mechanism has been proposed to explain the formation of molybdenum oxide nanoplatelets and nanobelts from the hybrid nanocomposites. This mechanism provided valuable insights into the function of electrospun nanofibers as a disposable template for the morphology control of materials with layered structures.

5. CNTs functionalized by an oxidation method have been introduced in this work to achieve a uniform composite dispersion in the polymer solution with high percentages of CNTs. Ordered 1D nanocomposite fibers with uniform diameters were obtained by electrospinning technique with aligned MWNTs as the nanofiller. Unique combination of the properties of CNTs has been retained by the composite nanofibers, which provide an effective bridge to translate the superior properties of CNTs into meso- and macro-scale structures.

6. Atomic Force Microscope (AFM) have been applied to study nano-mechanical properties of the individual nanofibers based on the classic beam bending mechanics. Significantly increased Young's moduli have been observed for the composite nanofibers with high CNT concentrations and lowered diameters.

7. With the incorporation of a certain concentration of CNTs, conducting composite nanofibers can be achieved. Temperature dependent electrical property study of the

composite nanofibers testified the semiconducting property of these nanofibers with low activation energy. By detecting the resistivity change of these conducting nanofibers, room temperature sensor devices have been developed. Sensor devices made from the polymer/MWNT composite nanofibers are much more energy effective compared with the regular metal oxide-based sensors, which requires elevated temperatures in order to be conducting. And they also provide an improved signal-to-noise ratio and a more stable performance compared with sensor devices made from pure MWNTs monolayer.

6.2 Suggestions for Future Work

Electrospinning technique has proved to be a versatile and cost effective method for producing 1D nanofibers, nanoporous mats as well as ordered polymer fiber patterns. These polymer-based architectures may find even wider applications beyond the examples elaborated in this dissertation. Promising applications of the nanoscale fibers include: tissue engineering, drug delivery, wound dressing and filtration industry.

From the view point of basic scientific researches on the synthesis of nanostructures, electrospinning technique can be combined with other synthesis method, such as sol-gel chemistry, to produce more metal oxide nanofibers or even compound ceramic nanofibers for various applications. This idea can be very important for the gas sensing applications, because of the high porosity and nano-crystallites provided by this synthesis method. By controlling the mole ratio of the sol-gel solution of different ceramic precursors, precise tailoring of the stoichiometry of the compound ceramics can be realized. Detailed investigations on the sensitivity, selectivity, stability and recovery time of the compound ceramic sensors are highly recommended.

On the other hand, the capability of electrospinning technique in assembling nanofillers can still be extended. Direct encapsulation of CNTs has been realized by a successful preparation of the composite dispersions in this work. Therefore, a uniform solution or dispersion system is necessary for achieving a thorough incorporation of the nanofillers. Functionalization through all kinds of chemical or physical methods may be necessary and effective for the dispersion system preparation. By encapsulating different nano-particles, nanotubes, nanorods or even nano-medicine, unique mechanical, electrical and medical properties can be achieved within the matrix of 1D polymer nanofibers. Meanwhile, modified electrospinning set-up can be designed to customize nanofiber assemblies for specific purposes.

Another important application of the nanofibrous scaffold is in biomedical materials and tissue engineering. Successful cell proliferation and morphology control inside a bio-compatible scaffold may realize the dermal reconstitution in a very effective manner.